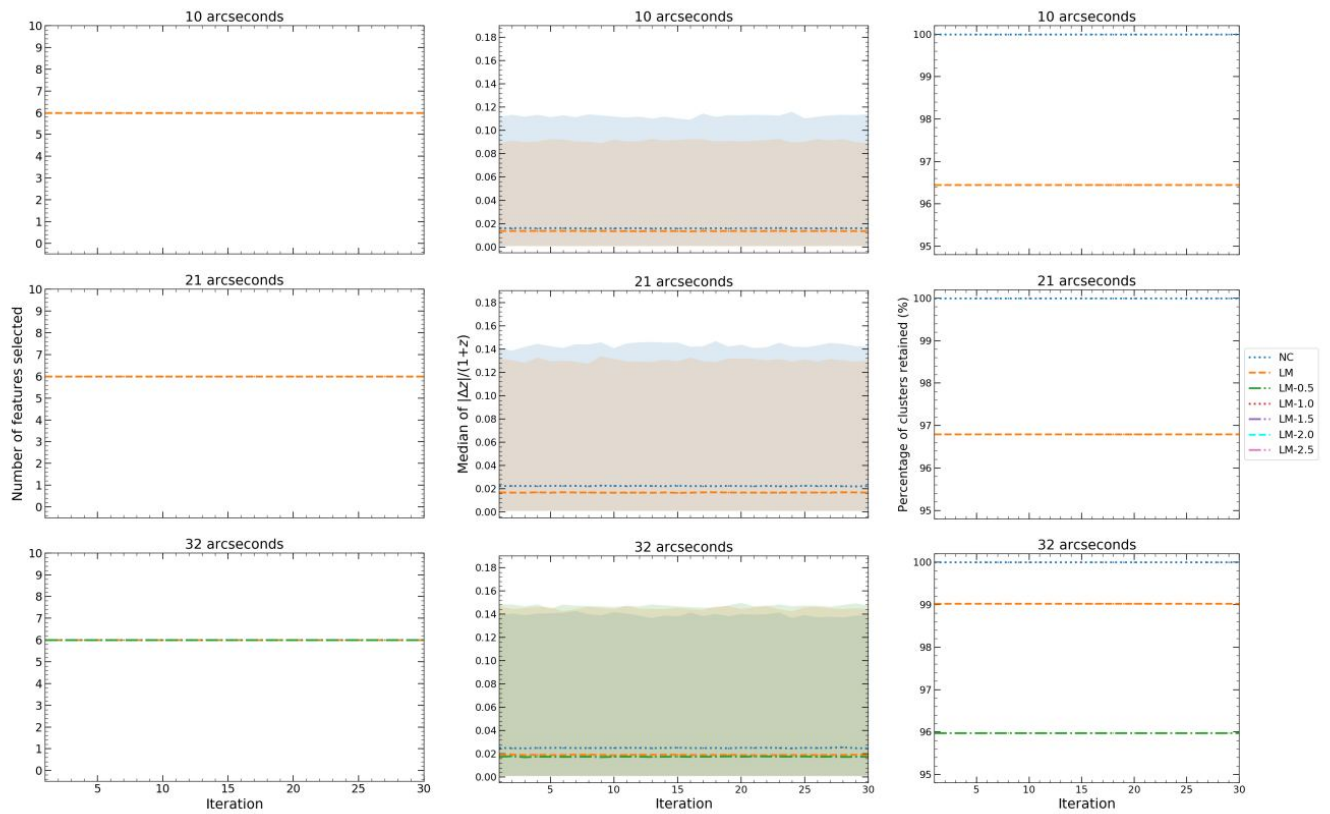
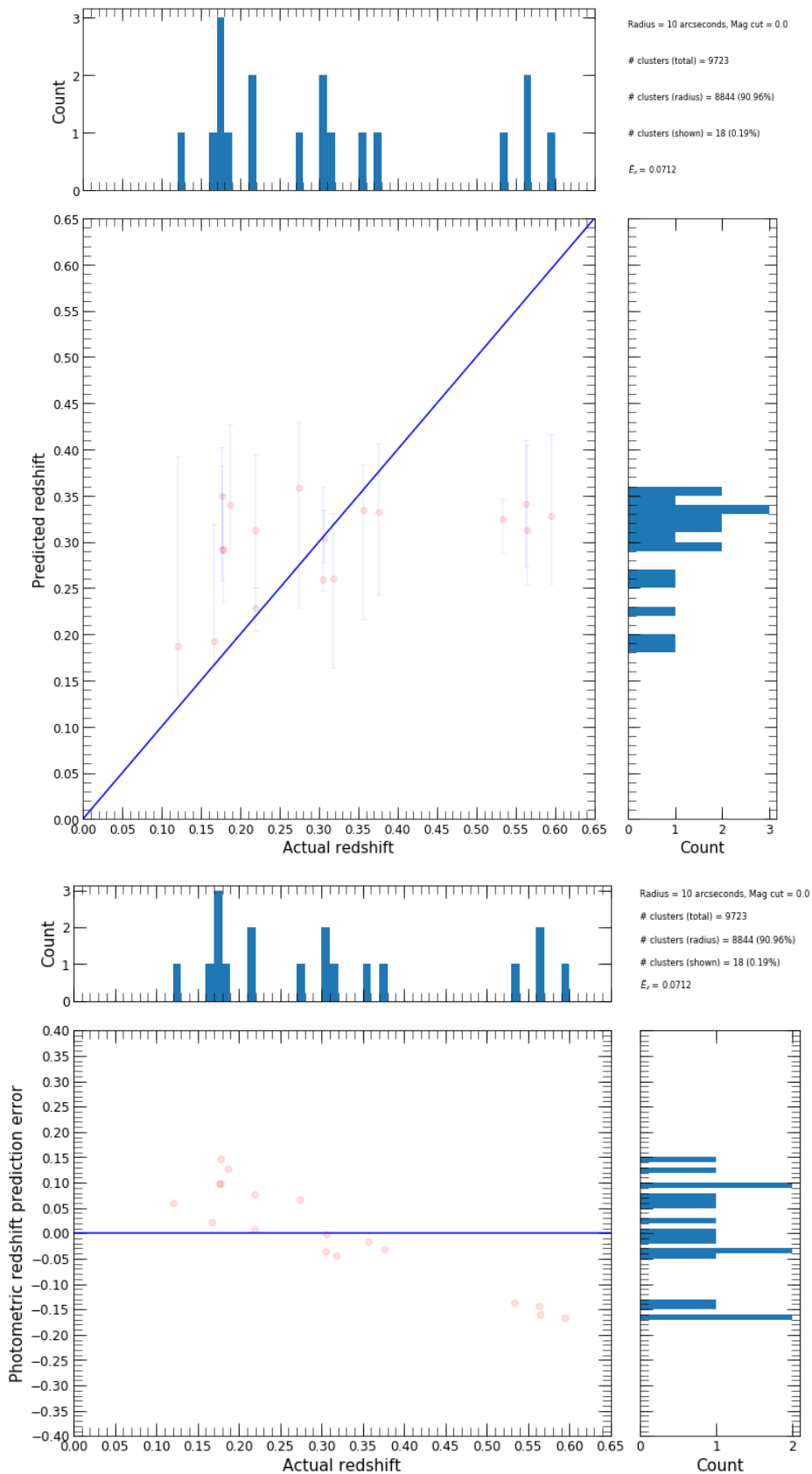


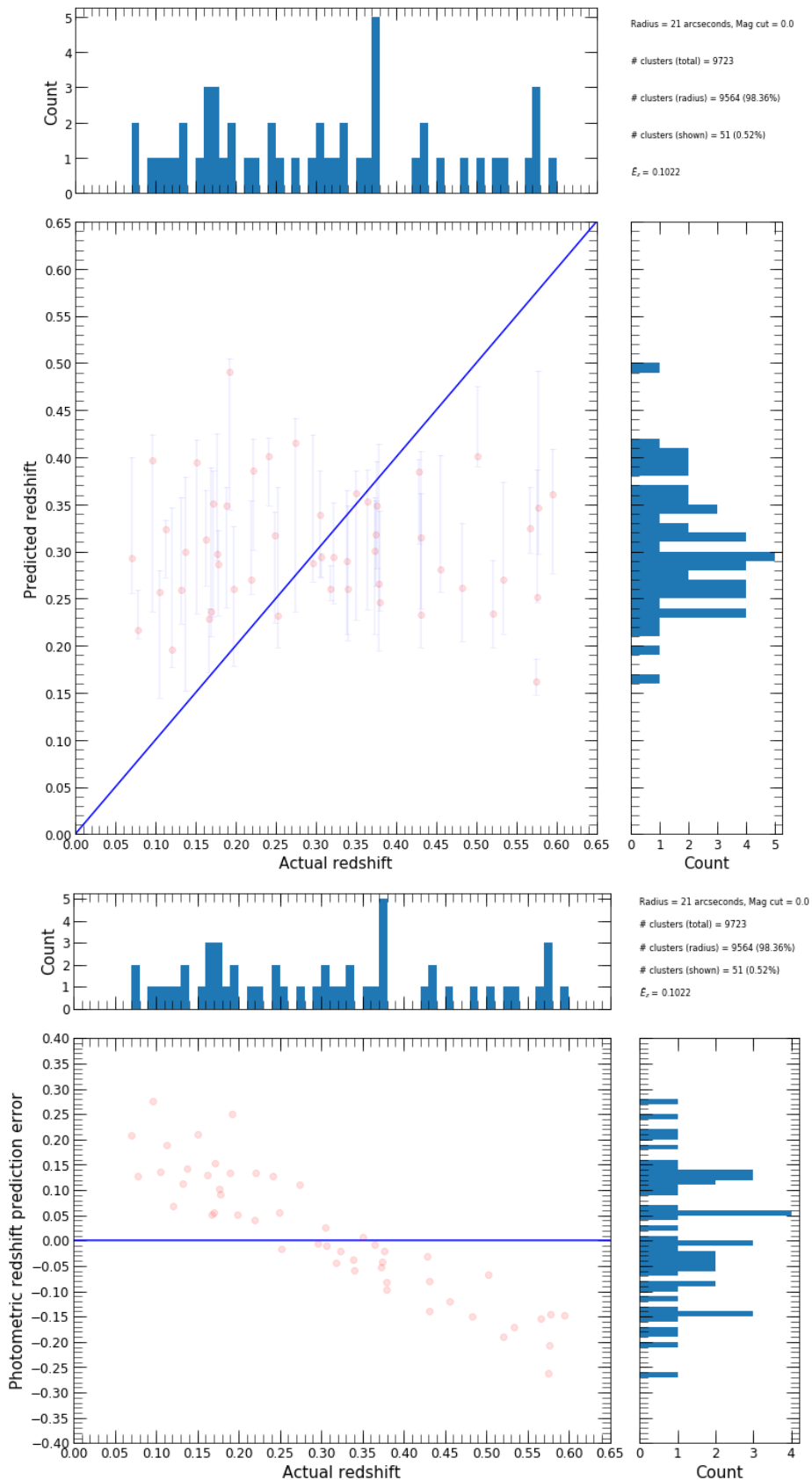
# SUPPLEMENTARY MATERIAL



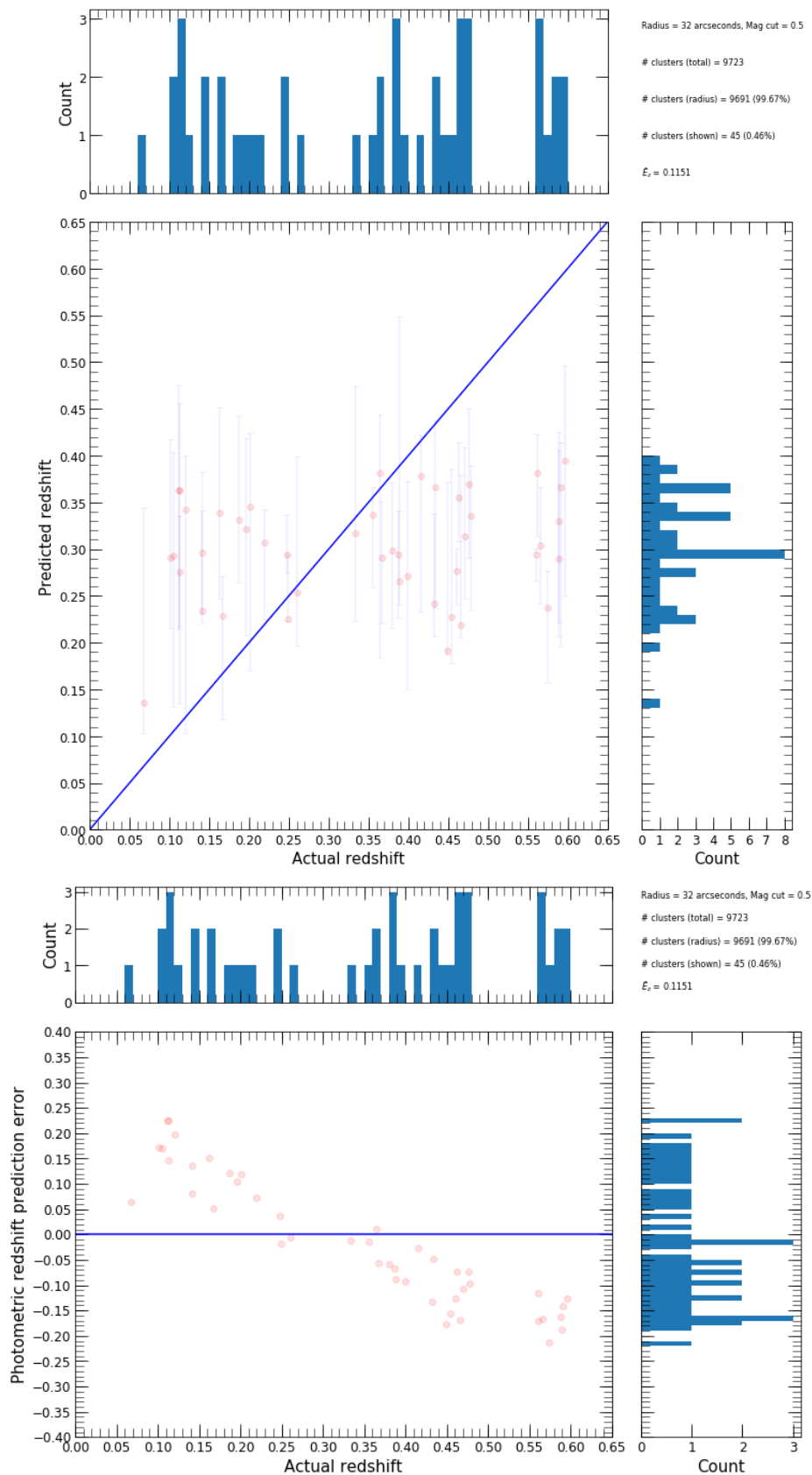
**Figure S1.** This figure displays the results from applying filter magnitude-cuts to the MWAR training set using a single KNN algorithm with a control group of manually selected features for each search radii (10 arcseconds on the top row, 21 arcseconds on the middle row and 32 arcseconds on the bottom row). `NC' represents a dataset with no filter magnitude-cuts applied and `LM' represents the MWAR dataset with SFS selected features where filter magnitude-cuts are applied to the limiting magnitude of SDSS. In addition, `LM' is the faintest filter magnitude-cut whilst `LM-2.5' is the brightest filter magnitude-cut. Left column: Number of features selected for the control group feature subset in ten-fold cross validation across thirty repeats. Middle column: Median of photometric redshift prediction errors ( $|\Delta z|/(1+z)$ ) across all tested clusters for the control group feature subset in ten-fold cross validation across thirty repeats, where the shaded regions represent 95 per cent confidence intervals. Right column: Percentage of test clusters retained after filter magnitude-cuts are applied with the control group feature subset in ten-fold cross validation across thirty repeats. It should be noted that if the percentage of clusters retained, after filter magnitude-cuts are applied, do not satisfy the 95 per cent cluster retention threshold we would not display the corresponding results in the other columns.



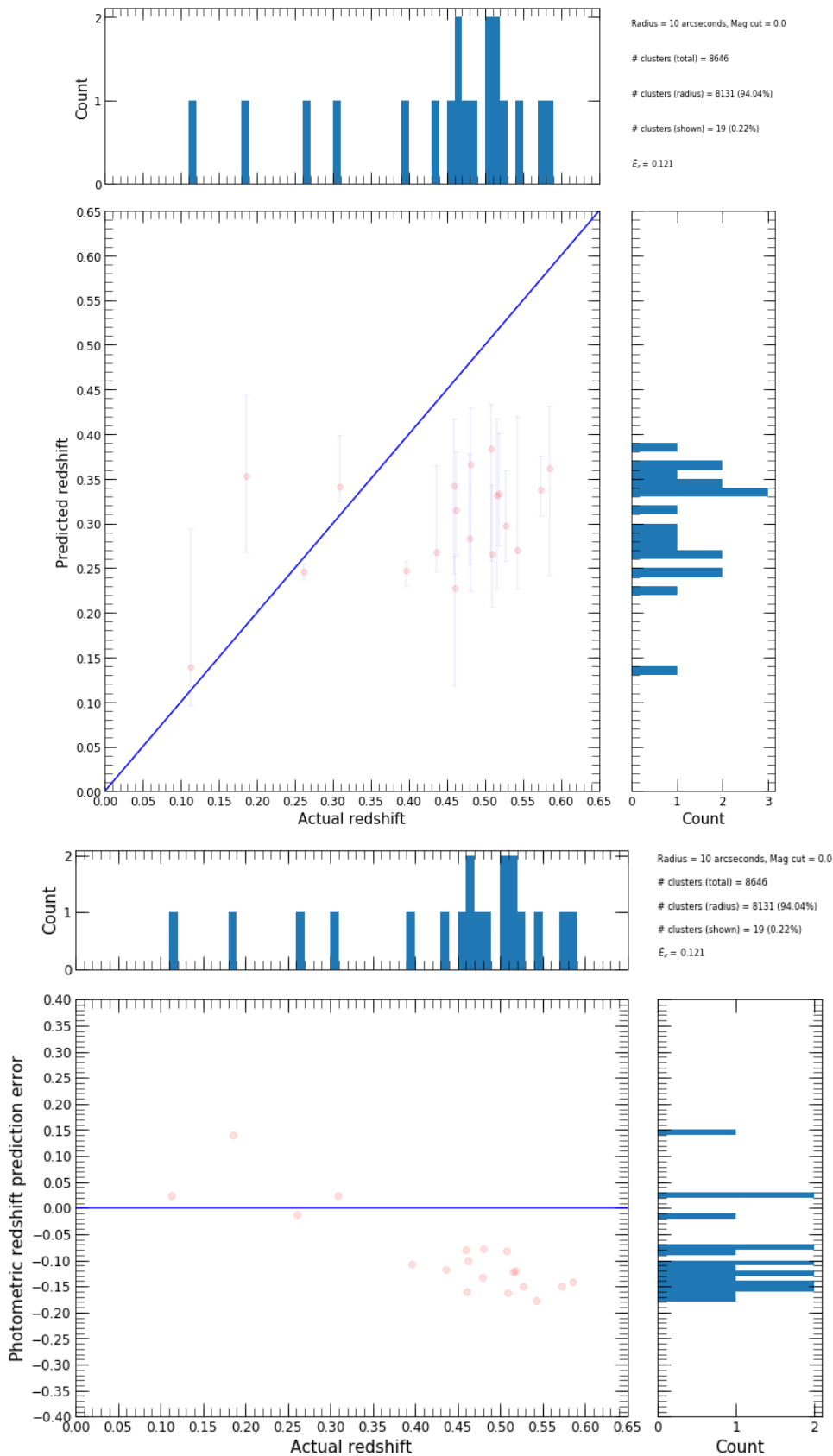
**Figure S2.** This figure displays the performance of photometric redshift predictions of clusters for the WNMR dataset that had partial bootstrap resamples returned within a 10 arcseconds search radius. Top row: Predicted versus 'actual' photometric redshift of tested clusters with frequency histograms of the distributions. Bottom row: Non-absolute photometric redshift prediction error versus 'actual' redshift of tested clusters with frequency histograms of the distributions. Other: '# clusters (total)' represents the total number of clusters in the WNMR dataset, '# clusters (radius)' represents the number of clusters in the WNMR test set that have observed galaxies within a 10 arcseconds search radius, '# clusters (shown)' represents the number of clusters in the WNMR test set that have observed galaxies within a 10 arcseconds search radius with partial bootstrap resamples returned,  $\bar{\epsilon}_z$  represents the median of photometric redshift prediction errors across all tested clusters within a 10 arcseconds search radius with partial bootstrap resamples returned.



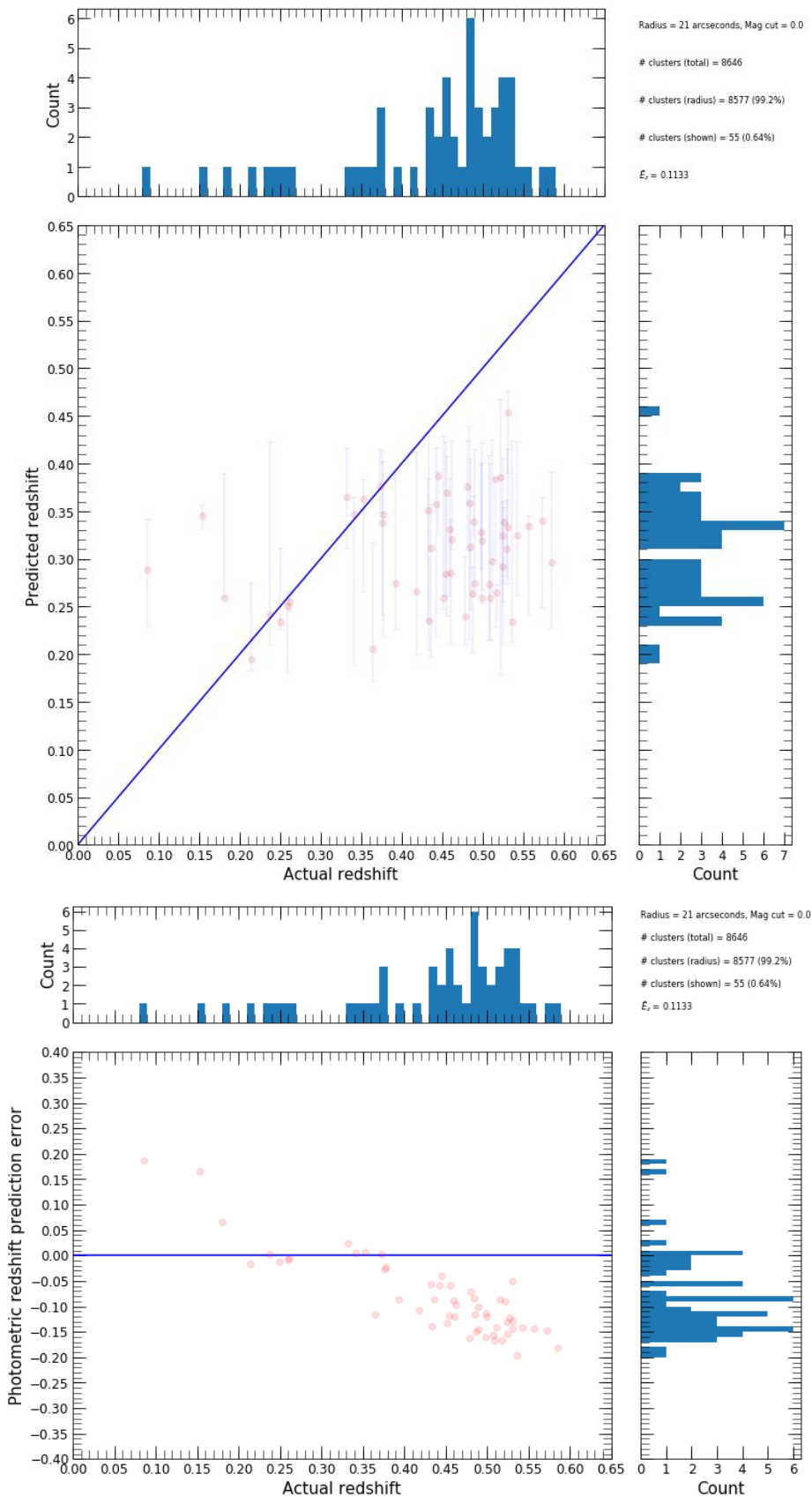
**Figure S3.** This figure displays the performance of photometric redshift predictions of clusters for the WNMR dataset that had partial bootstrap resamples returned within a 21 arcseconds search radius. Top row: Predicted versus 'actual' photometric redshift of tested clusters with frequency histograms of the distributions. Bottom row: Non-absolute photometric redshift prediction error versus 'actual' redshift of tested clusters with frequency histograms of the distributions. Other: '# clusters (total)' represents the total number of clusters in the WNMR dataset, '# clusters (radius)' represents the number of clusters in the WNMR test set that have observed galaxies within a 21 arcseconds search radius, '# clusters (shown)' represents the number of clusters in the WNMR test set that have observed galaxies within a 21 arcseconds search radius with partial bootstrap resamples returned,  $\bar{E}_z$  represents the median of photometric redshift prediction errors across all tested clusters within a 21 arcseconds search radius with partial bootstrap resamples returned.



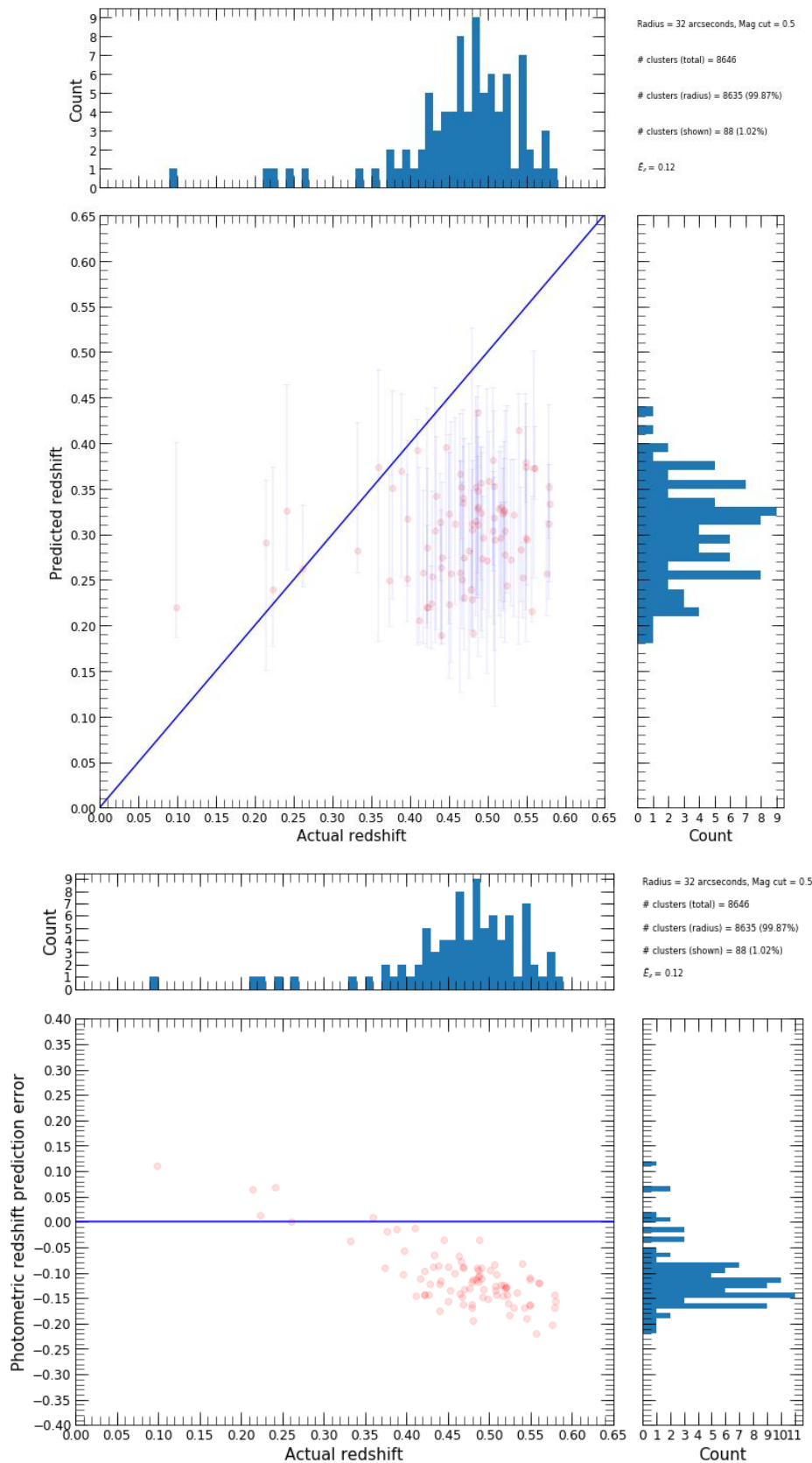
**Figure S4.** This figure displays the performance of photometric redshift predictions of clusters for the WNMR dataset that had partial bootstrap resamples returned within a 32 arcseconds search radius. Top row: Predicted versus 'actual' photometric redshift of tested clusters with frequency histograms of the distributions. Bottom row: Non-absolute photometric redshift prediction error versus 'actual' redshift of tested clusters with frequency histograms of the distributions. Other: '# clusters (total)' represents the total number of clusters in the WNMR dataset, '# clusters (radius)' represents the number of clusters in the WNMR test set that have observed galaxies within a 32 arcseconds search radius, '# clusters (shown)' represents the number of clusters in the WNMR test set that have observed galaxies within a 32 arcseconds search radius with partial bootstrap resamples returned,  $\bar{E}_z$  represents the median of photometric redshift prediction errors across all tested clusters within a 32 arcseconds search radius with partial bootstrap resamples returned.



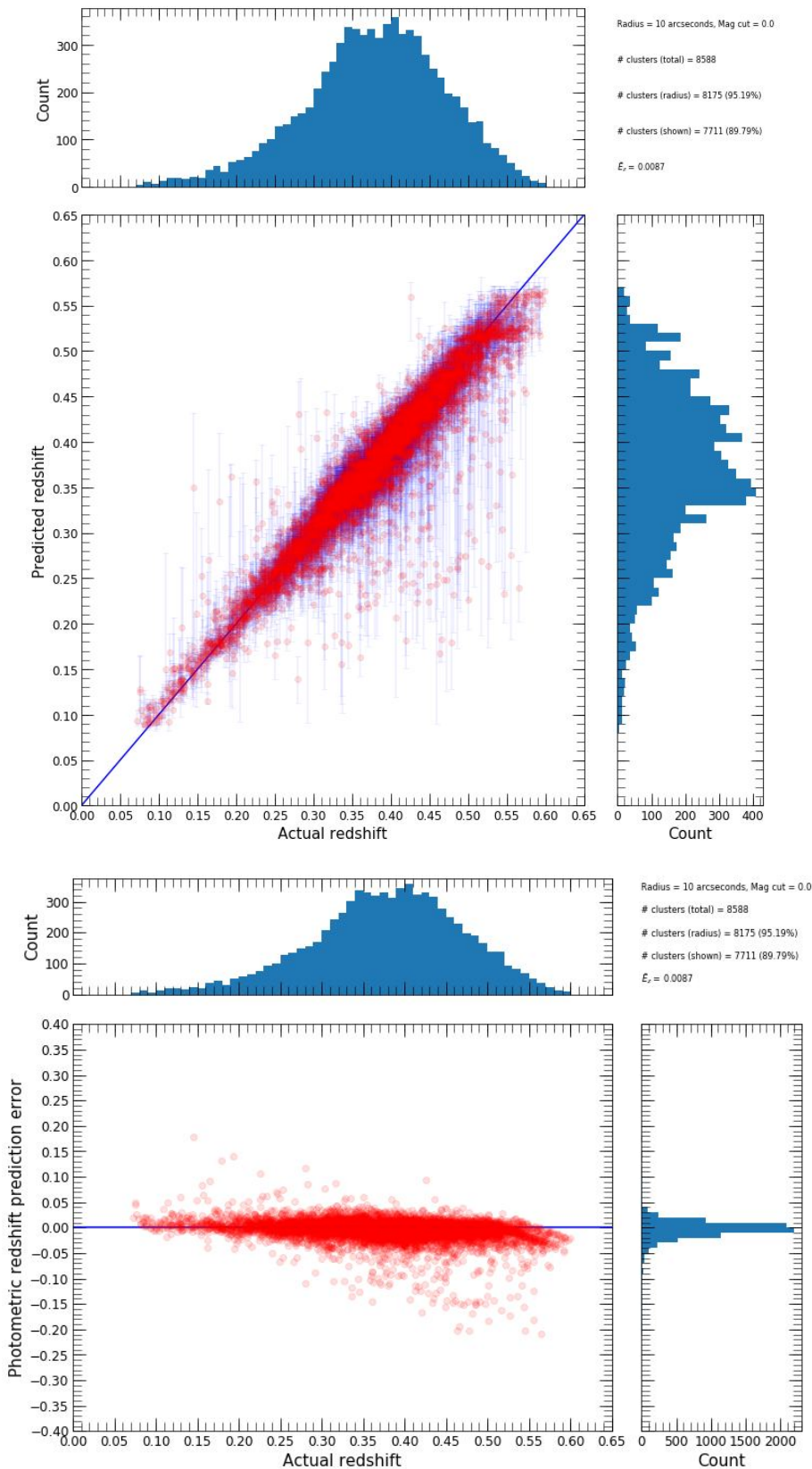
**Figure S5.** This figure displays the performance of photometric redshift predictions of clusters for the RNMW dataset that had partial bootstrap resamples returned within a 10 arcseconds search radius. Top row: Predicted versus 'actual' photometric redshift of tested clusters with frequency histograms of the distributions. Bottom row: Non-absolute photometric redshift prediction error versus 'actual' redshift of tested clusters with frequency histograms of the distributions. Other: '# clusters (total)' represents the total number of clusters in the RNMW dataset, '# clusters (radius)' represents the number of clusters in the RNMW test set that have observed galaxies within a 10 arcseconds search radius, '# clusters (shown)' represents the number of clusters in the RNMW test set that have observed galaxies within a 10 arcseconds search radius with partial bootstrap resamples returned,  $\bar{\epsilon}_z$  represents the median of photometric redshift prediction errors across all tested clusters within a 10 arcseconds search radius with partial bootstrap resamples returned.



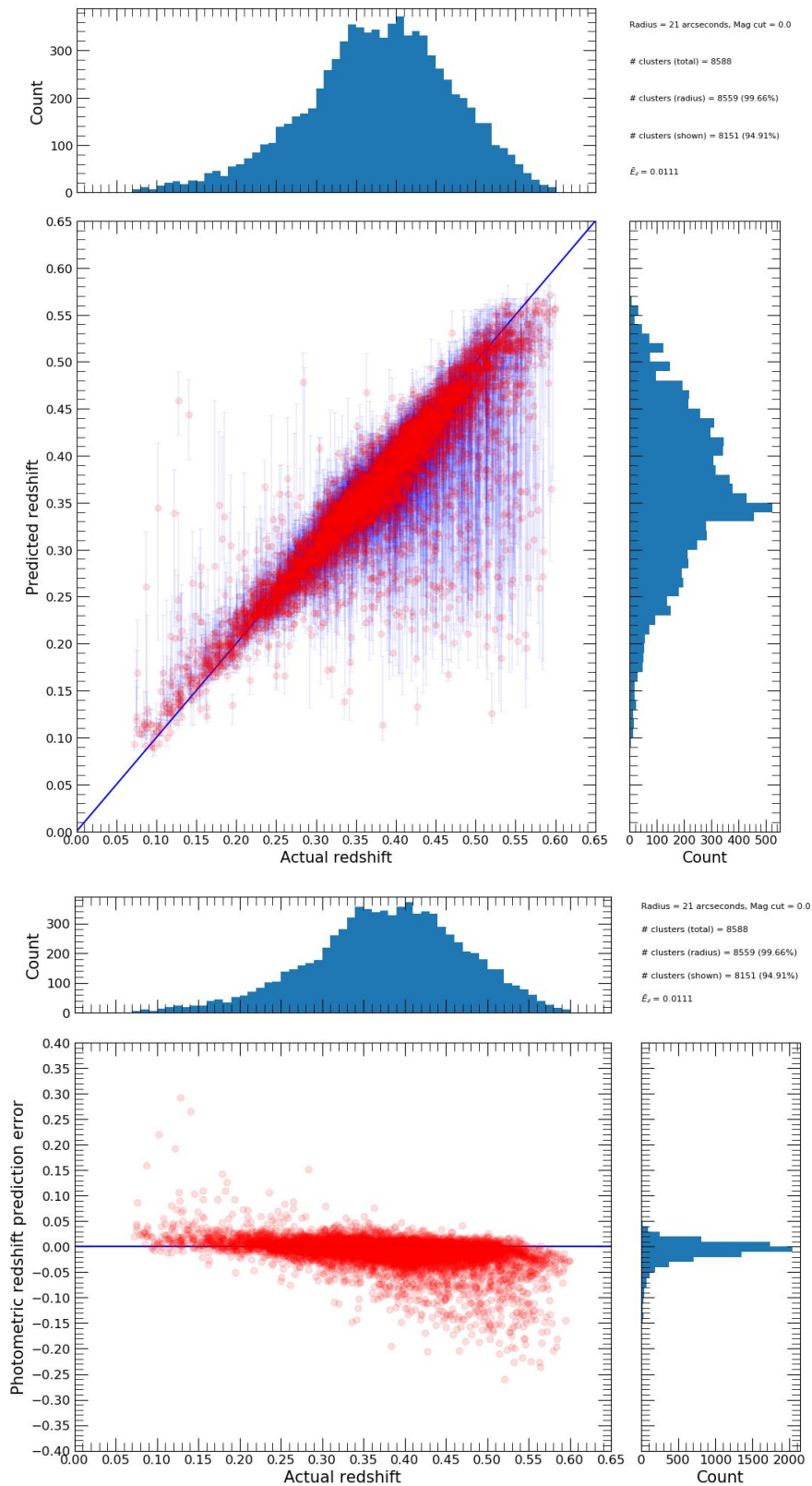
**Figure S6.** This figure displays the performance of photometric redshift predictions of clusters for the RNMW dataset that had partial bootstrap resamples returned within a 21 arcseconds search radius. Top row: Predicted versus 'actual' photometric redshift of tested clusters with frequency histograms of the distributions. Bottom row: Non-absolute photometric redshift prediction error versus 'actual' redshift of tested clusters with frequency histograms of the distributions. Other: '# clusters (total)' represents the total number of clusters in the RNMW dataset, '# clusters (radius)' represents the number of clusters in the RNMW test set that have observed galaxies within a 21 arcseconds search radius, '# clusters (shown)' represents the number of clusters in the RNMW test set that have observed galaxies within a 21 arcseconds search radius with partial bootstrap resamples returned,  $\bar{E}_z$  represents the median of photometric redshift prediction errors across all tested clusters within a 21 arcseconds search radius with partial bootstrap resamples returned.



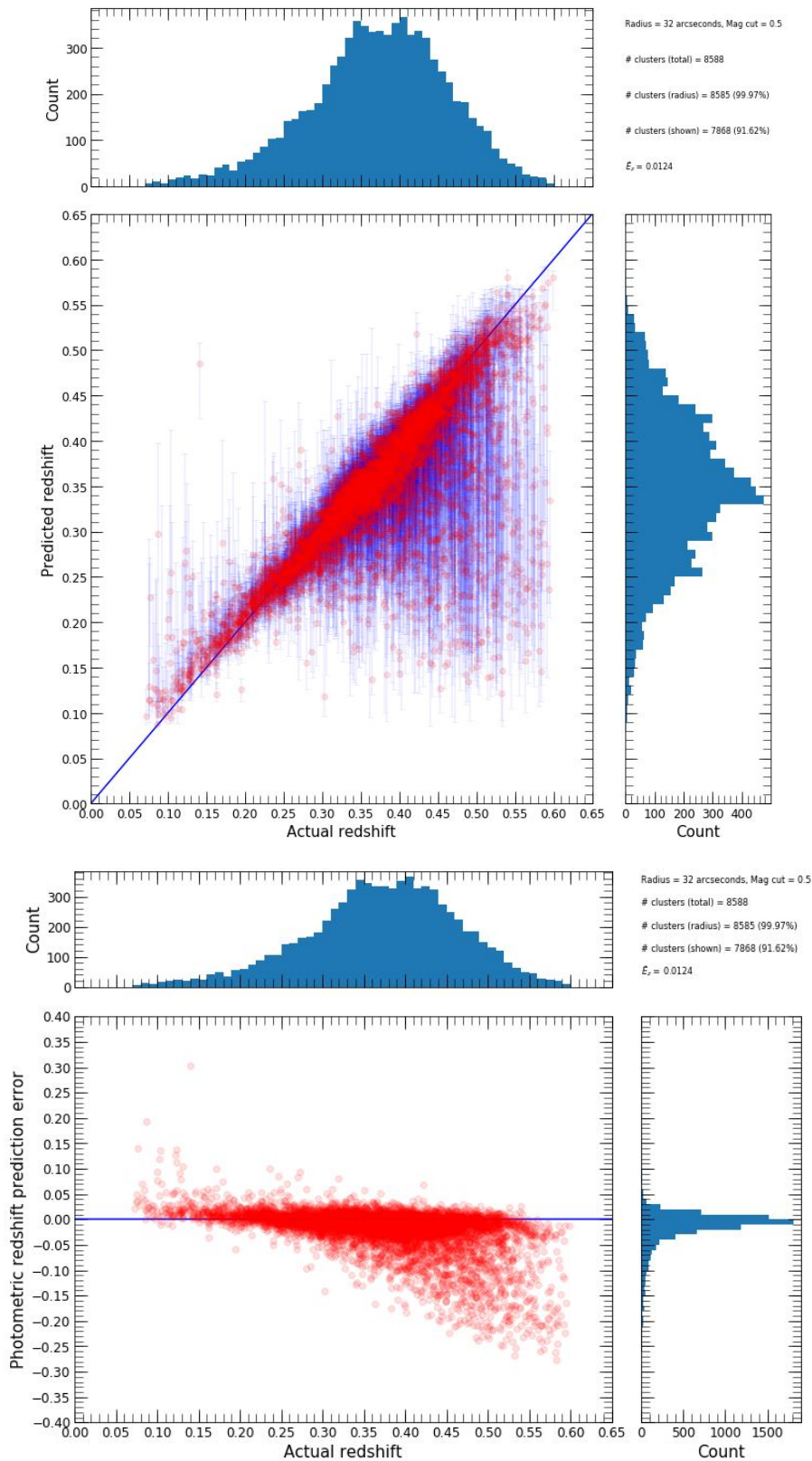
**Figure S7.** This figure displays the performance of photometric redshift predictions of clusters for the RNMW dataset that had partial bootstrap resamples returned within a 32 arcseconds search radius. Top row: Predicted versus 'actual' photometric redshift of tested clusters with frequency histograms of the distributions. Bottom row: Non-absolute photometric redshift prediction error versus 'actual' redshift of tested clusters with frequency histograms of the distributions. Other: '# clusters (total)' represents the total number of clusters in the RNMW dataset, '# clusters (radius)' represents the number of clusters in the RNMW test set that have observed galaxies within a 32 arcseconds search radius, '# clusters (shown)' represents the number of clusters in the RNMW test set that have observed galaxies within a 32 arcseconds search radius with partial bootstrap resamples returned,  $\bar{\epsilon}_z$  represents the median of photometric redshift prediction errors across all tested clusters within a 32 arcseconds search radius with partial bootstrap resamples returned.



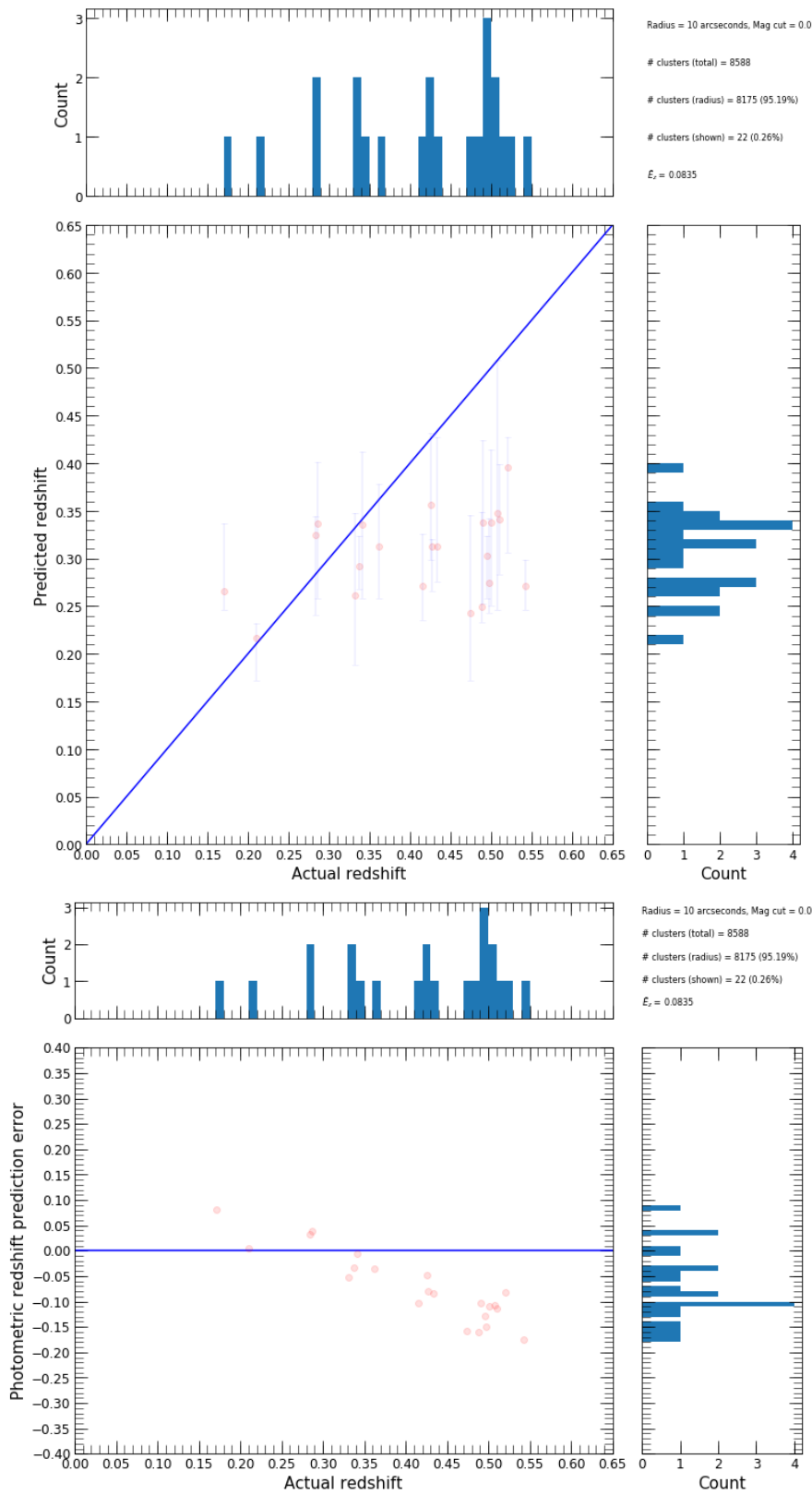
**Figure S8.** This figure displays the performance of photometric redshift predictions of clusters with low richness, which did not qualify for the MWAR dataset, that had full bootstrap resamples returned within a 10 arcseconds search radius. Top row: Predicted versus 'actual' photometric redshift of tested clusters with frequency histograms of the distributions. Bottom row: Non-absolute photometric redshift prediction error versus 'actual' redshift of tested clusters with frequency histograms of the distributions. Other: '# clusters (total)' represents the total number of clusters with low richness which did not qualify for the MWAR dataset, '# clusters (radius)' represents the number of clusters with low richness which did not qualify for the MWAR dataset that have observed galaxies within a 10 arcseconds search radius, '# clusters (shown)' represents the number of clusters with low richness which did not qualify for the MWAR dataset that have observed galaxies within a 10 arcseconds search radius with full bootstrap resamples returned,  $\bar{E}_z$  represents the median of photometric redshift prediction errors across all tested clusters within a 10 arcseconds search radius with full bootstrap resamples returned.



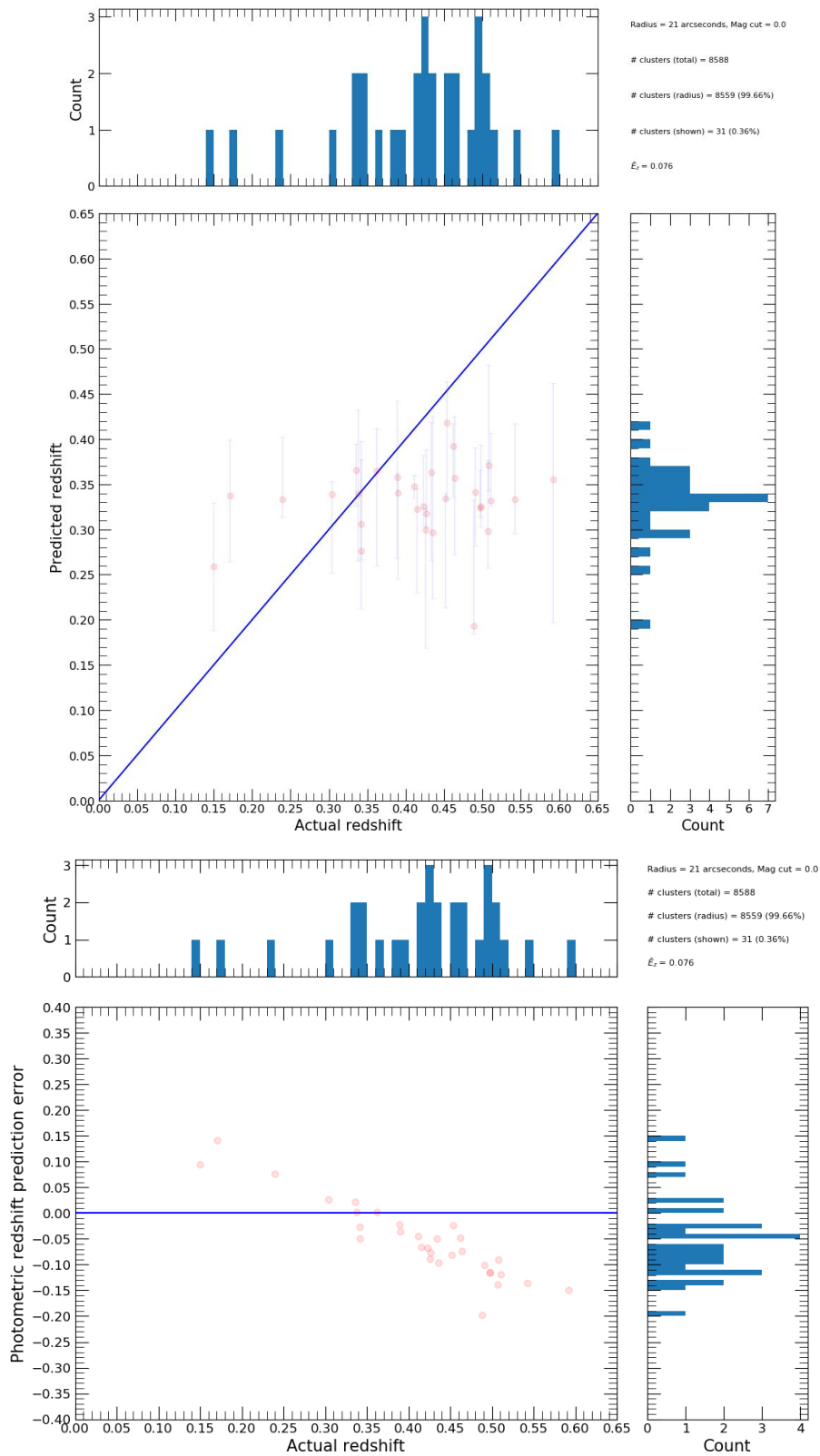
**Figure S9.** This figure displays the performance of photometric redshift predictions of clusters with low richness, which did not qualify for the MWAR dataset, that had full bootstrap resamples returned within a 21 arcseconds search radius. Top row: Predicted versus 'actual' photometric redshift of tested clusters with frequency histograms of the distributions. Bottom row: Non-absolute photometric redshift prediction error versus 'actual' redshift of tested clusters with frequency histograms of the distributions. Other: '# clusters (total)' represents the total number of clusters with low richness which did not qualify for the MWAR dataset, '# clusters (radius)' represents the number of clusters with low richness which did not qualify for the MWAR dataset that have observed galaxies within a 21 arcseconds search radius, '# clusters (shown)' represents the number of clusters with low richness which did not qualify for the MWAR dataset that have observed galaxies within a 21 arcseconds search radius with full bootstrap resamples returned,  $\bar{E}_z$  represents the median of photometric redshift prediction errors across all tested clusters within a 21 arcseconds search radius with full bootstrap resamples returned.



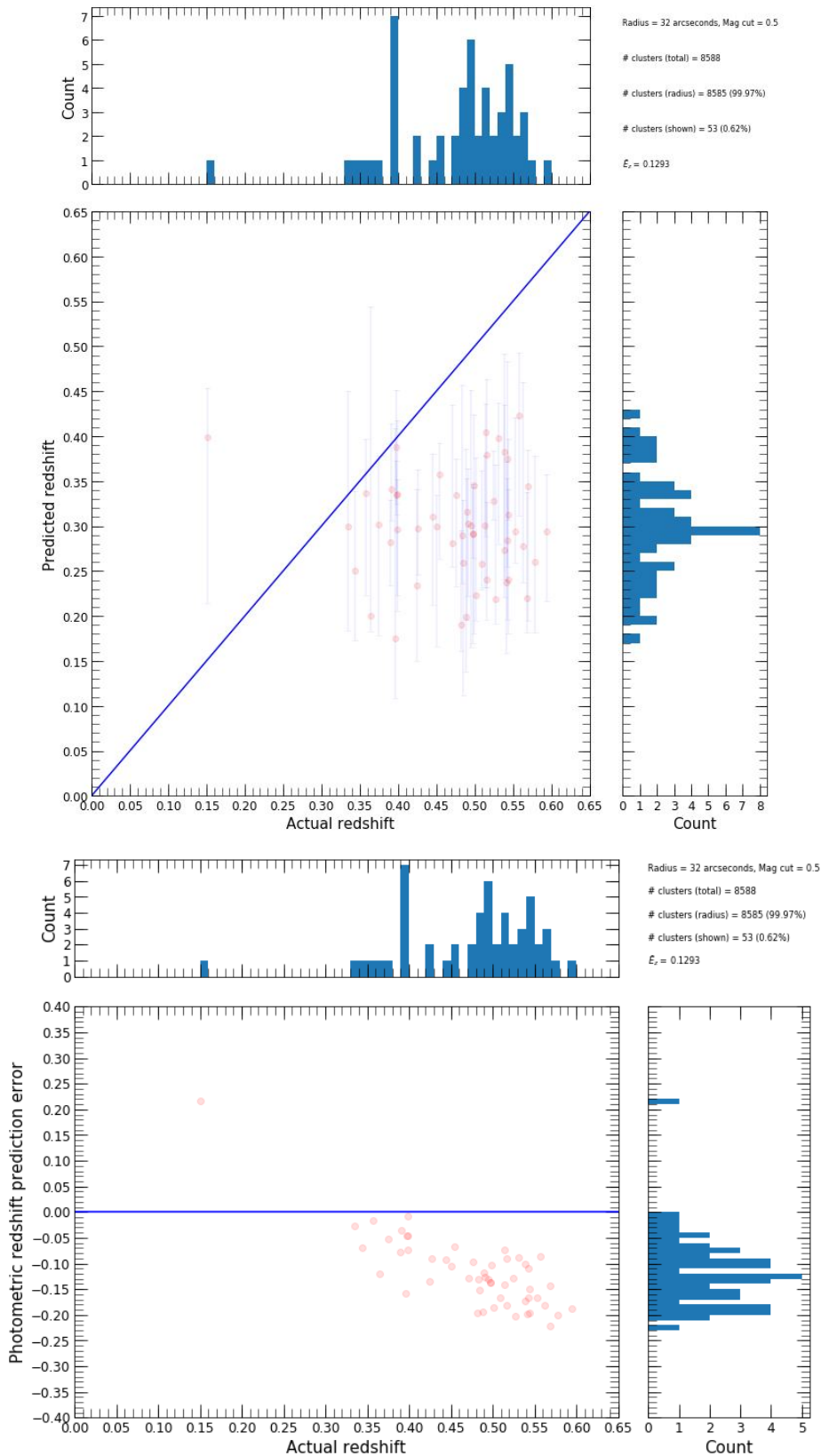
**Figure S10.** This figure displays the performance of photometric redshift predictions of clusters with low richness, which did not qualify for the MWAR dataset, that had full bootstrap resamples returned within a 32 arcseconds search radius. Top row: Predicted versus 'actual' photometric redshift of tested clusters with frequency histograms of the distributions. Bottom row: Non-absolute photometric redshift prediction error versus 'actual' redshift of tested clusters with frequency histograms of the distributions. Other: '# clusters (total)' represents the total number of clusters with low richness which did not qualify for the MWAR dataset, '# clusters (radius)' represents the number of clusters with low richness which did not qualify for the MWAR dataset that have observed galaxies within a 32 arcseconds search radius, '# clusters (shown)' represents the number of clusters with low richness which did not qualify for the MWAR dataset that have observed galaxies within a 32 arcseconds search radius with full bootstrap resamples returned,  $\tilde{E}_z$  represents the median of photometric redshift prediction errors across all tested clusters within a 32 arcseconds search radius with full bootstrap resamples returned.



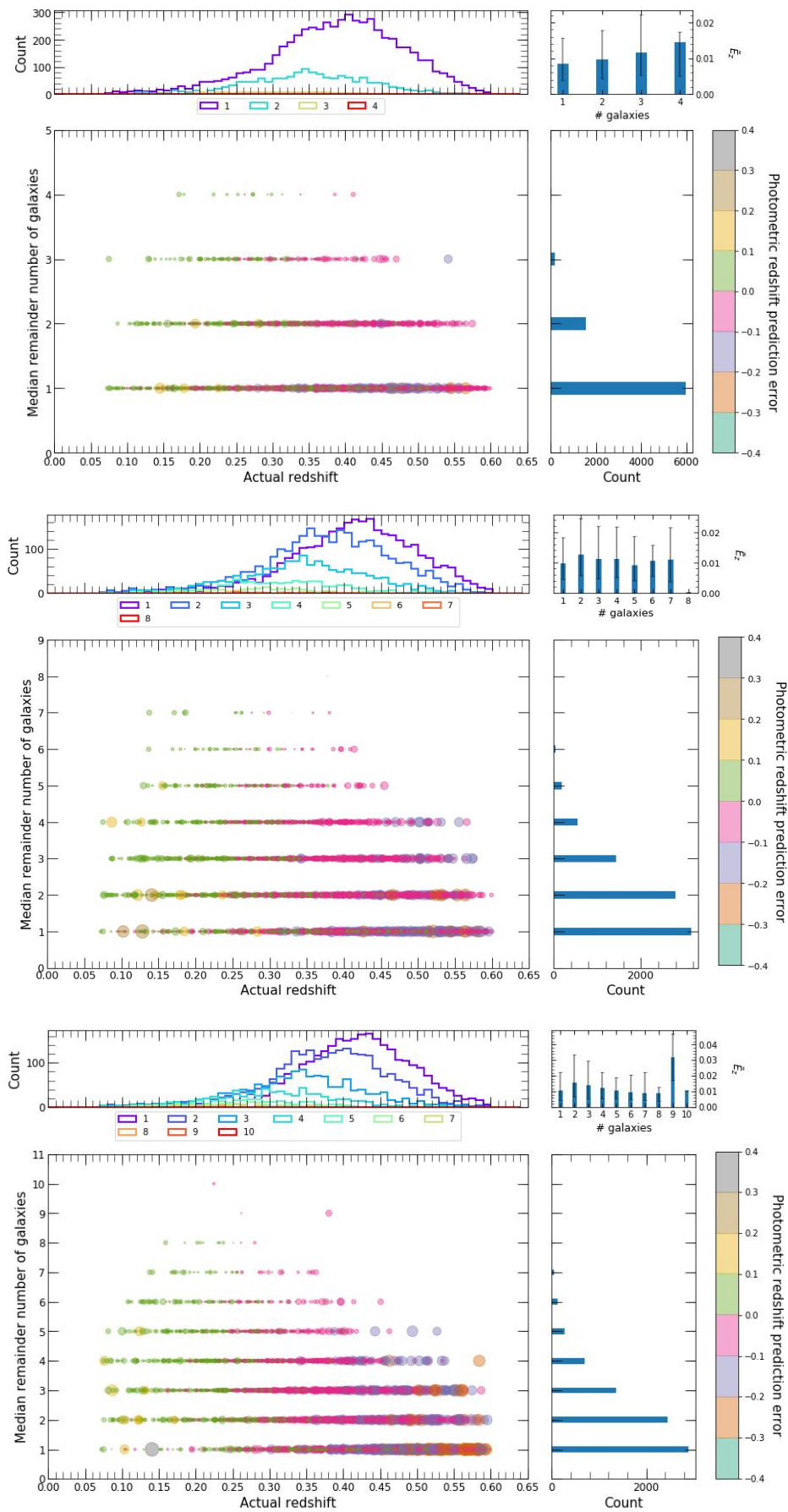
**Figure S11.** This figure displays the performance of photometric redshift predictions of clusters with low richness, which did not qualify for the MWAR dataset, that had partial bootstrap resamples returned within a 10 arcseconds search radius. Top row: Predicted versus 'actual' photometric redshift of tested clusters with frequency histograms of the distributions. Bottom row: Non-absolute photometric redshift prediction error versus 'actual' redshift of tested clusters with frequency histograms of the distributions. Other: '# clusters (total)' represents the total number of clusters with low richness which did not qualify for the MWAR dataset, '# clusters (radius)' represents the number of clusters with low richness which did not qualify for the MWAR dataset that have observed galaxies within a 10 arcseconds search radius, '# clusters (shown)' represents the number of clusters with low richness which did not qualify for the MWAR dataset that have observed galaxies within a 10 arcseconds search radius with partial bootstrap resamples returned,  $\bar{E}_z$  represents the median of photometric redshift prediction errors across all tested clusters within a 10 arcseconds search radius with partial bootstrap resamples returned.



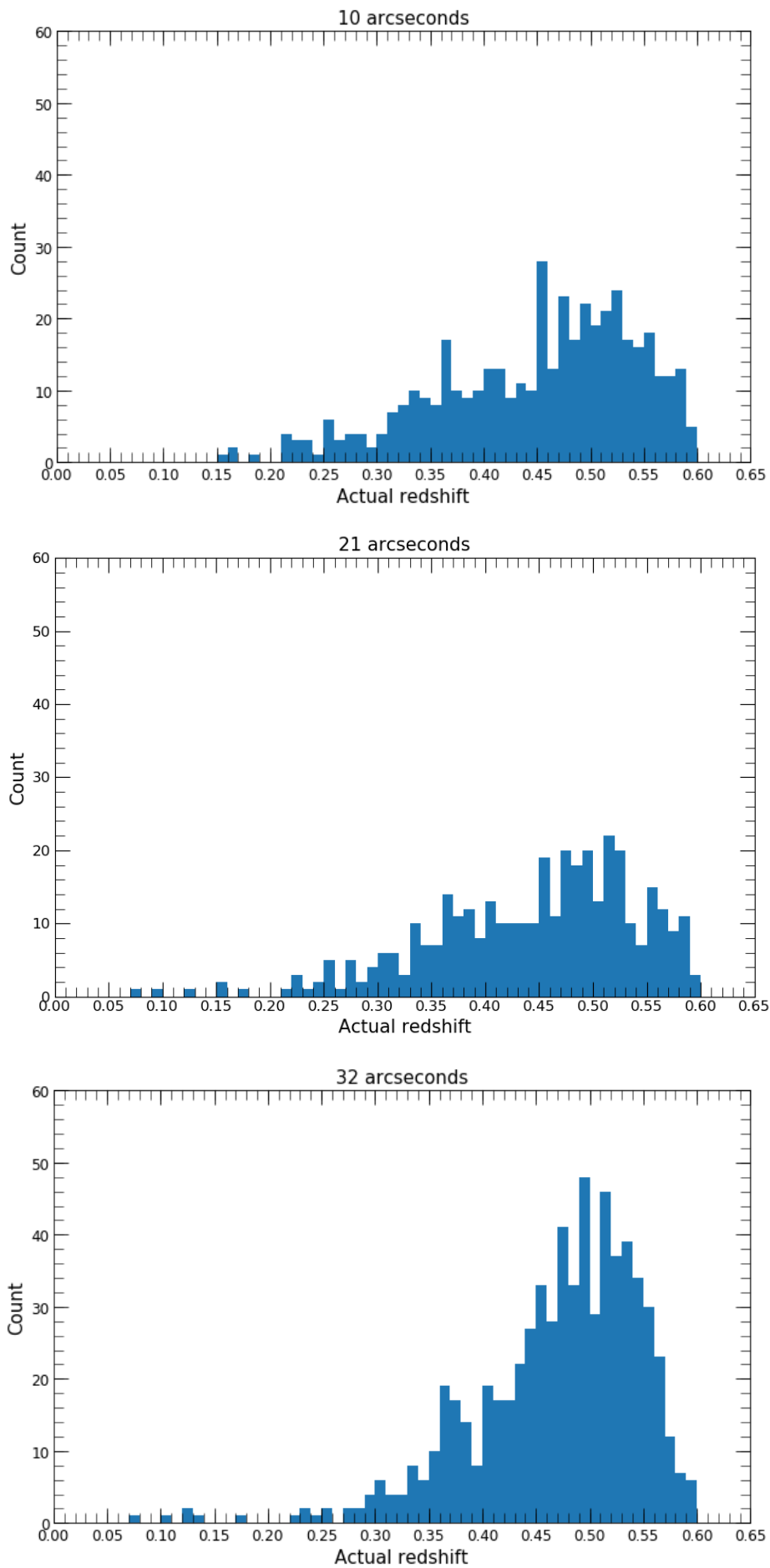
**Figure S12.** This figure displays the performance of photometric redshift predictions of clusters with low richness, which did not qualify for the MWAR dataset, that had partial bootstrap resamples returned within a 21 arcseconds search radius. Top row: Predicted versus 'actual' photometric redshift of tested clusters with frequency histograms of the distributions. Bottom row: Non-absolute photometric redshift prediction error versus 'actual' redshift of tested clusters with frequency histograms of the distributions. Other: '# clusters (total)' represents the total number of clusters with low richness which did not qualify for the MWAR dataset, '# clusters (radius)' represents the number of clusters with low richness which did not qualify for the MWAR dataset that have observed galaxies within a 21 arcseconds search radius, '# clusters (shown)' represents the number of clusters with low richness which did not qualify for the MWAR dataset that have observed galaxies within a 21 arcseconds search radius with partial bootstrap resamples returned,  $\tilde{E}_z$  represents the median of photometric redshift prediction errors across all tested clusters within a 21 arcseconds search radius with partial bootstrap resamples returned.



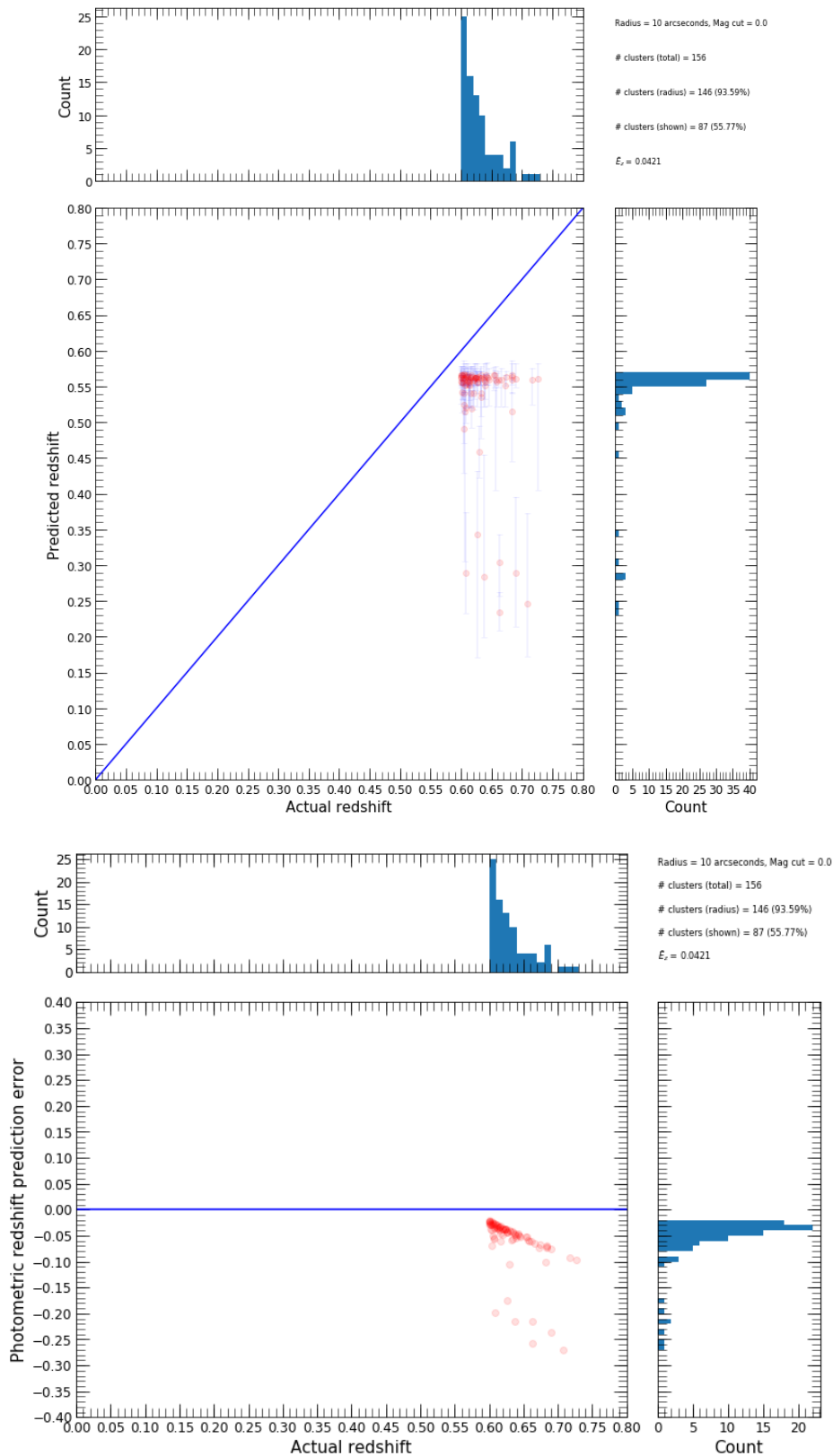
**Figure S13.** This figure displays the performance of photometric redshift predictions of clusters with low richness, which did not qualify for the MWAR dataset, that had partial bootstrap resamples returned within a 32 arcseconds search radius. Top row: Predicted versus 'actual' photometric redshift of tested clusters with frequency histograms of the distributions. Bottom row: Non-absolute photometric redshift prediction error versus 'actual' redshift of tested clusters with frequency histograms of the distributions. Other: '# clusters (total)' represents the total number of clusters with low richness which did not qualify for the MWAR dataset, '# clusters (radius)' represents the number of clusters with low richness which did not qualify for the MWAR dataset that have observed galaxies within a 32 arcseconds search radius, '# clusters (shown)' represents the number of clusters with low richness which did not qualify for the MWAR dataset that have observed galaxies within a 32 arcseconds search radius with partial bootstrap resamples returned,  $\bar{E}_z$  represents the median of photometric redshift prediction errors across all tested clusters within a 32 arcseconds search radius with partial bootstrap resamples returned.



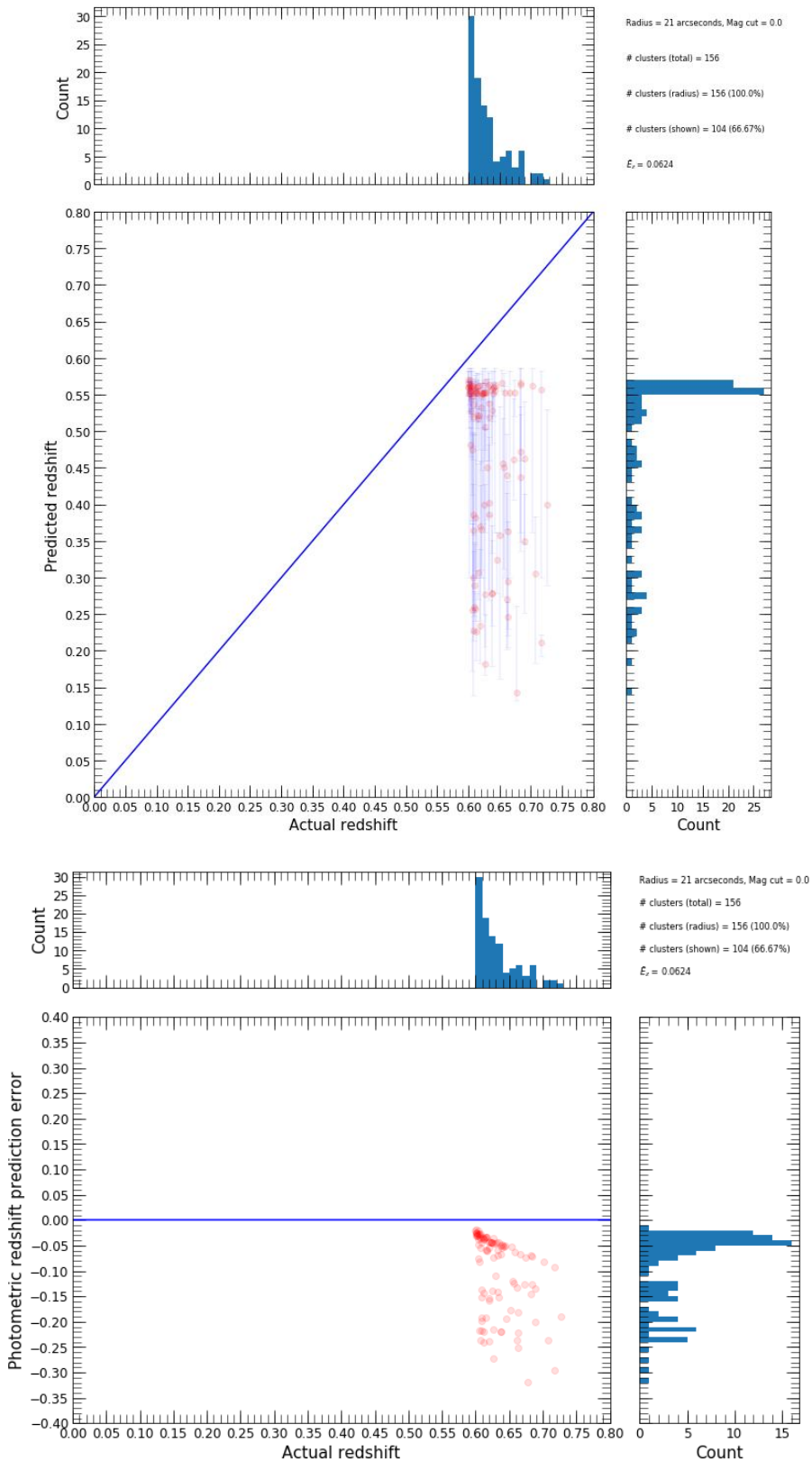
**Figure S14.** This figure displays the number of galaxies used in photometric redshift predictions of clusters with low richness versus ‘actual’ redshift of tested clusters, which did not qualify for the MWAR dataset, where predictions had full bootstrap resamples returned within a 10 (top row), 21 (middle row) and 32 (bottom row) arcseconds search radius. It should be noted that the size of individual points change in relation to the value of the non-absolute photometric redshift prediction error. Frequency histograms of the distributions are also shown.  $\tilde{E}_z$  represents the median of photometric redshift prediction errors across all tested clusters for each number of galaxies bin.



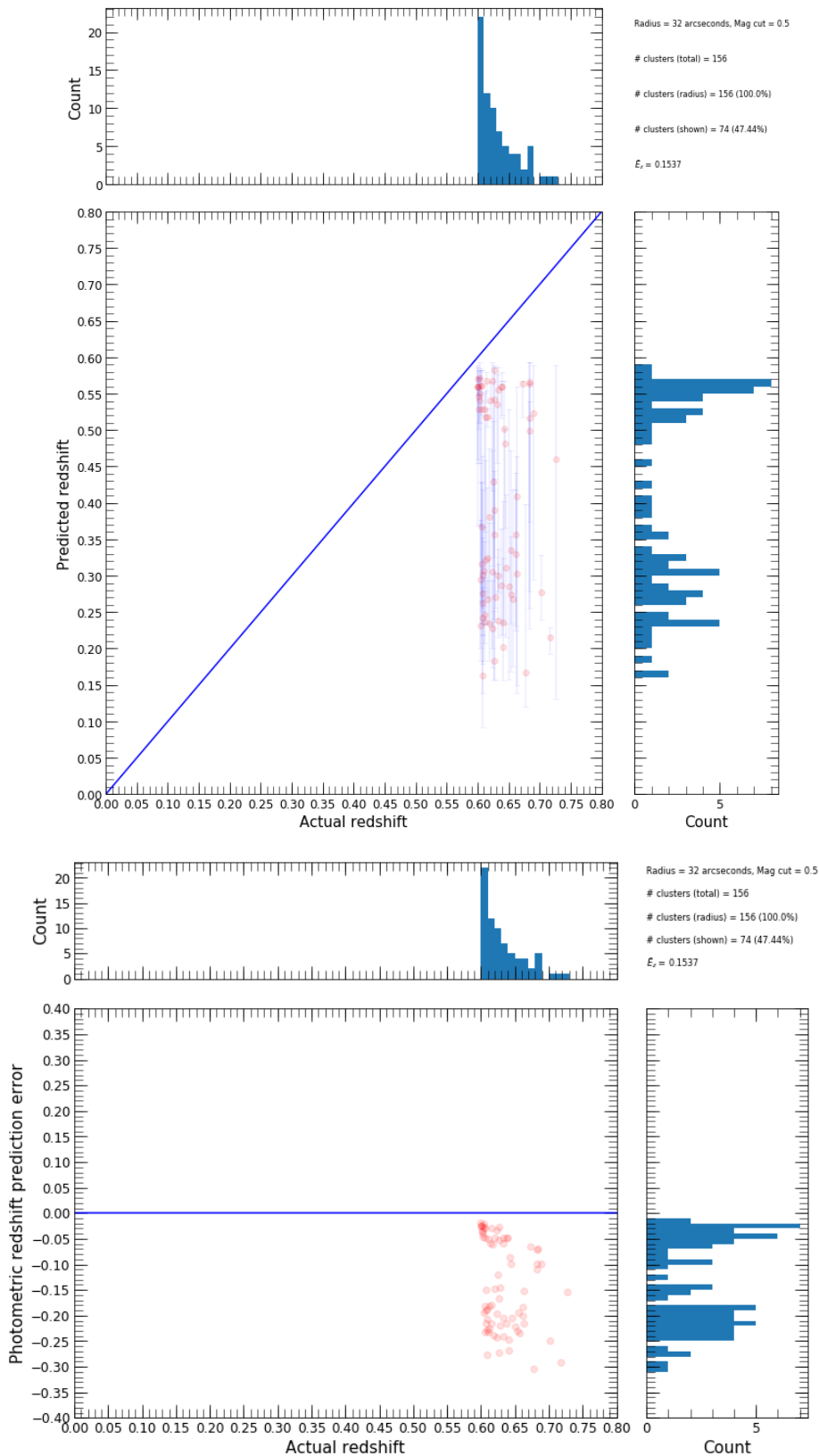
**Figure S15.** This figure displays the ‘actual’ redshift distributions of clusters with low richness, which did not qualify for the MWAR dataset, that had no bootstrap resamples returned within a 10 (top row), 21 (middle row) and 32 (bottom row) arcseconds search radius.



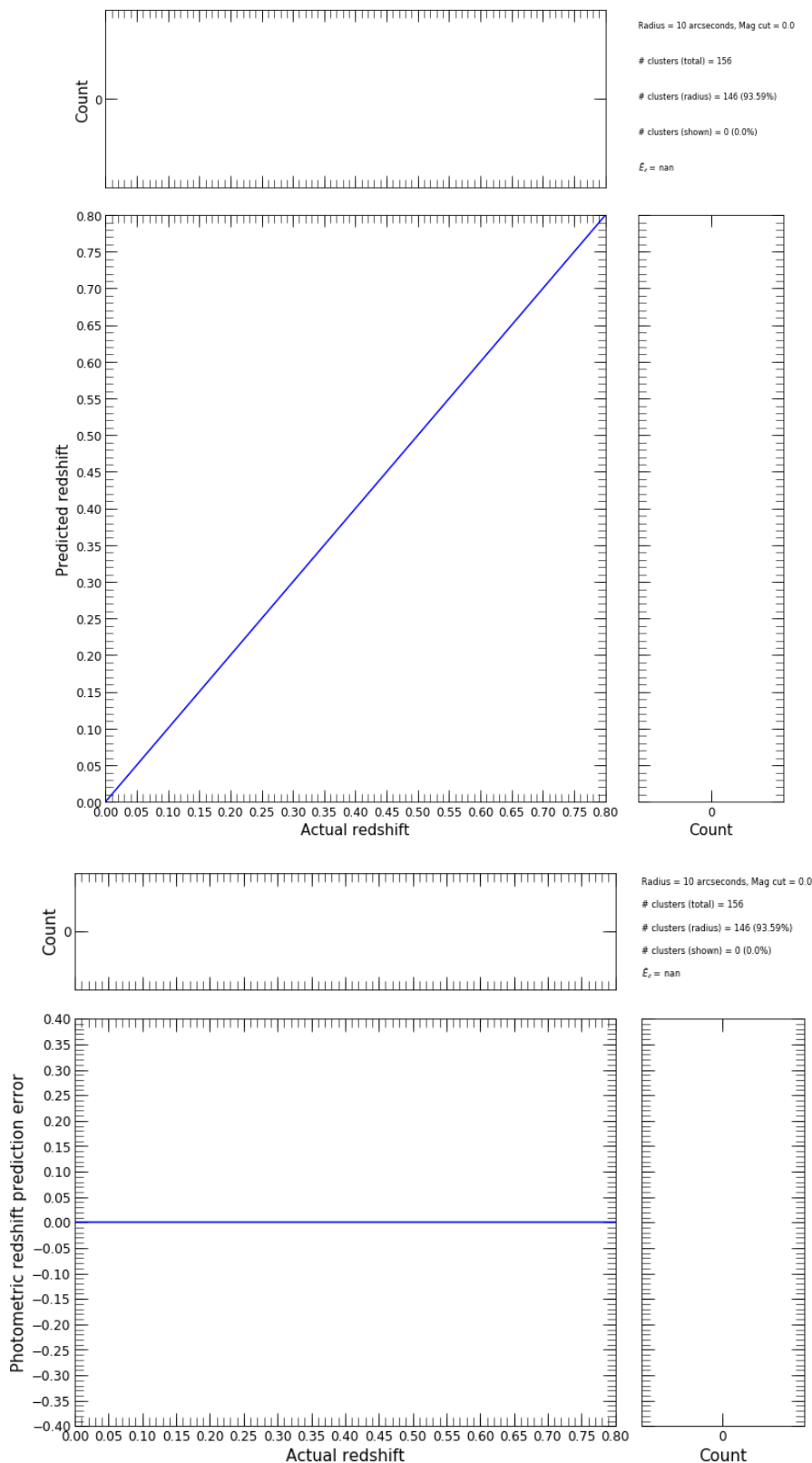
**Figure S16.** This figure displays the performance of photometric redshift predictions of clusters at high redshift, which did not qualify for the WNMR dataset, that had full bootstrap resamples returned within a 10 arcseconds search radius. Top row: Predicted versus 'actual' photometric redshift of tested clusters with frequency histograms of the distributions. Bottom row: Non-absolute photometric redshift prediction error versus 'actual' redshift of tested clusters with frequency histograms of the distributions. Other: '# clusters (total)' represents the total number of clusters at high redshift which did not qualify for the WNMR dataset, '# clusters (radius)' represents the number of clusters at high redshift which did not qualify for the WNMR dataset that have observed galaxies within a 10 arcseconds search radius, '# clusters (shown)' represents the number of clusters at high redshift which did not qualify for the WNMR dataset that have observed galaxies within a 10 arcseconds search radius with full bootstrap resamples returned,  $\bar{E}_z$  represents the median of photometric redshift prediction errors across all tested clusters within a 10 arcseconds search radius with full bootstrap resamples returned.



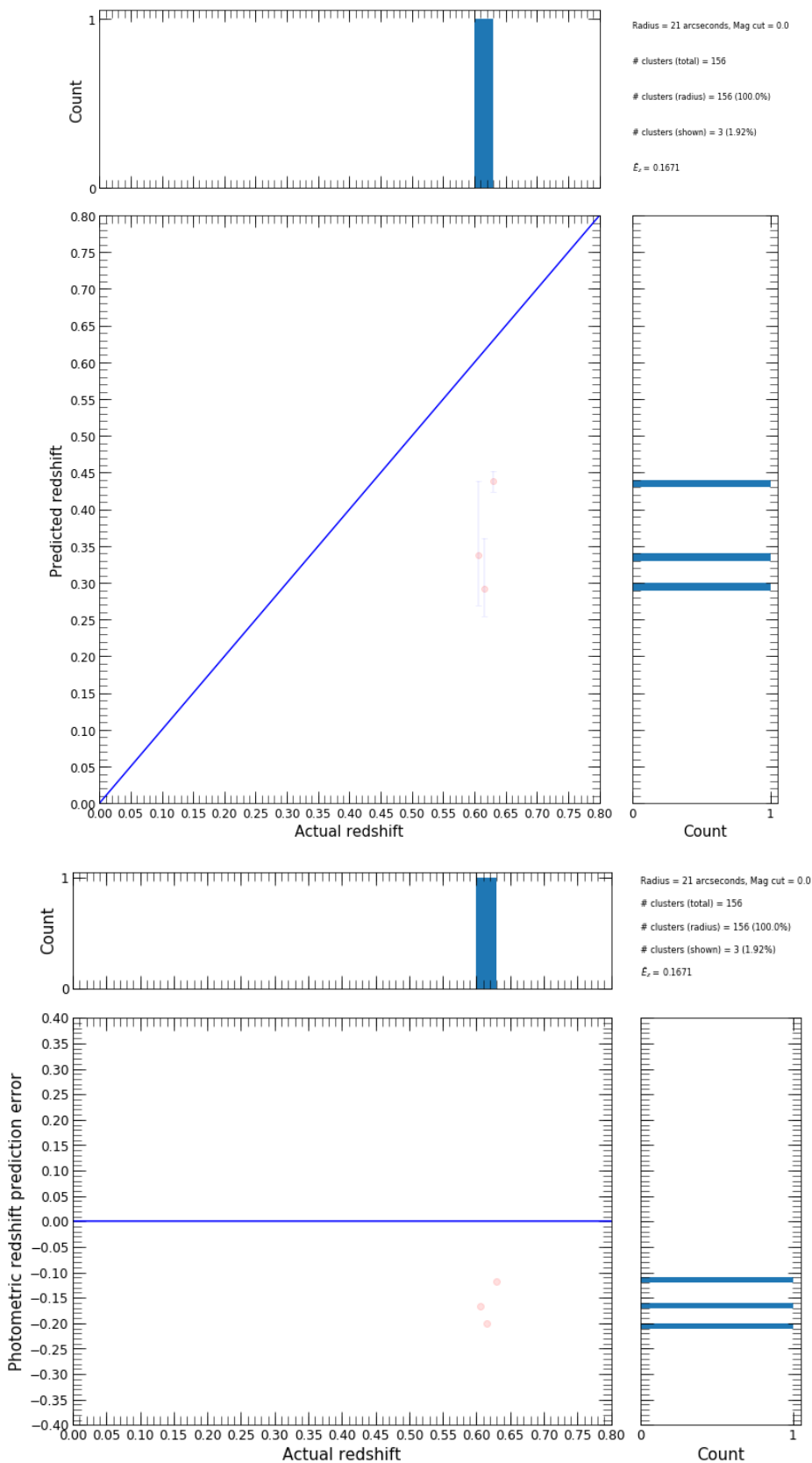
**Figure S17.** This figure displays the performance of photometric redshift predictions of clusters at high redshift, which did not qualify for the WNMR dataset, that had full bootstrap resamples returned within a 21 arcseconds search radius. Top row: Predicted versus 'actual' photometric redshift of tested clusters with frequency histograms of the distributions. Bottom row: Non-absolute photometric redshift prediction error versus 'actual' redshift of tested clusters with frequency histograms of the distributions. Other: '# clusters (total)' represents the total number of clusters at high redshift which did not qualify for the WNMR dataset, '# clusters (radius)' represents the number of clusters at high redshift which did not qualify for the WNMR dataset that have observed galaxies within a 21 arcseconds search radius, '# clusters (shown)' represents the number of clusters at high redshift which did not qualify for the WNMR dataset that have observed galaxies within a 21 arcseconds search radius with full bootstrap resamples returned,  $\bar{E}_z$  represents the median of photometric redshift prediction errors across all tested clusters within a 21 arcseconds search radius with full bootstrap resamples returned.



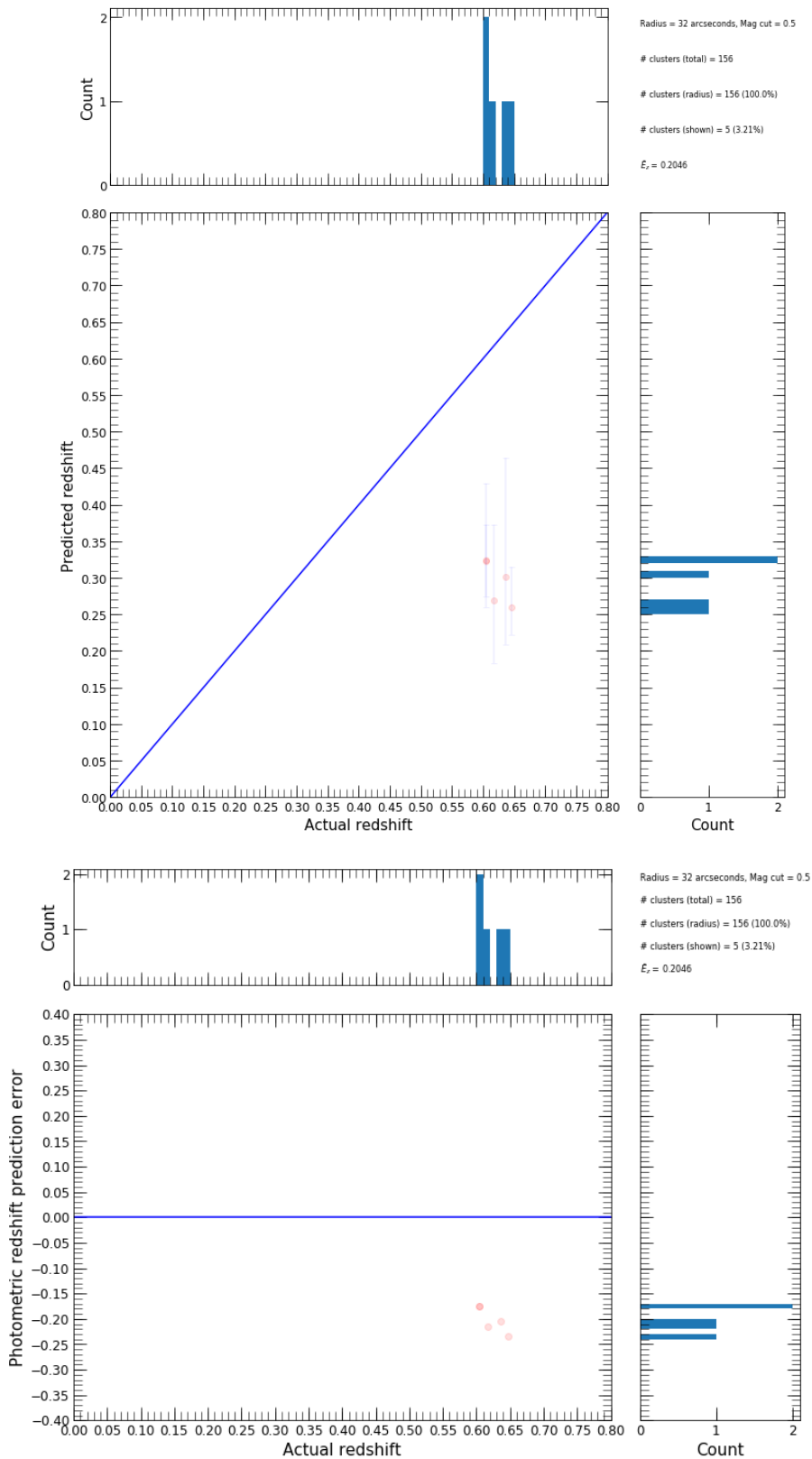
**Figure S18.** This figure displays the performance of photometric redshift predictions of clusters at high redshift, which did not qualify for the WNMR dataset, that had full bootstrap resamples returned within a 32 arcseconds search radius. Top row: Predicted versus 'actual' photometric redshift of tested clusters with frequency histograms of the distributions. Bottom row: Non-absolute photometric redshift prediction error versus 'actual' redshift of tested clusters with frequency histograms of the distributions. Other: '# clusters (total)' represents the total number of clusters at high redshift which did not qualify for the WNMR dataset, '# clusters (radius)' represents the number of clusters at high redshift which did not qualify for the WNMR dataset that have observed galaxies within a 32 arcseconds search radius, '# clusters (shown)' represents the number of clusters at high redshift which did not qualify for the WNMR dataset that have observed galaxies within a 32 arcseconds search radius with full bootstrap resamples returned,  $\bar{E}_z$  represents the median of photometric redshift prediction errors across all tested clusters within a 32 arcseconds search radius with full bootstrap resamples returned.



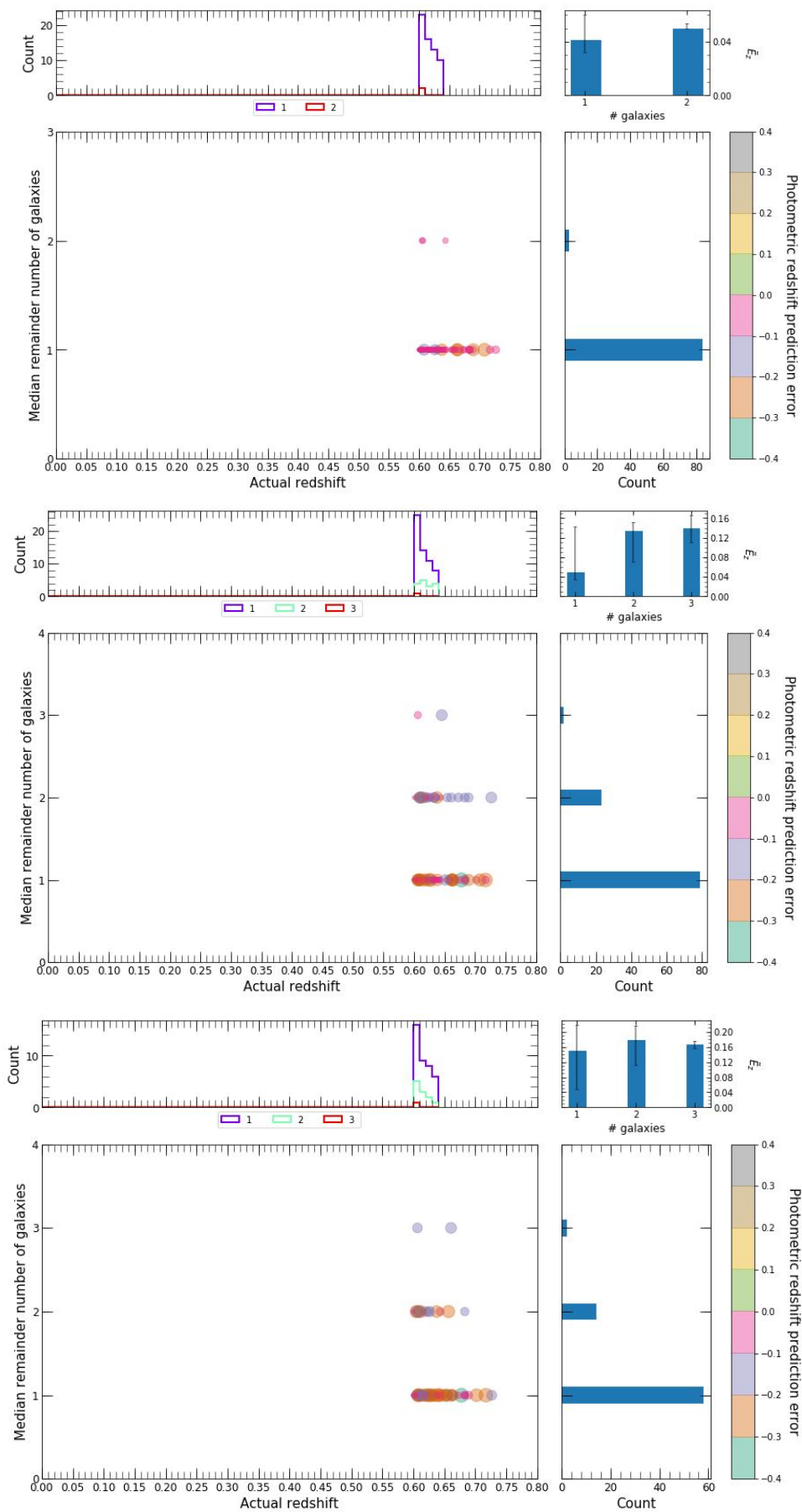
**Figure S19.** This figure displays the performance of photometric redshift predictions of clusters at high redshift, which did not qualify for the WNMR dataset, that had partial bootstrap resamples returned within a 10 arcseconds search radius. It should be noted that in this figure there were no resultant predictions made by the tuned model, as none of the clusters met the conditions. Top row: Predicted versus 'actual' photometric redshift of tested clusters with frequency histograms of the distributions. Bottom row: Non-absolute photometric redshift prediction error versus 'actual' redshift of tested clusters with frequency histograms of the distributions. Other: '# clusters (total)' represents the total number of clusters at high redshift which did not qualify for the WNMR dataset, '# clusters (radius)' represents the number of clusters at high redshift which did not qualify for the WNMR dataset that have observed galaxies within a 10 arcseconds search radius, '# clusters (shown)' represents the number of clusters at high redshift which did not qualify for the WNMR dataset that have observed galaxies within a 10 arcseconds search radius with partial bootstrap resamples returned,  $\bar{E}_z$  represents the median of photometric redshift prediction errors across all tested clusters within a 10 arcseconds search radius with partial bootstrap resamples returned.



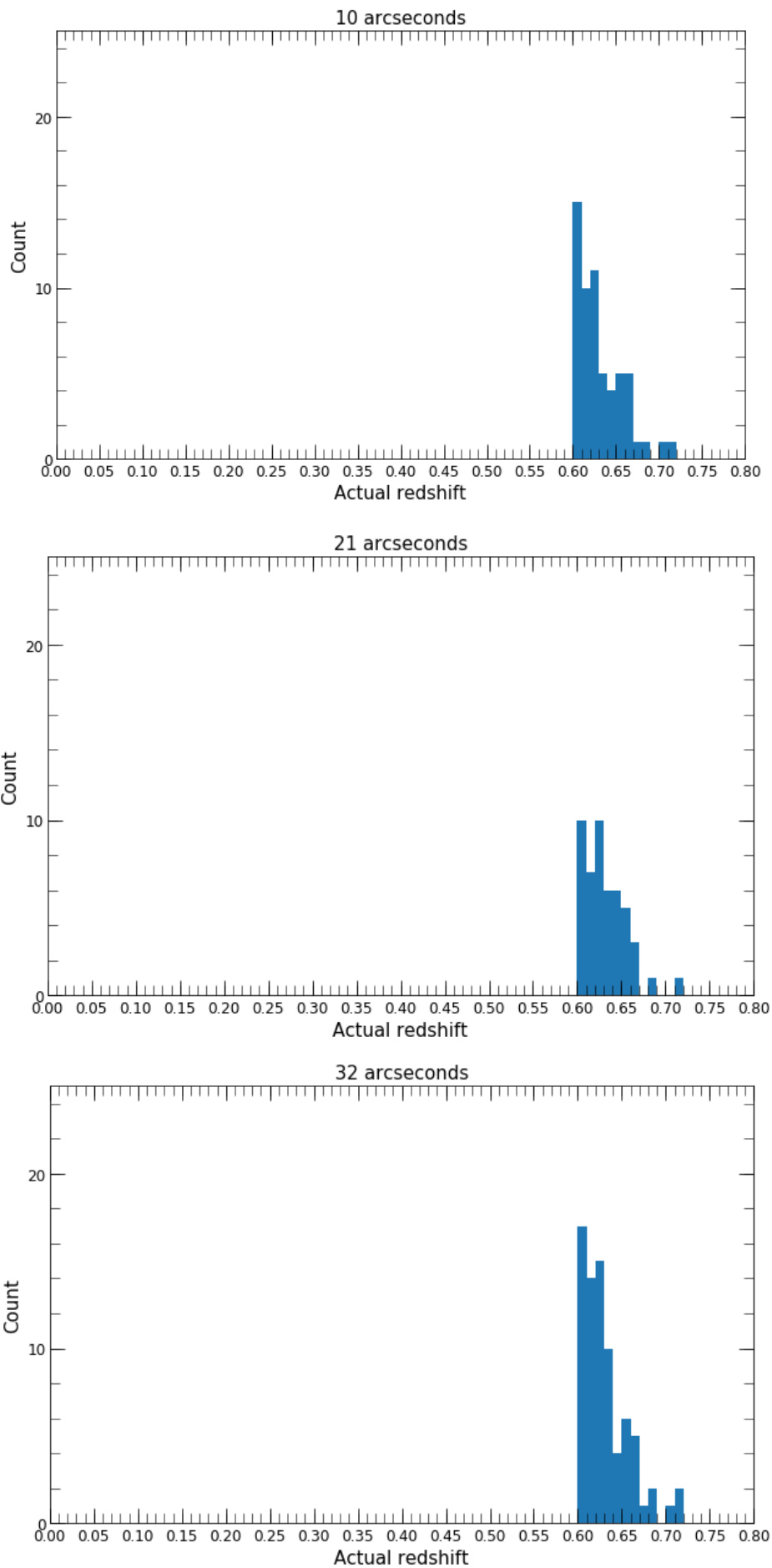
**Figure S20.** This figure displays the performance of photometric redshift predictions of clusters at high redshift, which did not qualify for the WNMR dataset, that had partial bootstrap resamples returned within a 21 arcseconds search radius. Top row: Predicted versus 'actual' photometric redshift of tested clusters with frequency histograms of the distributions. Bottom row: Non-absolute photometric redshift prediction error versus 'actual' redshift of tested clusters with frequency histograms of the distributions. Other: '# clusters (total)' represents the total number of clusters at high redshift which did not qualify for the WNMR dataset, '# clusters (radius)' represents the number of clusters at high redshift which did not qualify for the WNMR dataset that have observed galaxies within a 21 arcseconds search radius, '# clusters (shown)' represents the number of clusters at high redshift which did not qualify for the WNMR dataset that have observed galaxies within a 21 arcseconds search radius with partial bootstrap resamples returned,  $\bar{E}_z$  represents the median of photometric redshift prediction errors across all tested clusters within a 21 arcseconds search radius with partial bootstrap resamples returned.



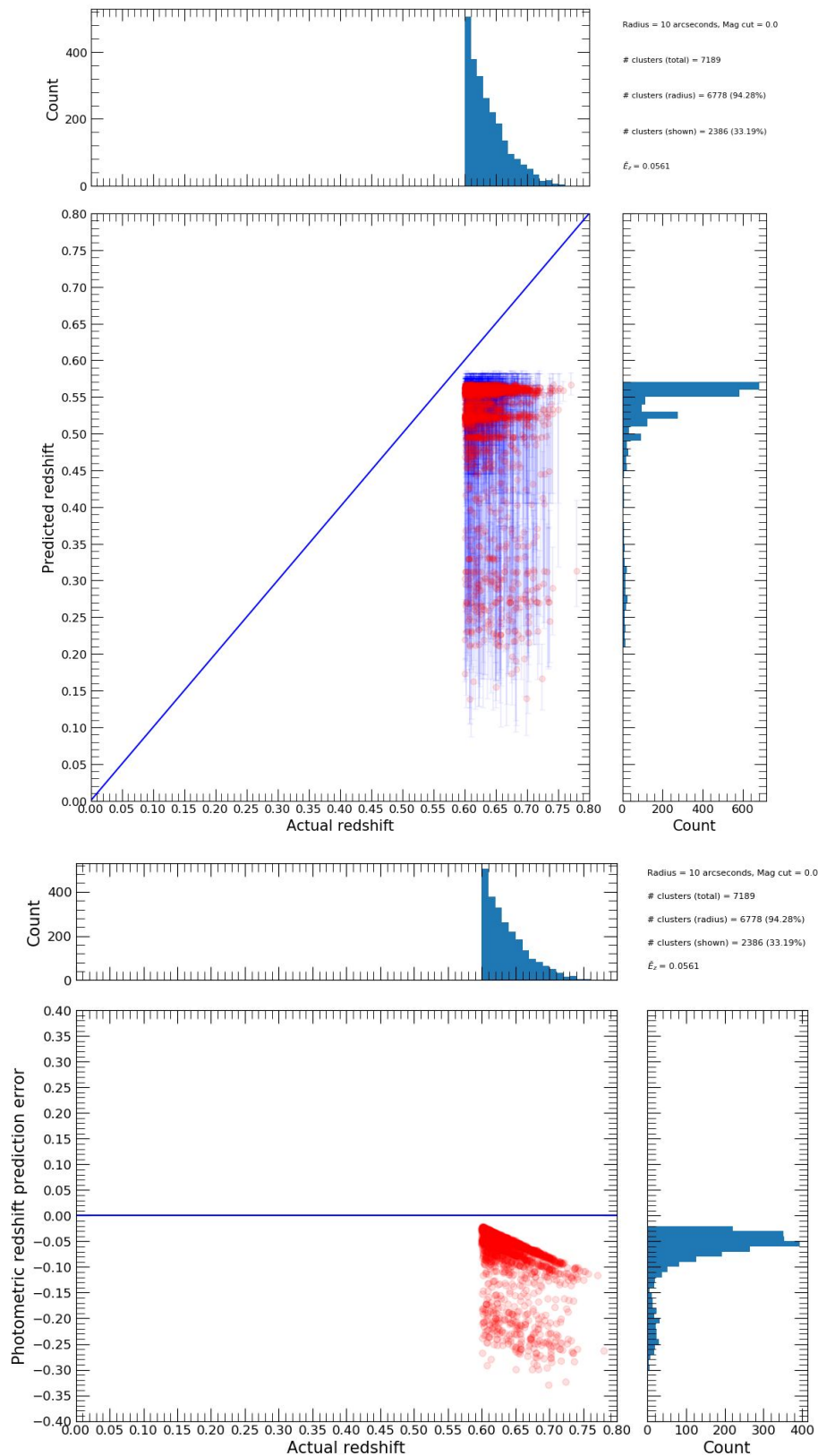
**Figure S21.** This figure displays the performance of photometric redshift predictions of clusters at high redshift, which did not qualify for the WNMR dataset, that had partial bootstrap resamples returned within a 32 arcseconds search radius. Top row: Predicted versus 'actual' photometric redshift of tested clusters with frequency histograms of the distributions. Bottom row: Non-absolute photometric redshift prediction error versus 'actual' redshift of tested clusters with frequency histograms of the distributions. Other: '# clusters (total)' represents the total number of clusters at high redshift which did not qualify for the WNMR dataset, '# clusters (radius)' represents the number of clusters at high redshift which did not qualify for the WNMR dataset that have observed galaxies within a 32 arcseconds search radius, '# clusters (shown)' represents the number of clusters at high redshift which did not qualify for the WNMR dataset that have observed galaxies within a 32 arcseconds search radius with partial bootstrap resamples returned,  $\bar{E}_z$  represents the median of photometric redshift prediction errors across all tested clusters within a 32 arcseconds search radius with partial bootstrap resamples returned.



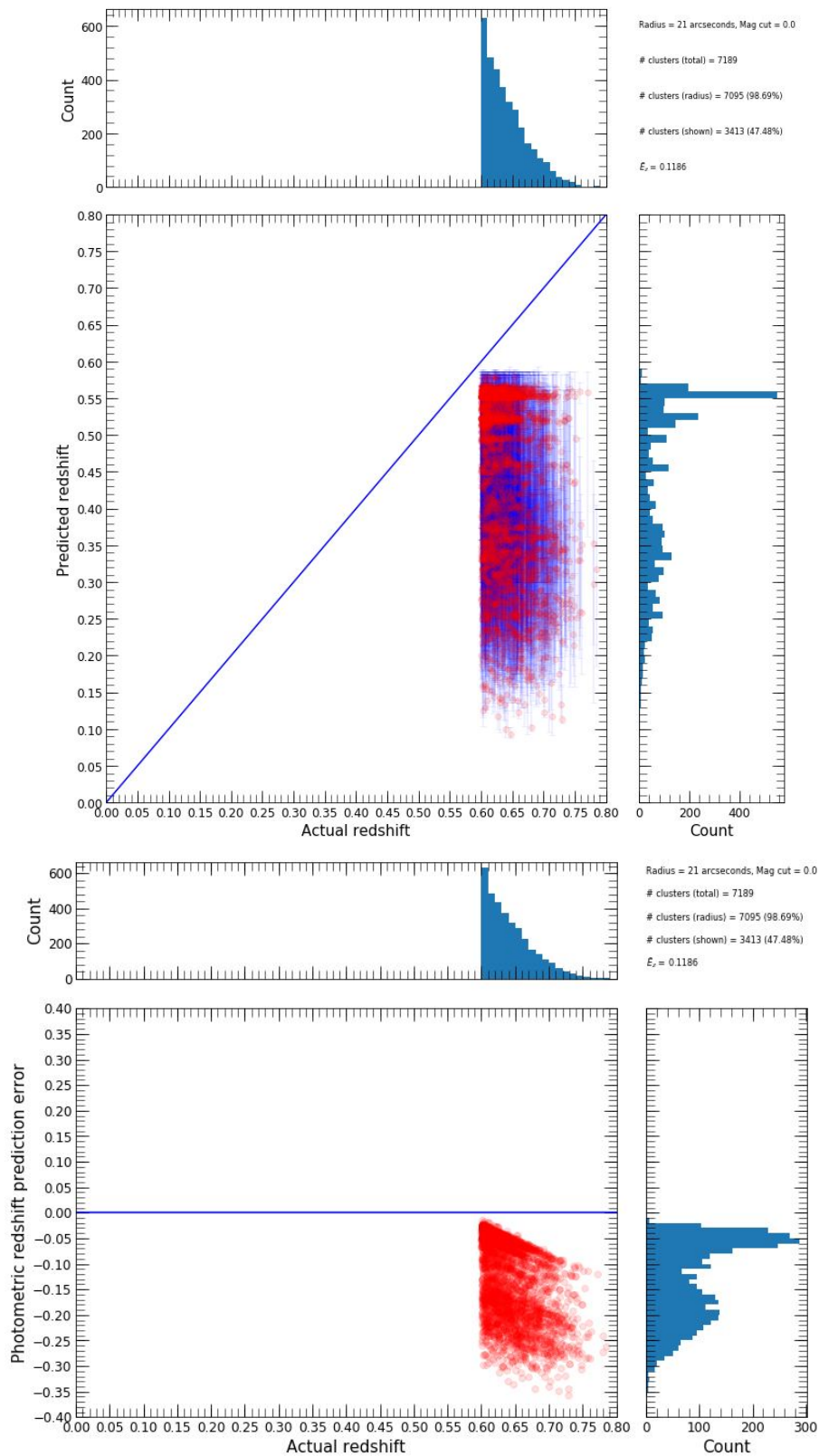
**Figure S22.** This figure displays the number of galaxies used in photometric redshift predictions of clusters at high redshift versus 'actual' redshift of tested clusters, which did not qualify for the WNMR dataset, where predictions had full bootstrap resamples returned within a 10 (top row), 21 (middle row) and 32 (bottom row) arcseconds search radius. It should be noted that the size of individual points change in relation to the value of the non-absolute photometric redshift prediction error. Frequency histograms of the distributions are also shown.  $\bar{E}_z$  represents the median of photometric redshift prediction errors across all tested clusters for each number of galaxies bin.



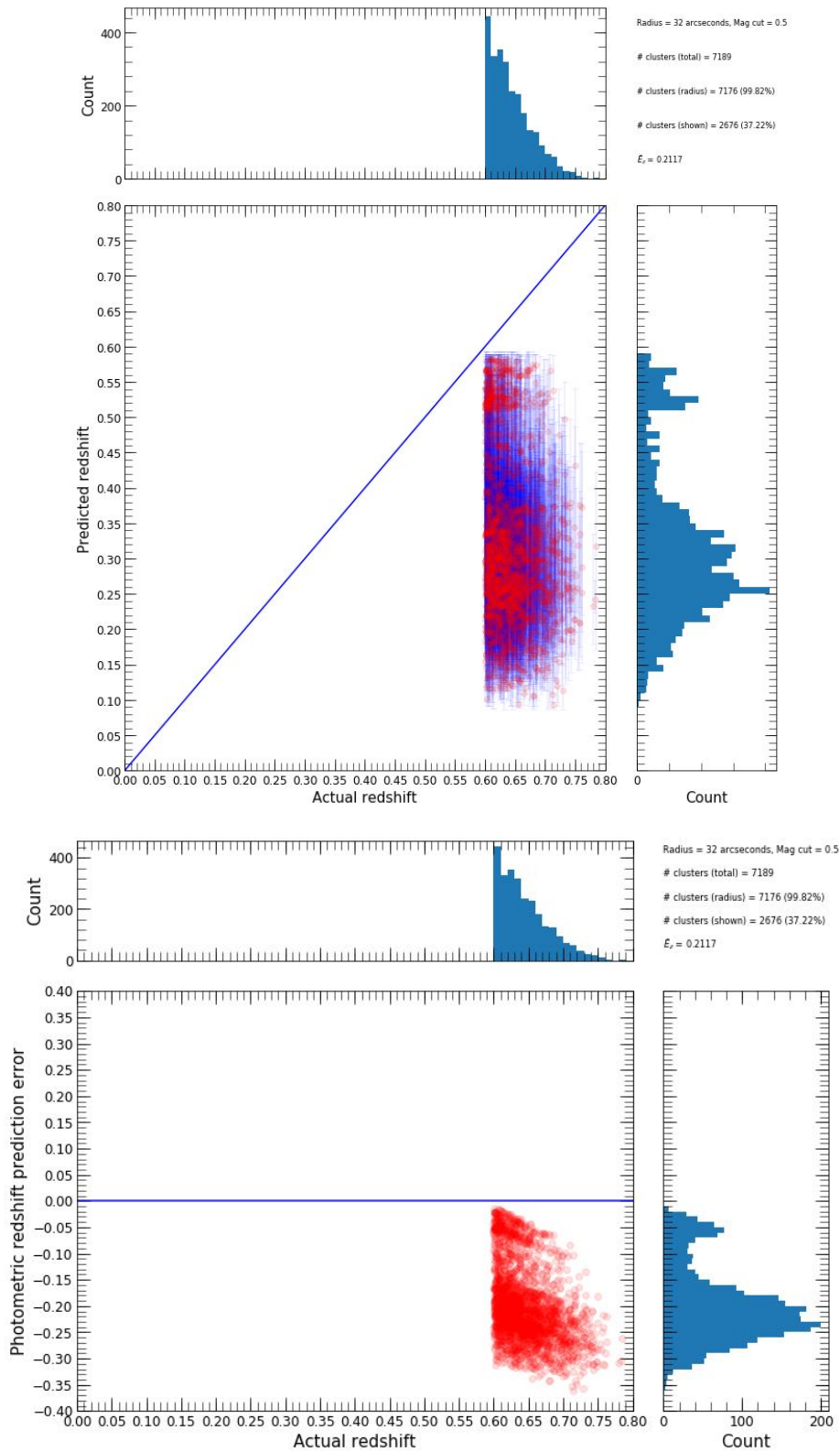
**Figure S23.** This figure displays the 'actual' redshift distributions of clusters at high redshift, which did not qualify for the WNMR dataset, that had no bootstrap resamples returned within a 10 (top row), 21 (middle row) and 32 (bottom row) arcseconds search radius.



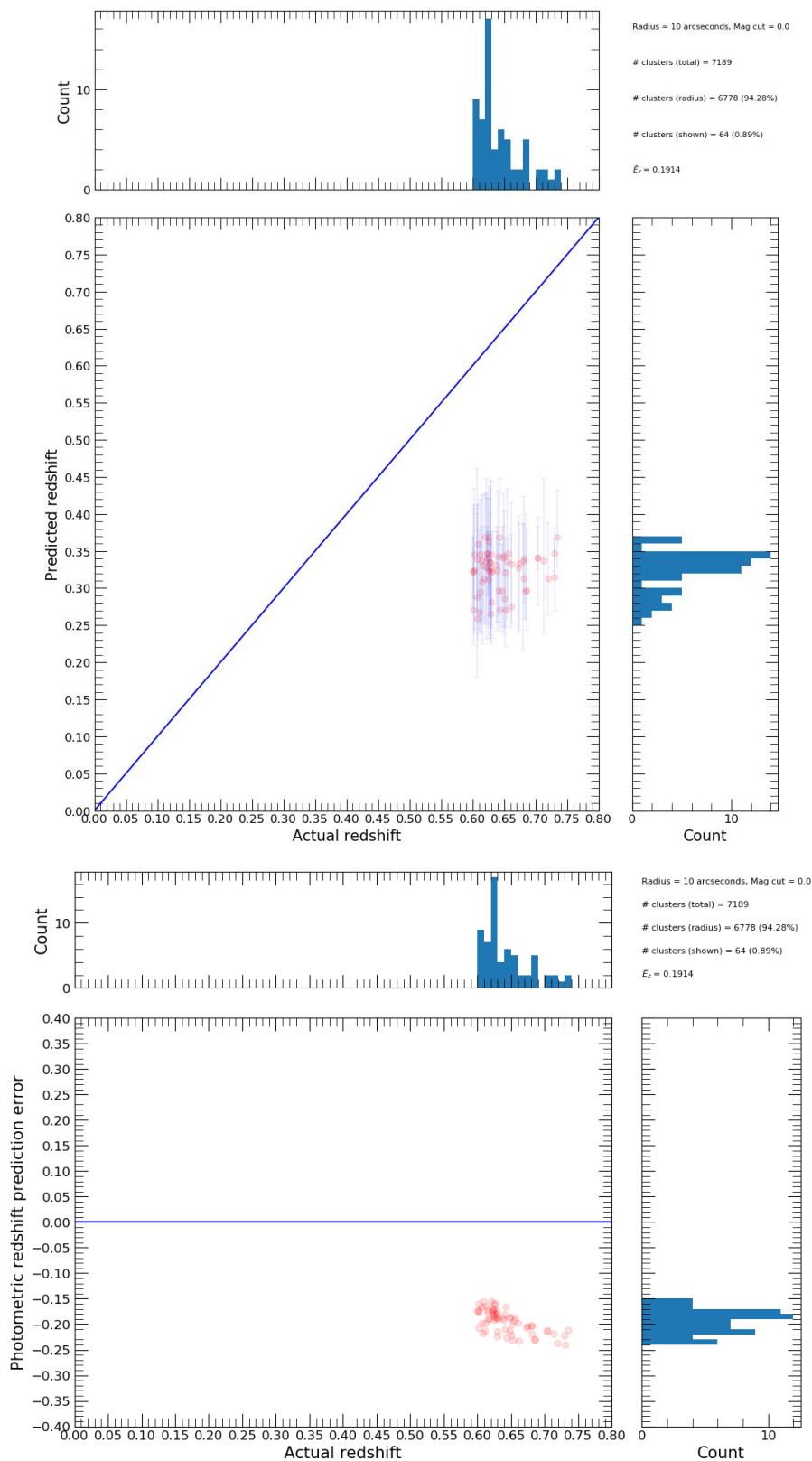
**Figure S24.** This figure displays the performance of photometric redshift predictions of clusters at high redshift with low richness, which did not qualify for the WNMN dataset, that had full bootstrap resamples returned within a 10 arcseconds search radius. Top row: Predicted versus 'actual' photometric redshift of tested clusters with frequency histograms of the distributions. Bottom row: Non-absolute photometric redshift prediction error versus 'actual' redshift of tested clusters with frequency histograms of the distributions. Other: '# clusters (total)' represents the total number of clusters at high redshift with low richness which did not qualify for the WNMN dataset, '# clusters (radius)' represents the number of clusters at high redshift with low richness which did not qualify for the WNMN dataset that have observed galaxies within a 10 arcseconds search radius, '# clusters (shown)' represents the number of clusters at high redshift with low richness which did not qualify for the WNMN dataset that have observed galaxies within a 10 arcseconds search radius with full bootstrap resamples returned,  $\bar{E}_z$  represents the median of photometric redshift prediction errors across all tested clusters within a 10 arcseconds search radius with full bootstrap resamples returned.



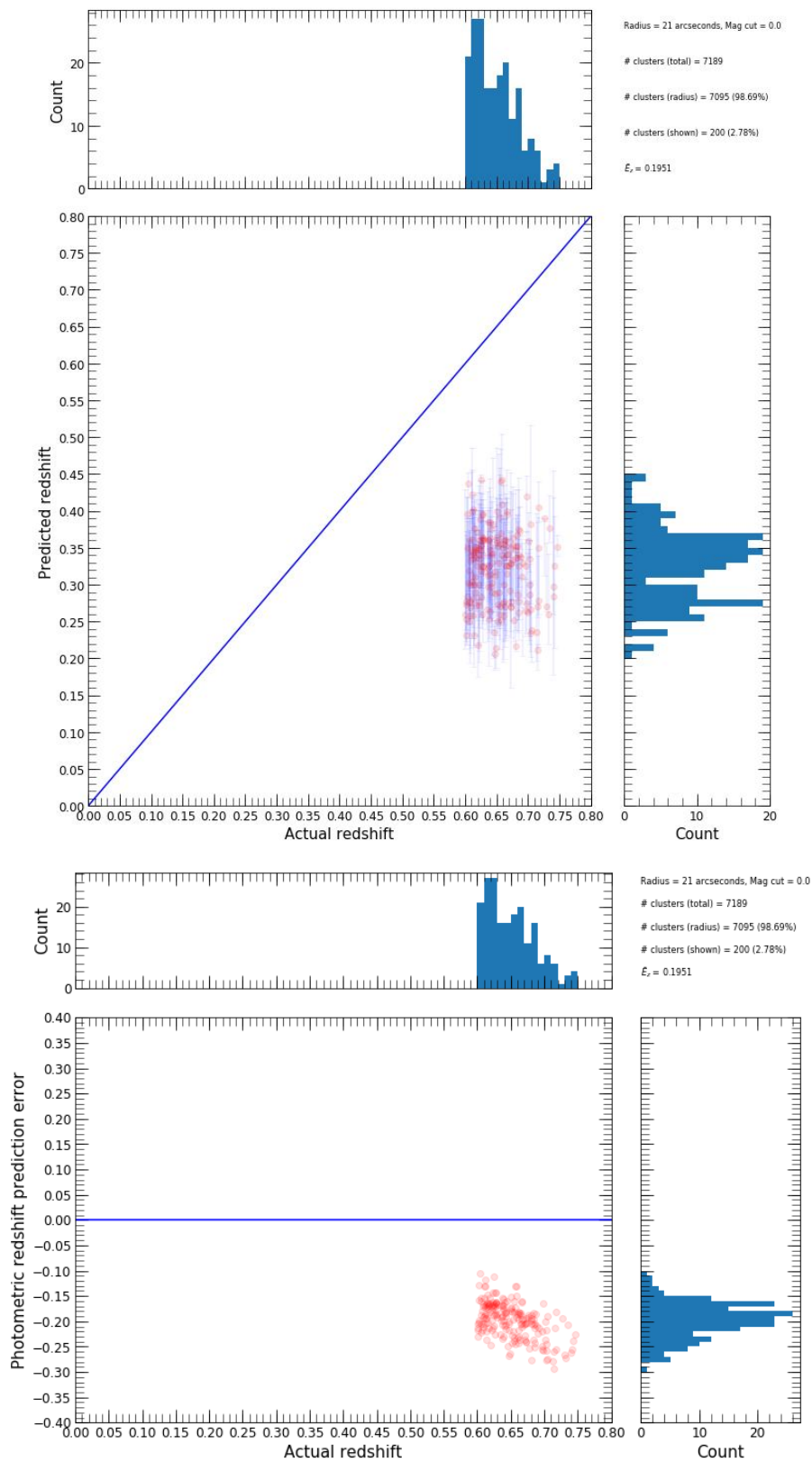
**Figure S25.** This figure displays the performance of photometric redshift predictions of clusters at high redshift with low richness, which did not qualify for the WNMR dataset, that had full bootstrap resamples returned within a 21 arcseconds search radius. Top row: Predicted versus 'actual' photometric redshift of tested clusters with frequency histograms of the distributions. Bottom row: Non-absolute photometric redshift prediction error versus 'actual' redshift of tested clusters with frequency histograms of the distributions. Other: '# clusters (total)' represents the total number of clusters at high redshift with low richness which did not qualify for the WNMR dataset, '# clusters (radius)' represents the number of clusters at high redshift with low richness which did not qualify for the WNMR dataset that have observed galaxies within a 21 arcseconds search radius, '# clusters (shown)' represents the number of clusters at high redshift with low richness which did not qualify for the WNMR dataset that have observed galaxies within a 21 arcseconds search radius with full bootstrap resamples returned,  $\bar{\epsilon}_z$  represents the median of photometric redshift prediction errors across all tested clusters within a 21 arcseconds search radius with full bootstrap resamples returned.



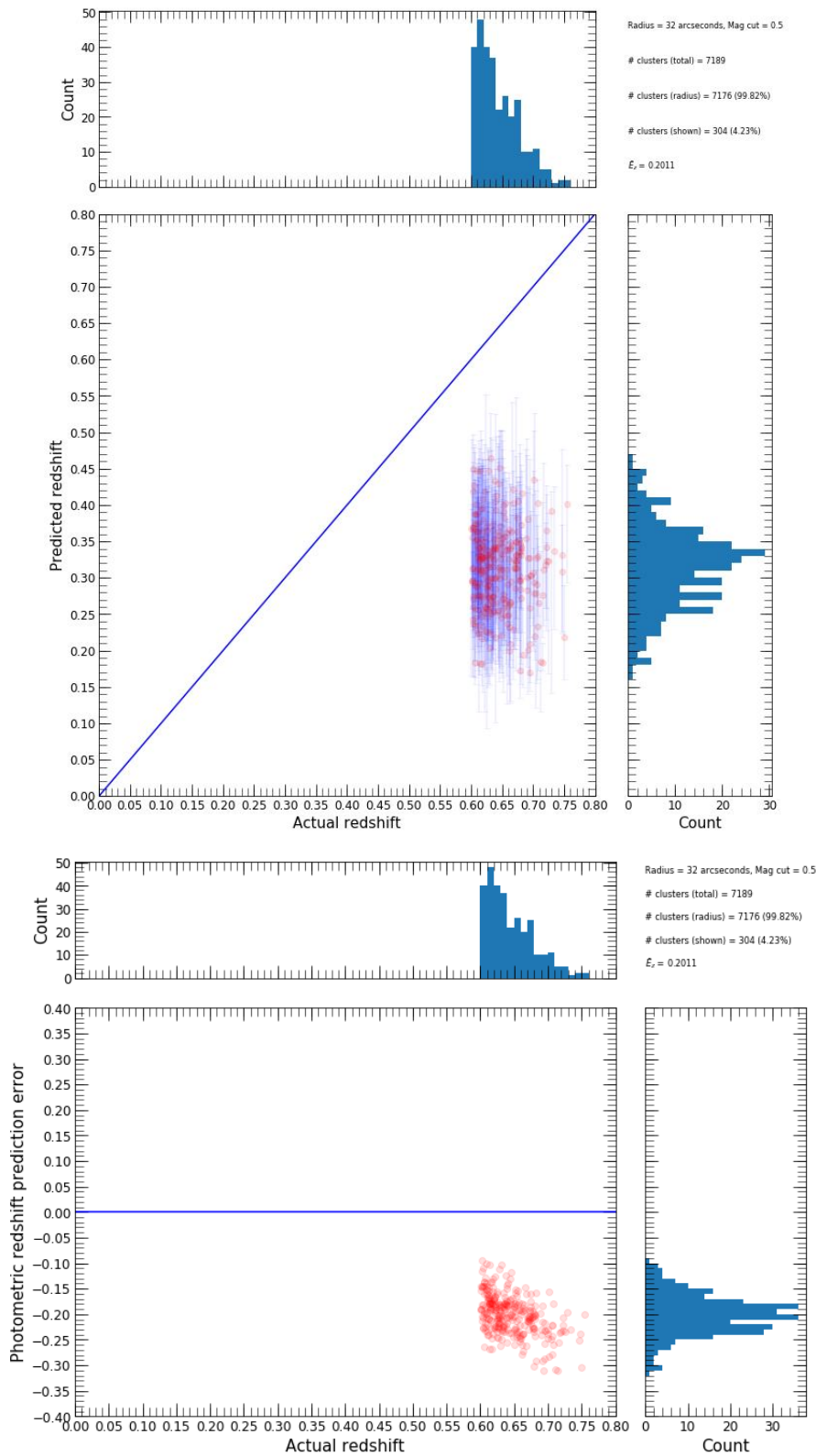
**Figure S26.** This figure displays the performance of photometric redshift predictions of clusters at high redshift with low richness, which did not qualify for the WNMR dataset, that had full bootstrap resamples returned within a 32 arcseconds search radius. Top row: Predicted versus 'actual' photometric redshift of tested clusters with frequency histograms of the distributions. Bottom row: Non-absolute photometric redshift prediction error versus 'actual' redshift of tested clusters with frequency histograms of the distributions. Other: '# clusters (total)' represents the total number of clusters at high redshift with low richness which did not qualify for the WNMR dataset, '# clusters (radius)' represents the number of clusters at high redshift with low richness which did not qualify for the WNMR dataset that have observed galaxies within a 32 arcseconds search radius, '# clusters (shown)' represents the number of clusters at high redshift with low richness which did not qualify for the WNMR dataset that have observed galaxies within a 32 arcseconds search radius with full bootstrap resamples returned,  $\bar{E}_z$  represents the median of photometric redshift prediction errors across all tested clusters within a 32 arcseconds search radius with full bootstrap resamples returned.



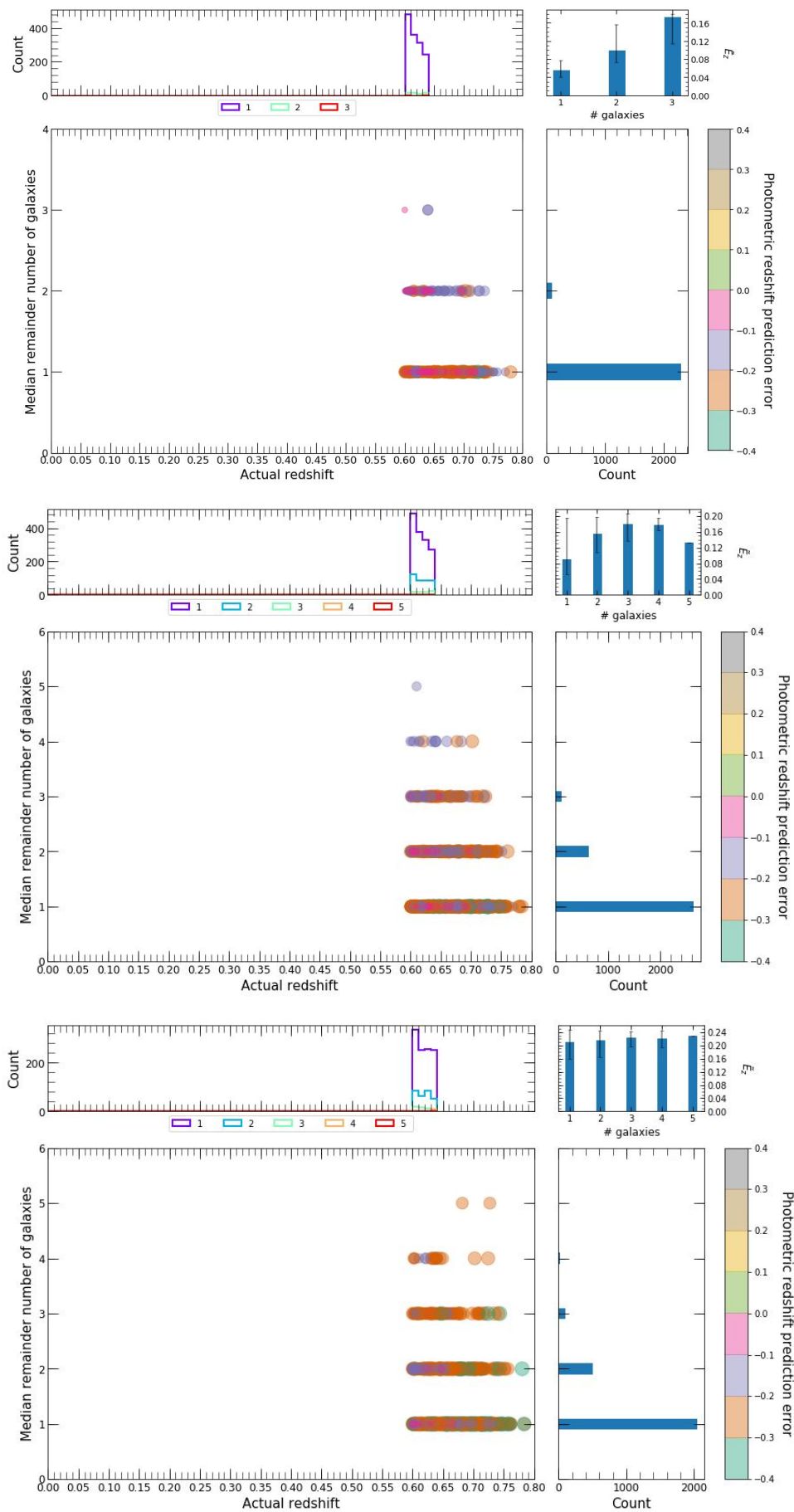
**Figure S27.** This figure displays the performance of photometric redshift predictions of clusters at high redshift with low richness, which did not qualify for the WNMN dataset, that had partial bootstrap resamples returned within a 10 arcseconds search radius. Top row: Predicted versus 'actual' photometric redshift of tested clusters with frequency histograms of the distributions. Bottom row: Non-absolute photometric redshift prediction error versus 'actual' redshift of tested clusters with frequency histograms of the distributions. Other: '# clusters (total)' represents the total number of clusters at high redshift with low richness which did not qualify for the WNMN dataset, '# clusters (radius)' represents the number of clusters at high redshift with low richness which did not qualify for the WNMN dataset that have observed galaxies within a 10 arcseconds search radius, '# clusters (shown)' represents the number of clusters at high redshift with low richness which did not qualify for the WNMN dataset that have observed galaxies within a 10 arcseconds search radius with partial bootstrap resamples returned,  $\tilde{E}_z$  represents the median of photometric redshift prediction errors across all tested clusters within a 10 arcseconds search radius with partial bootstrap resamples returned.



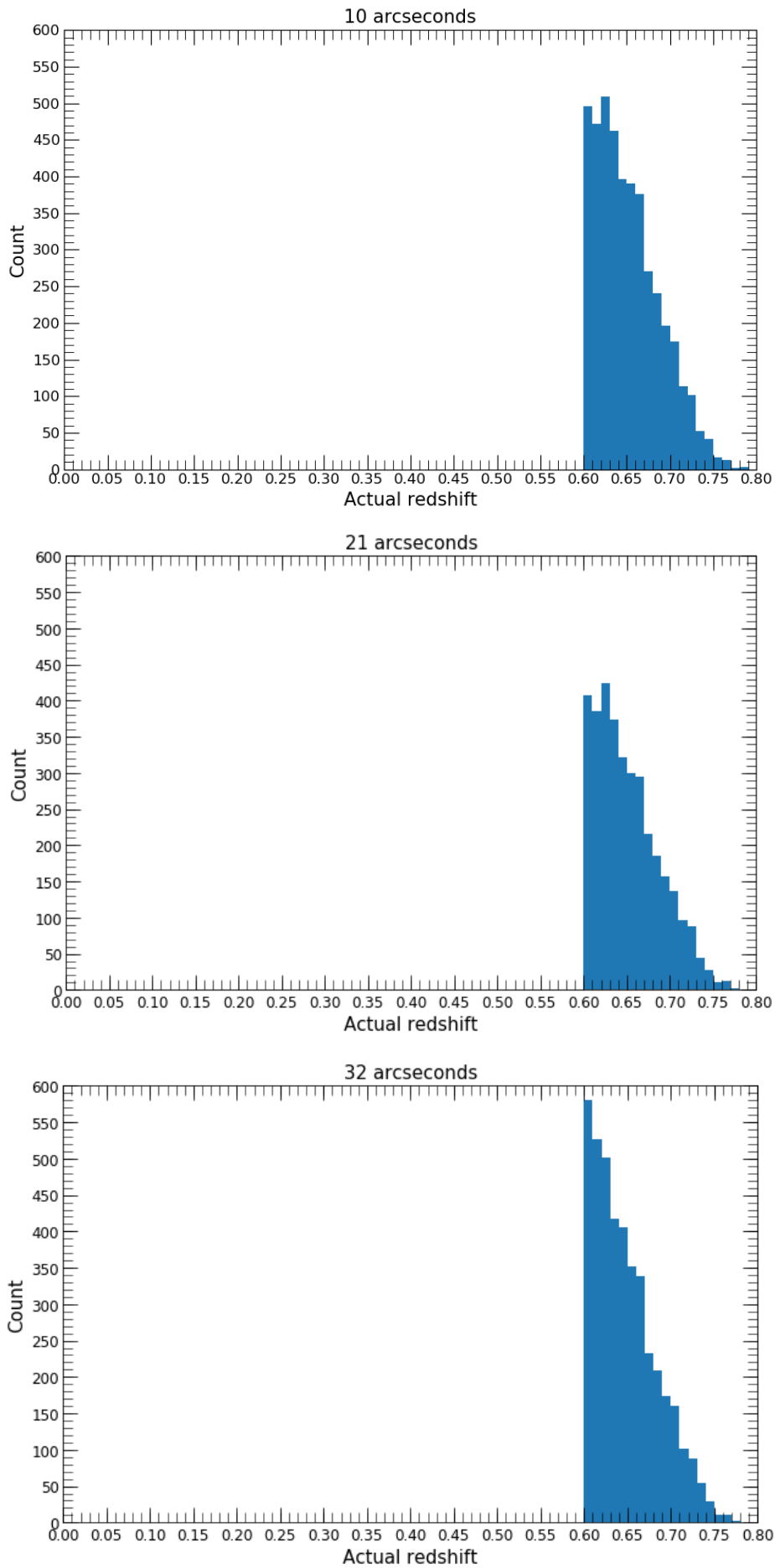
**Figure S28.** This figure displays the performance of photometric redshift predictions of clusters at high redshift with low richness, which did not qualify for the WNMR dataset, that had partial bootstrap resamples returned within a 21 arcseconds search radius. Top row: Predicted versus 'actual' photometric redshift of tested clusters with frequency histograms of the distributions. Bottom row: Non-absolute photometric redshift prediction error versus 'actual' redshift of tested clusters with frequency histograms of the distributions. Other: '# clusters (total)' represents the total number of clusters at high redshift with low richness which did not qualify for the WNMR dataset, '# clusters (radius)' represents the number of clusters at high redshift with low richness which did not qualify for the WNMR dataset that have observed galaxies within a 21 arcseconds search radius, '# clusters (shown)' represents the number of clusters at high redshift with low richness which did not qualify for the WNMR dataset that have observed galaxies within a 21 arcseconds search radius with partial bootstrap resamples returned,  $\bar{\epsilon}_z$  represents the median of photometric redshift prediction errors across all tested clusters within a 21 arcseconds search radius with partial bootstrap resamples returned.



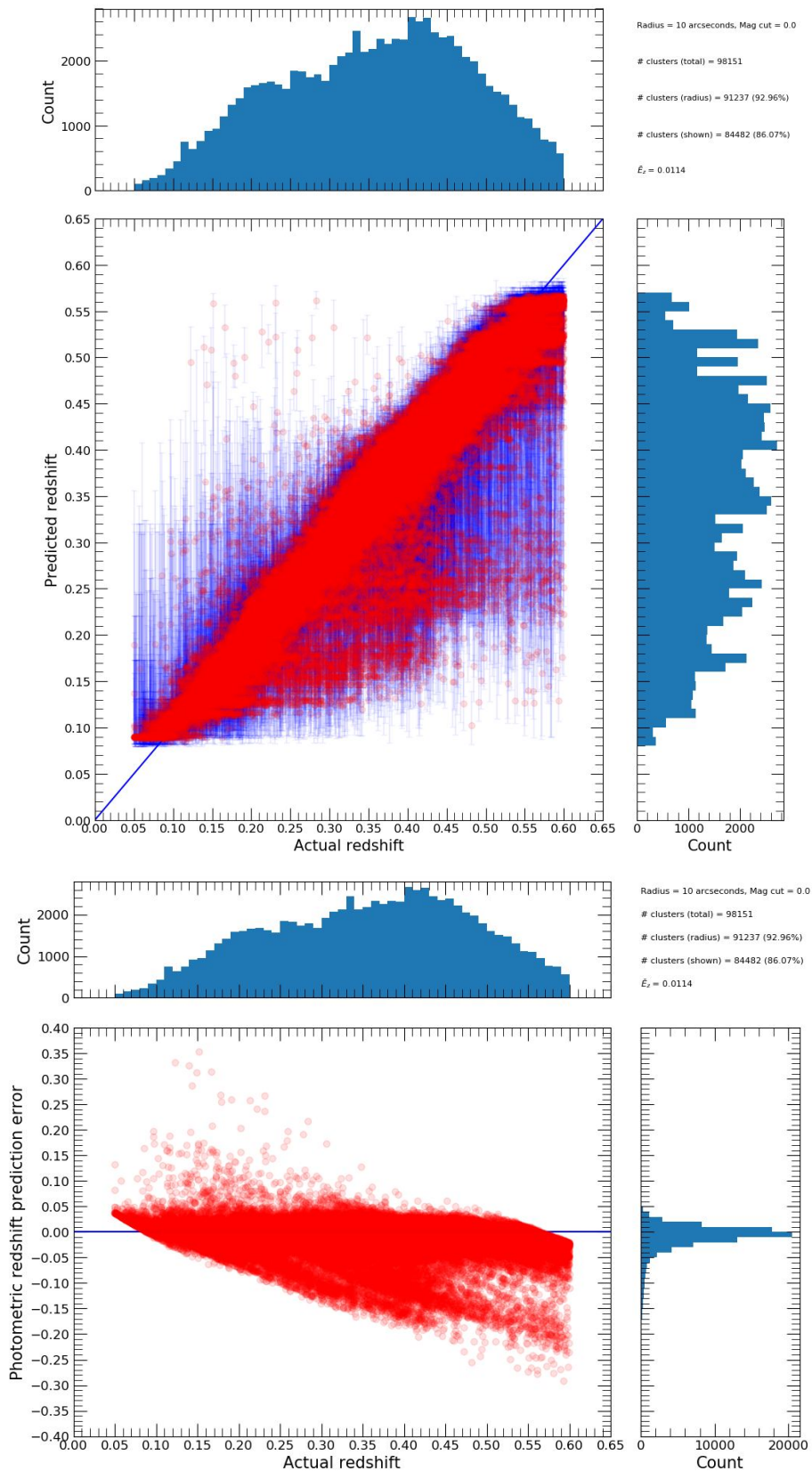
**Figure S29.** This figure displays the performance of photometric redshift predictions of clusters at high redshift with low richness, which did not qualify for the WNMR dataset, that had partial bootstrap resamples returned within a 32 arcseconds search radius. Top row: Predicted versus 'actual' photometric redshift of tested clusters with frequency histograms of the distributions. Bottom row: Non-absolute photometric redshift prediction error versus 'actual' redshift of tested clusters with frequency histograms of the distributions. Other: '# clusters (total)' represents the total number of clusters at high redshift with low richness which did not qualify for the WNMR dataset, '# clusters (radius)' represents the number of clusters at high redshift with low richness which did not qualify for the WNMR dataset that have observed galaxies within a 32 arcseconds search radius, '# clusters (shown)' represents the number of clusters at high redshift with low richness which did not qualify for the WNMR dataset that have observed galaxies within a 32 arcseconds search radius with partial bootstrap resamples returned,  $\bar{E}_z$  represents the median of photometric redshift prediction errors across all tested clusters within a 32 arcseconds search radius with partial bootstrap resamples returned.



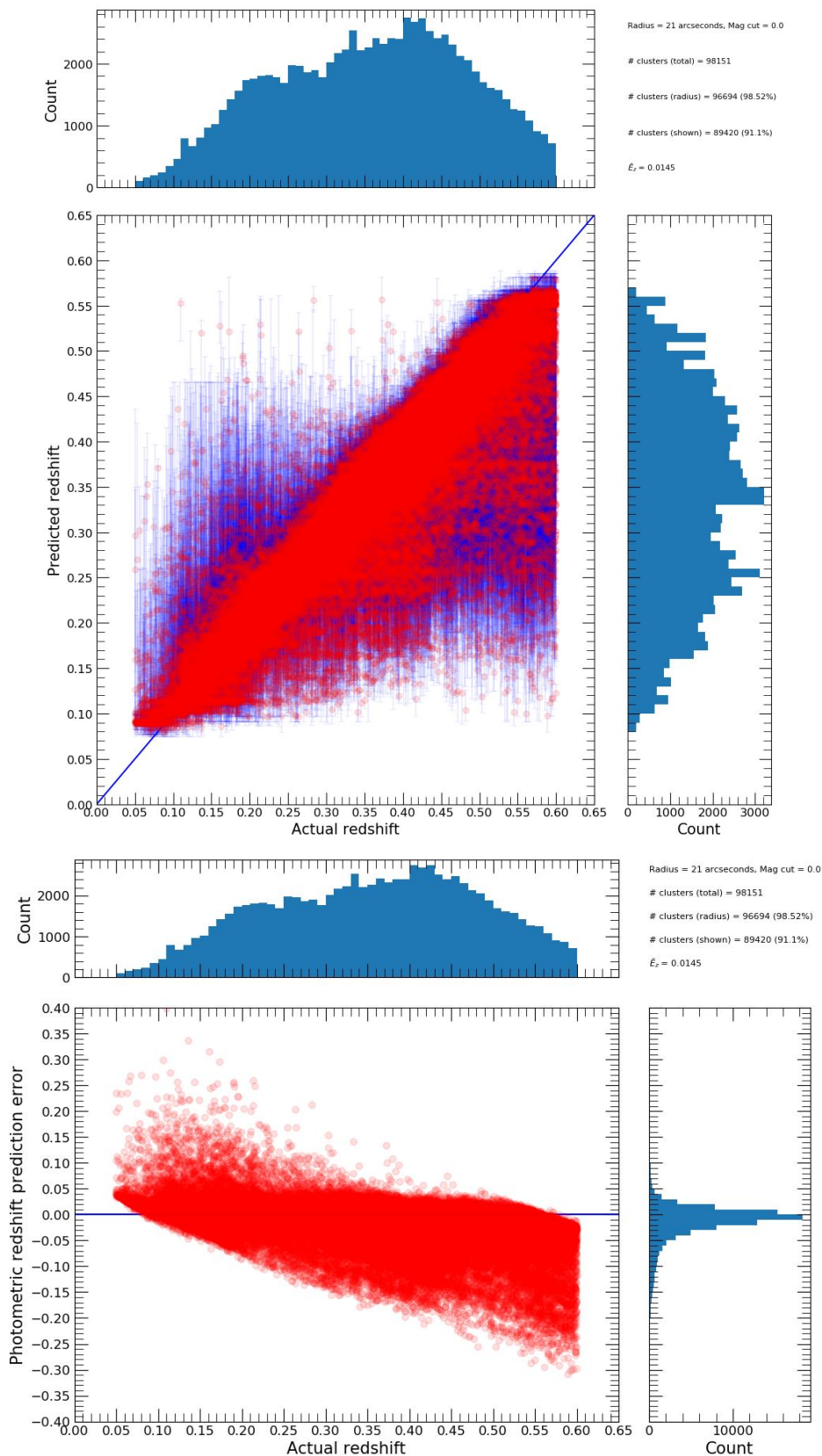
**Figure S30.** This figure displays the number of galaxies used in photometric redshift predictions of clusters at high redshift with low richness versus ‘actual’ redshift of tested clusters, which did not qualify for the WNMR dataset, where predictions had full bootstrap resamples returned within a 10 (top row), 21 (middle row) and 32 (bottom row) arcseconds search radius. It should be noted that the size of individual points change in relation to the value of the non-absolute photometric redshift prediction error. Frequency histograms of the distributions are also shown.  $\bar{E}_z$  represents the median of photometric redshift prediction errors across all tested clusters for each number of galaxies bin.



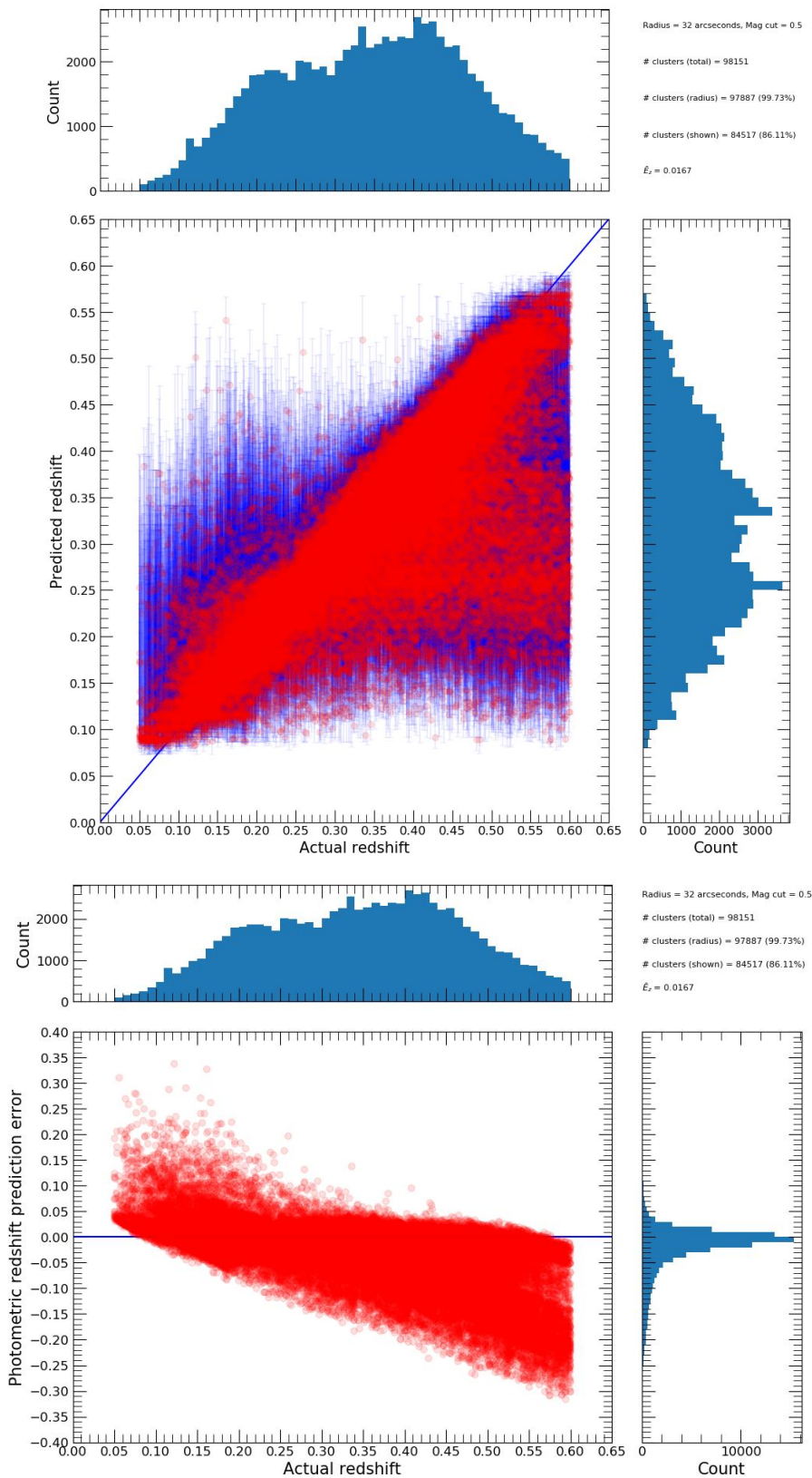
**Figure S31.** This figure displays the ‘actual’ redshift distributions of clusters at high redshift with low richness, which did not qualify for the WNMR dataset, that had no bootstrap resamples returned within a 10 (top row), 21 (middle row) and 32 (bottom row) arcseconds search radius.



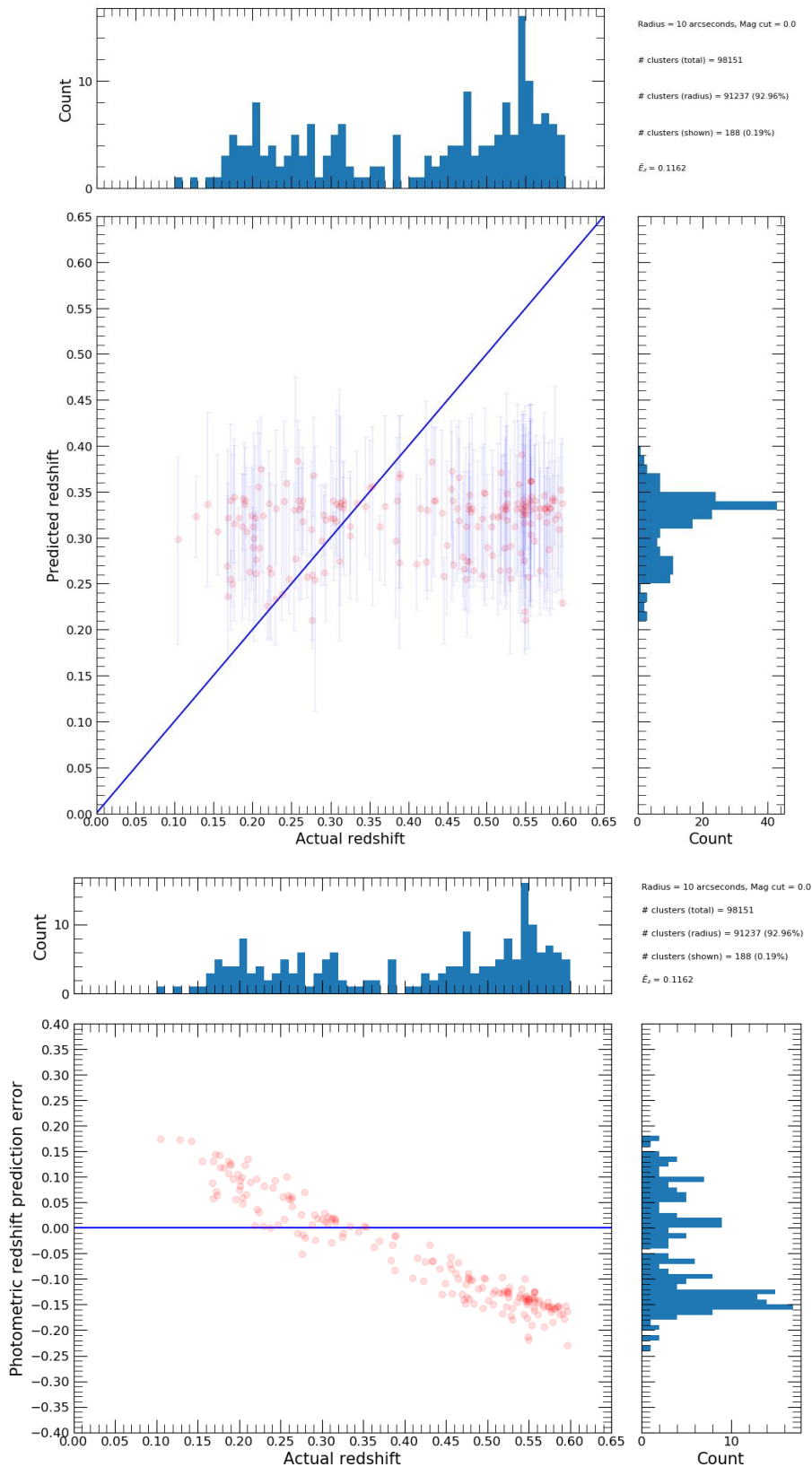
**Figure S32.** This figure displays the performance of photometric redshift predictions of clusters with low richness, which did not qualify for the WNMR dataset, that had full bootstrap resamples returned within a 10 arcseconds search radius. Top row: Predicted versus 'actual' photometric redshift of tested clusters with frequency histograms of the distributions. Bottom row: Non-absolute photometric redshift prediction error versus 'actual' redshift of tested clusters with frequency histograms of the distributions. Other: '# clusters (total)' represents the total number of clusters with low richness which did not qualify for the WNMR dataset, '# clusters (radius)' represents the number of clusters with low richness which did not qualify for the WNMR dataset that have observed galaxies within a 10 arcseconds search radius, '# clusters (shown)' represents the number of clusters with low richness which did not qualify for the WNMR dataset that have observed galaxies within a 10 arcseconds search radius with full bootstrap resamples returned,  $\bar{E}_z$  represents the median of photometric redshift prediction errors across all tested clusters within a 10 arcseconds search radius with full bootstrap resamples returned.



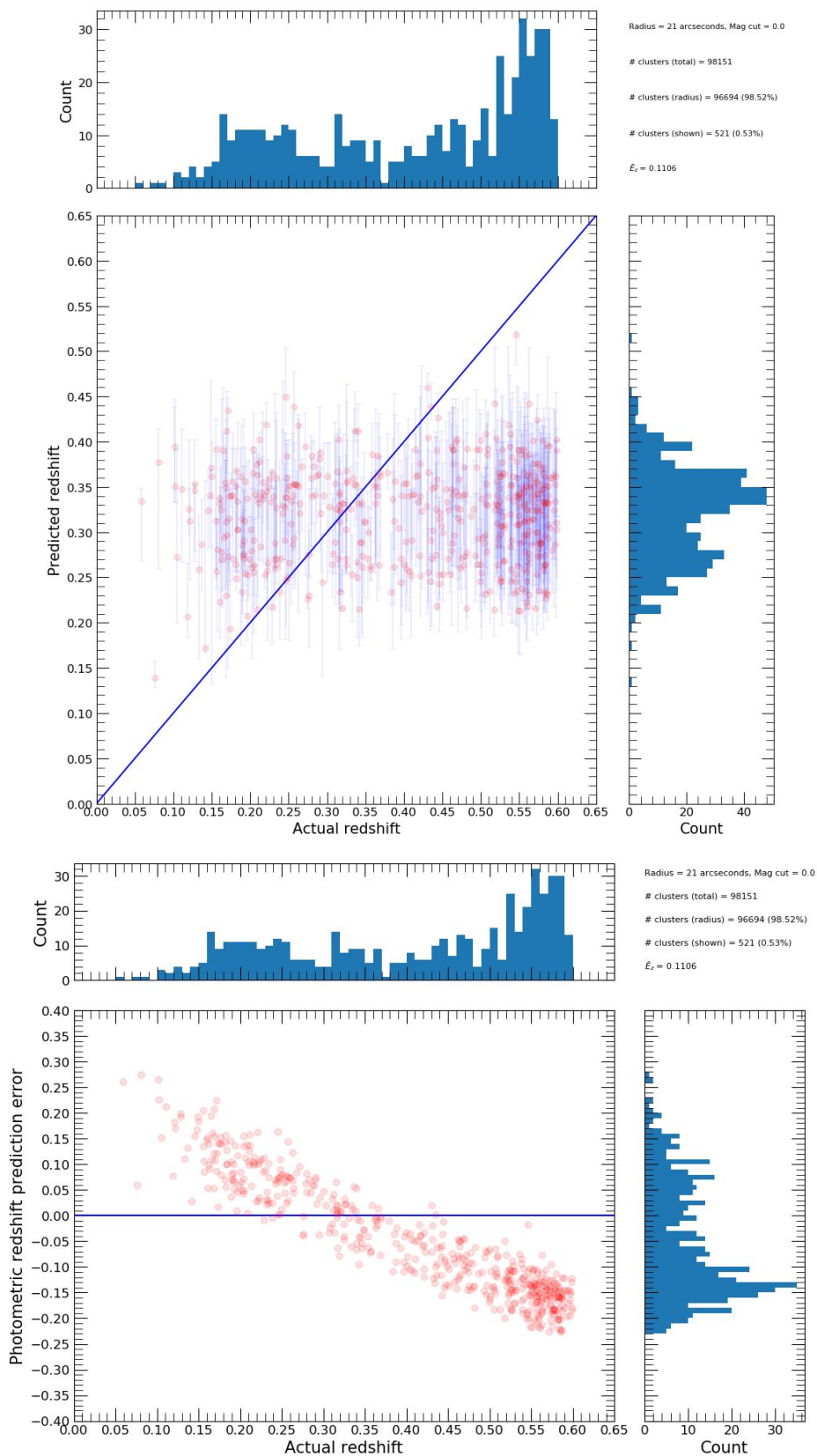
**Figure S33.** This figure displays the performance of photometric redshift predictions of clusters with low richness, which did not qualify for the WNMR dataset, that had full bootstrap resamples returned within a 21 arcseconds search radius. Top row: Predicted versus 'actual' photometric redshift of tested clusters with frequency histograms of the distributions. Bottom row: Non-absolute photometric redshift prediction error versus 'actual' redshift of tested clusters with frequency histograms of the distributions. Other: '# clusters (total)' represents the total number of clusters with low richness which did not qualify for the WNMR dataset, '# clusters (radius)' represents the number of clusters with low richness which did not qualify for the WNMR dataset that have observed galaxies within a 21 arcseconds search radius, '# clusters (shown)' represents the number of clusters with low richness which did not qualify for the WNMR dataset that have observed galaxies within a 21 arcseconds search radius with full bootstrap resamples returned,  $\bar{E}_z$  represents the median of photometric redshift prediction errors across all tested clusters within a 21 arcseconds search radius with full bootstrap resamples returned.



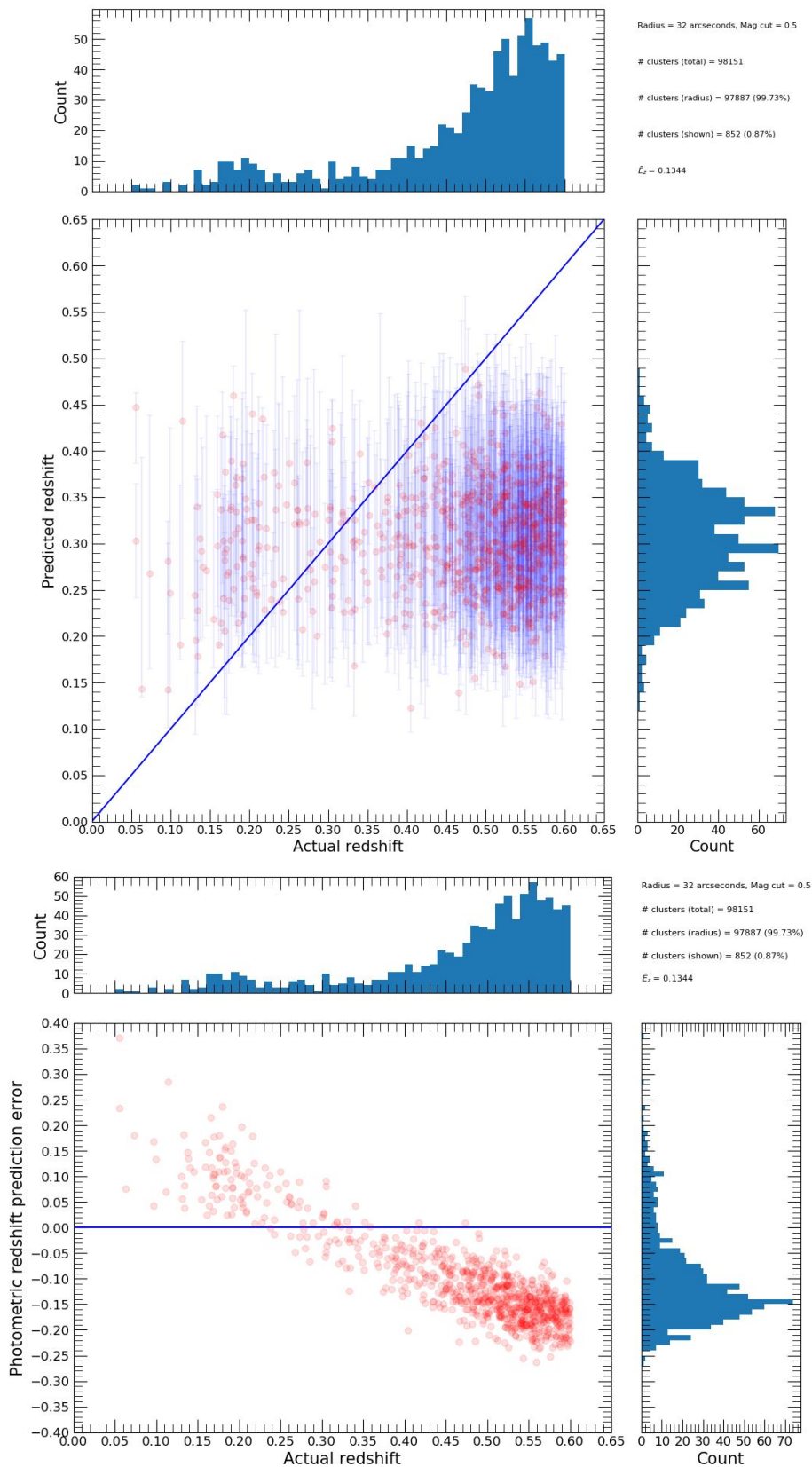
**Figure S34.** This figure displays the performance of photometric redshift predictions of clusters with low richness, which did not qualify for the WNMR dataset, that had full bootstrap resamples returned within a 32 arcseconds search radius. Top row: Predicted versus 'actual' photometric redshift of tested clusters with frequency histograms of the distributions. Bottom row: Non-absolute photometric redshift prediction error versus 'actual' redshift of tested clusters with frequency histograms of the distributions. Other: '# clusters (total)' represents the total number of clusters with low richness which did not qualify for the WNMR dataset, '# clusters (radius)' represents the number of clusters with low richness which did not qualify for the WNMR dataset that have observed galaxies within a 32 arcseconds search radius, '# clusters (shown)' represents the number of clusters with low richness which did not qualify for the WNMR dataset that have observed galaxies within a 32 arcseconds search radius with full bootstrap resamples returned,  $\tilde{E}_z$  represents the median of photometric redshift prediction errors across all tested clusters within a 32 arcseconds search radius with full bootstrap resamples returned.



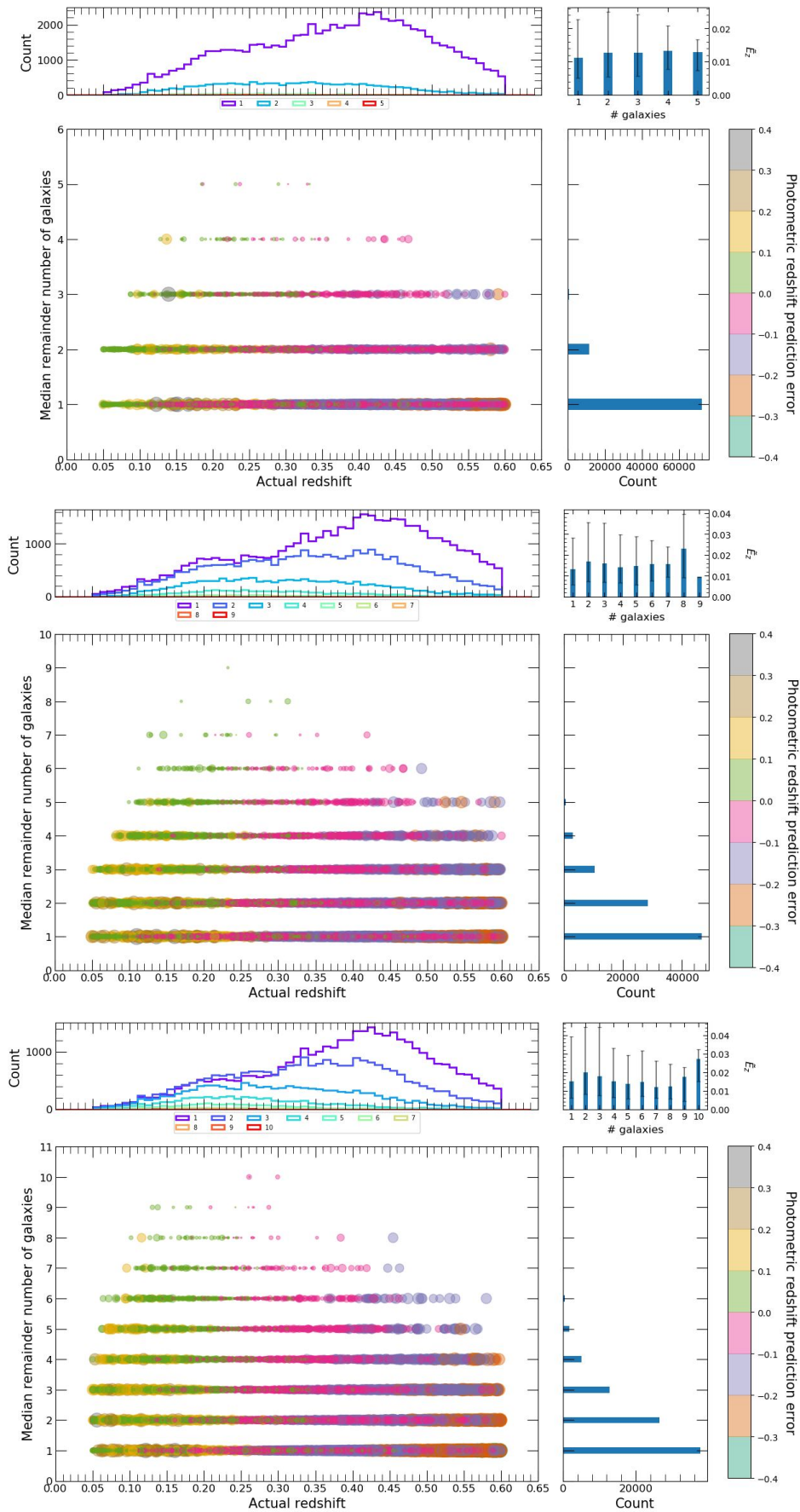
**Figure S35.** This figure displays the performance of photometric redshift predictions of clusters with low richness, which did not qualify for the WNMR dataset, that had partial bootstrap resamples returned within a 10 arcseconds search radius. Top row: Predicted versus 'actual' photometric redshift of tested clusters with frequency histograms of the distributions. Bottom row: Non-absolute photometric redshift prediction error versus 'actual' redshift of tested clusters with frequency histograms of the distributions. Other: '# clusters (total)' represents the total number of clusters with low richness which did not qualify for the WNMR dataset, '# clusters (radius)' represents the number of clusters with low richness which did not qualify for the WNMR dataset that have observed galaxies within a 10 arcseconds search radius, '# clusters (shown)' represents the number of clusters with low richness which did not qualify for the WNMR dataset that have observed galaxies within a 10 arcseconds search radius with partial bootstrap resamples returned,  $\bar{E}_z$  represents the median of photometric redshift prediction errors across all tested clusters within a 10 arcseconds search radius with partial bootstrap resamples returned.



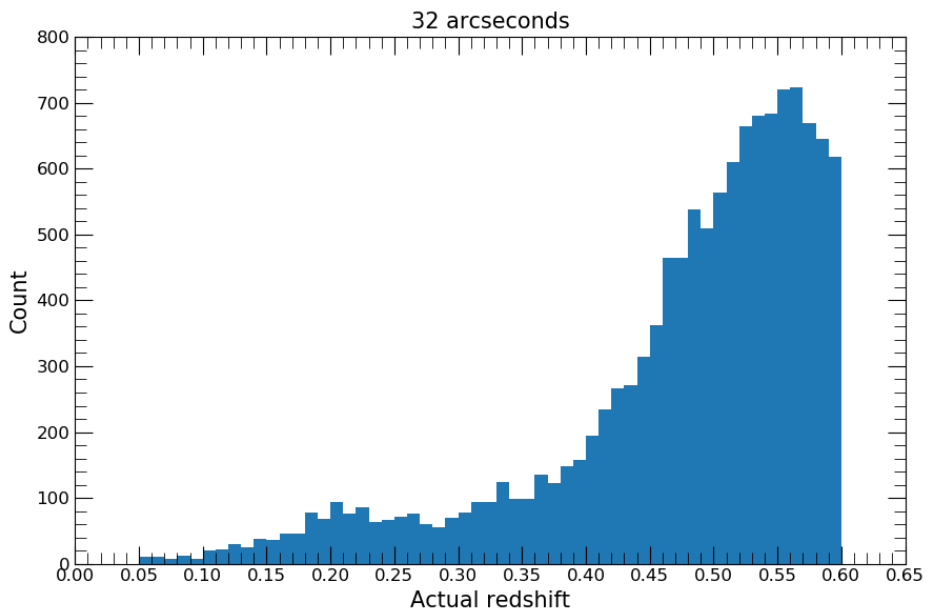
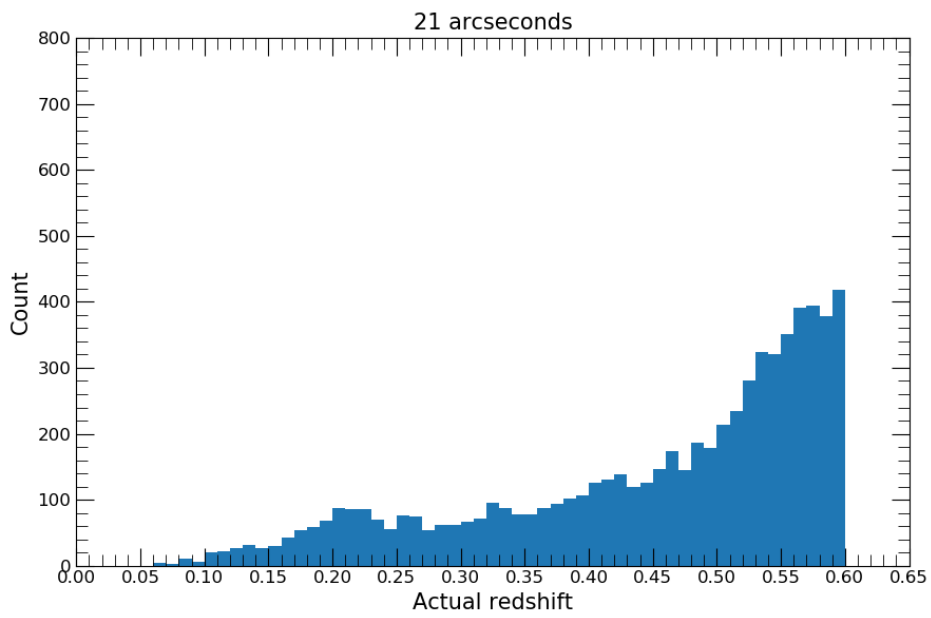
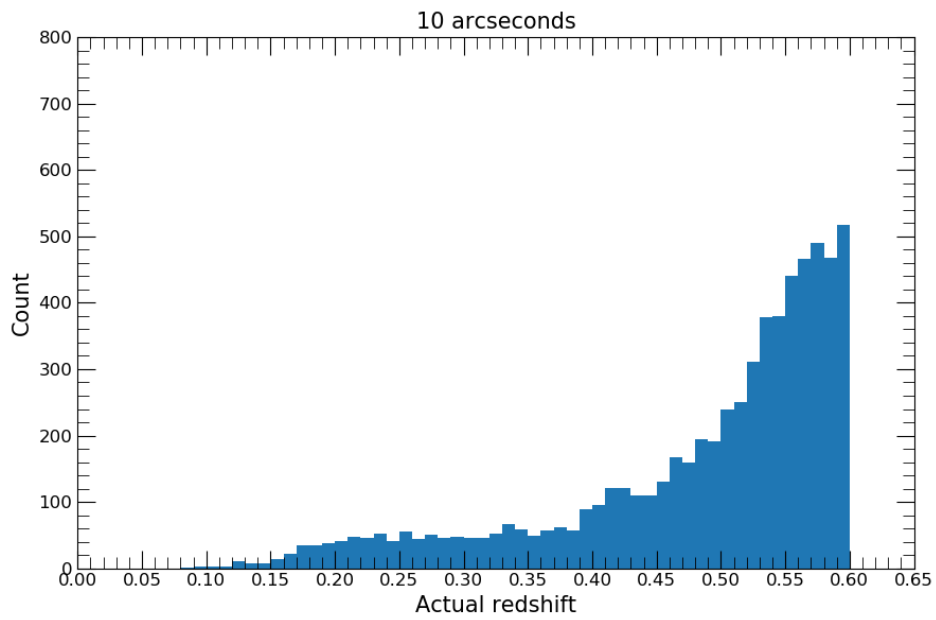
**Figure S36.** This figure displays the performance of photometric redshift predictions of clusters with low richness, which did not qualify for the WNMR dataset, that had partial bootstrap resamples returned within a 21 arcseconds search radius. Top row: Predicted versus 'actual' photometric redshift of tested clusters with frequency histograms of the distributions. Bottom row: Non-absolute photometric redshift prediction error versus 'actual' redshift of tested clusters with frequency histograms of the distributions. Other: '# clusters (total)' represents the total number of clusters with low richness which did not qualify for the WNMR dataset, '# clusters (radius)' represents the number of clusters with low richness which did not qualify for the WNMR dataset that have observed galaxies within a 21 arcseconds search radius, '# clusters (shown)' represents the number of clusters with low richness which did not qualify for the WNMR dataset that have observed galaxies within a 21 arcseconds search radius with partial bootstrap resamples returned,  $\bar{E}_z$  represents the median of photometric redshift prediction errors across all tested clusters within a 21 arcseconds search radius with partial bootstrap resamples returned.



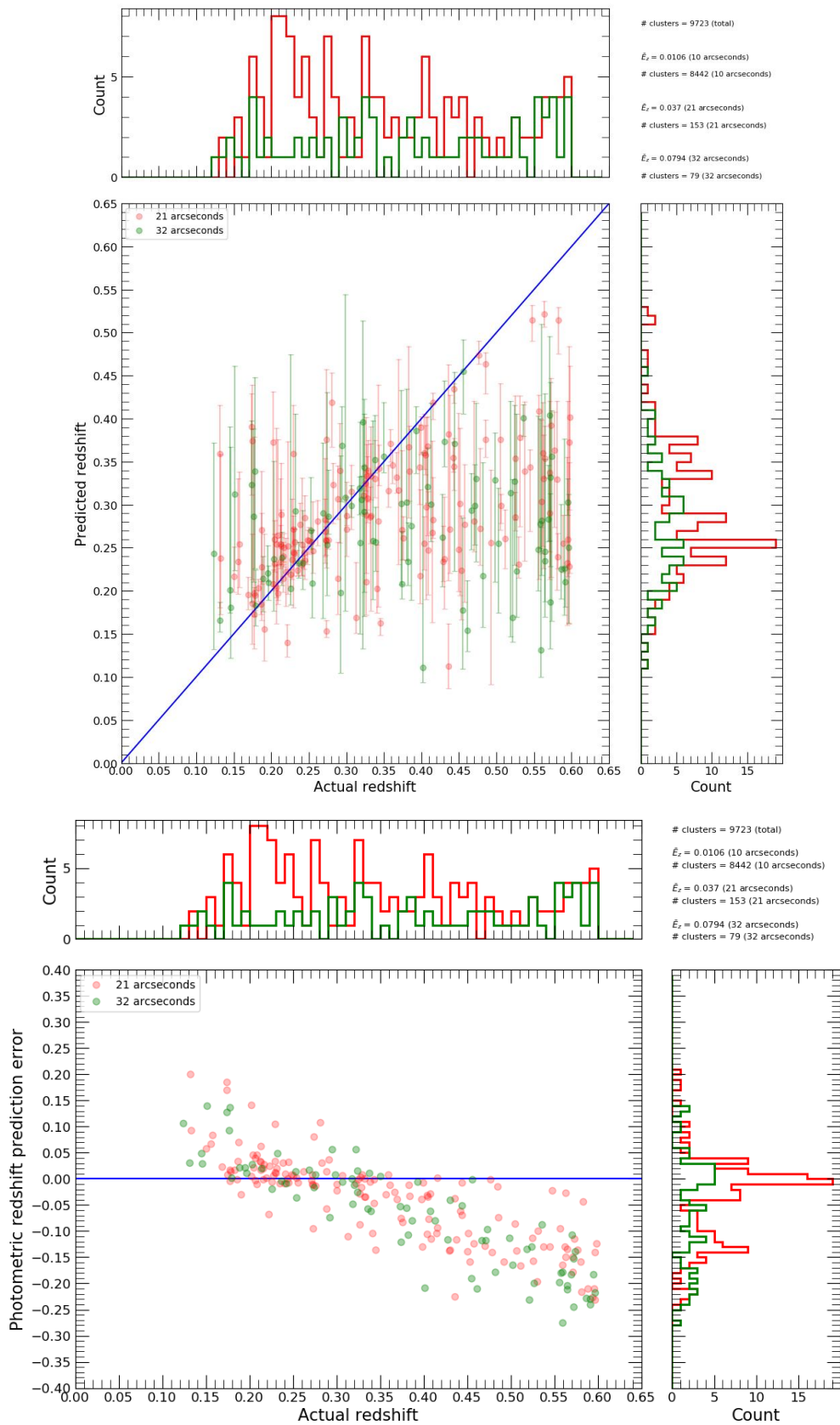
**Figure S37.** This figure displays the performance of photometric redshift predictions of clusters with low richness, which did not qualify for the WNMR dataset, that had partial bootstrap resamples returned within a 32 arcseconds search radius. Top row: Predicted versus 'actual' photometric redshift of tested clusters with frequency histograms of the distributions. Bottom row: Non-absolute photometric redshift prediction error versus 'actual' redshift of tested clusters with frequency histograms of the distributions. Other: '# clusters (total)' represents the total number of clusters with low richness which did not qualify for the WNMR dataset, '# clusters (radius)' represents the number of clusters with low richness which did not qualify for the WNMR dataset that have observed galaxies within a 32 arcseconds search radius, '# clusters (shown)' represents the number of clusters with low richness which did not qualify for the WNMR dataset that have observed galaxies within a 32 arcseconds search radius with partial bootstrap resamples returned,  $\bar{E}_z$  represents the median of photometric redshift prediction errors across all tested clusters within a 32 arcseconds search radius with partial bootstrap resamples returned.



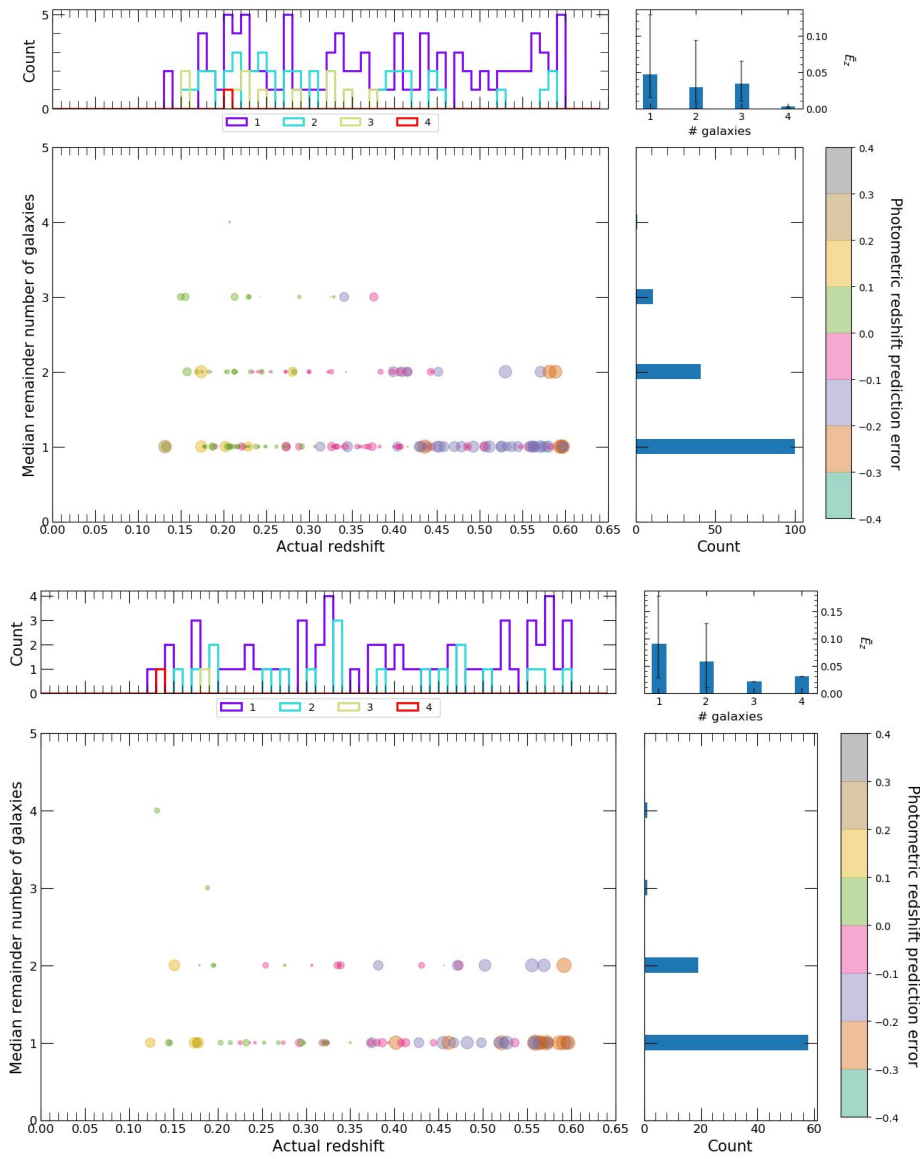
**Figure S38.** This figure displays the number of galaxies used in photometric redshift predictions of clusters with low richness versus ‘actual’ redshift of tested clusters, which did not qualify for the WNMR dataset, where predictions had full bootstrap resamples returned within a 10 (top row), 21 (middle row) and 32 (bottom row) arcseconds search radius. It should be noted that the size of individual points change in relation to the value of the non-absolute photometric redshift prediction error. Frequency histograms of the distributions are also shown.  $\bar{E}_z$  represents the median of photometric redshift prediction errors across all tested clusters for each number of galaxies bin.



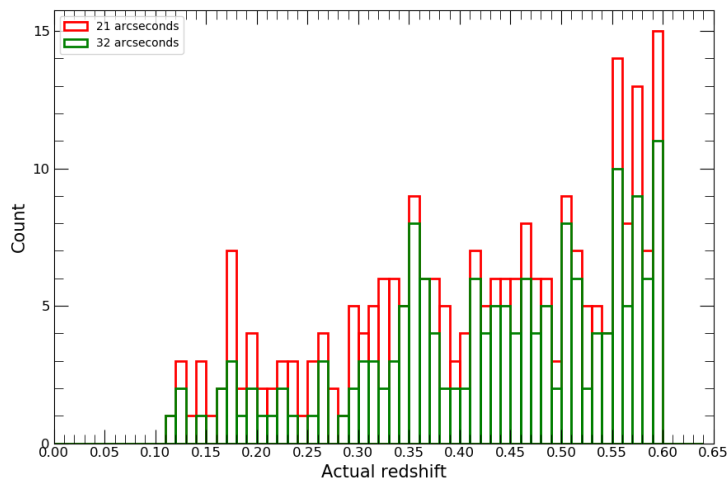
**Figure S39.** This figure displays the ‘actual’ redshift distributions of clusters with low richness, which did not qualify for the WNMR dataset, that had no bootstrap resamples returned within a 10 (top row), 21 (middle row) and 32 (bottom row) arcseconds search radius.



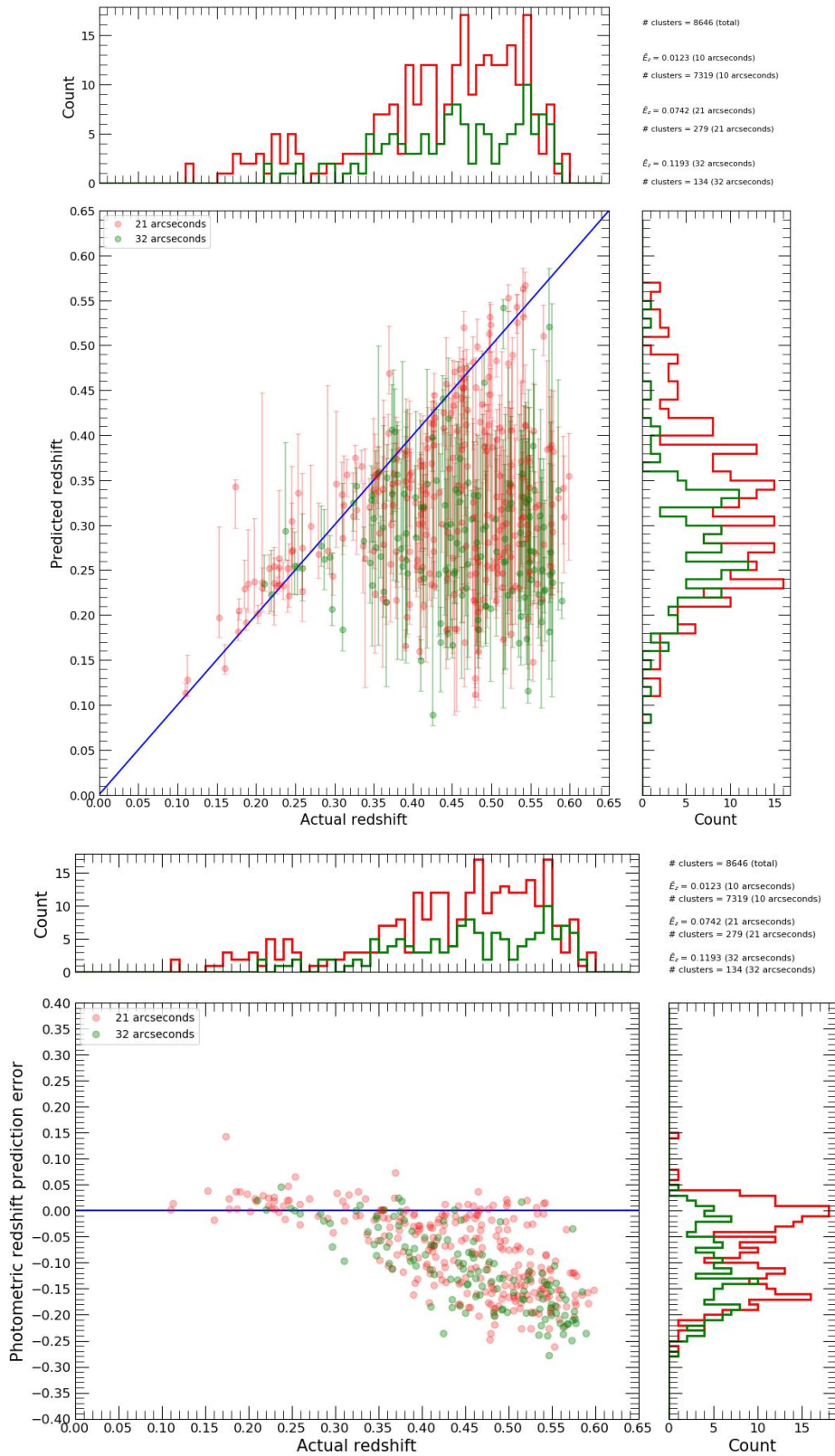
**Figure S40.** This figure displays the performance of photometric redshift predictions of clusters for the WNMR test set that had full bootstrap resamples returned within a 21 (red) or 32 (green) arcseconds search radius. If a cluster has no or partial bootstrap resamples returned at 10 arcseconds then the search radius is increased until a prediction with full bootstrap resamples returned is obtained. Top row: Predicted versus 'actual' photometric redshift of tested clusters with frequency histograms of the distributions. Bottom row: Non-absolute photometric redshift prediction error versus 'actual' redshift of tested clusters with frequency histograms of the distributions. Other: '# clusters (total)' represents the total number of clusters for the WNMR test set, '# clusters' represents the number of clusters for the WNMR test set that have observed galaxies within a 10, 21 and 32 arcseconds search radii with full bootstrap resamples returned,  $\bar{E}_z$  represents the median of photometric redshift prediction errors across all tested clusters within a 10, 21 and 32 arcseconds search radii with full bootstrap resamples returned.



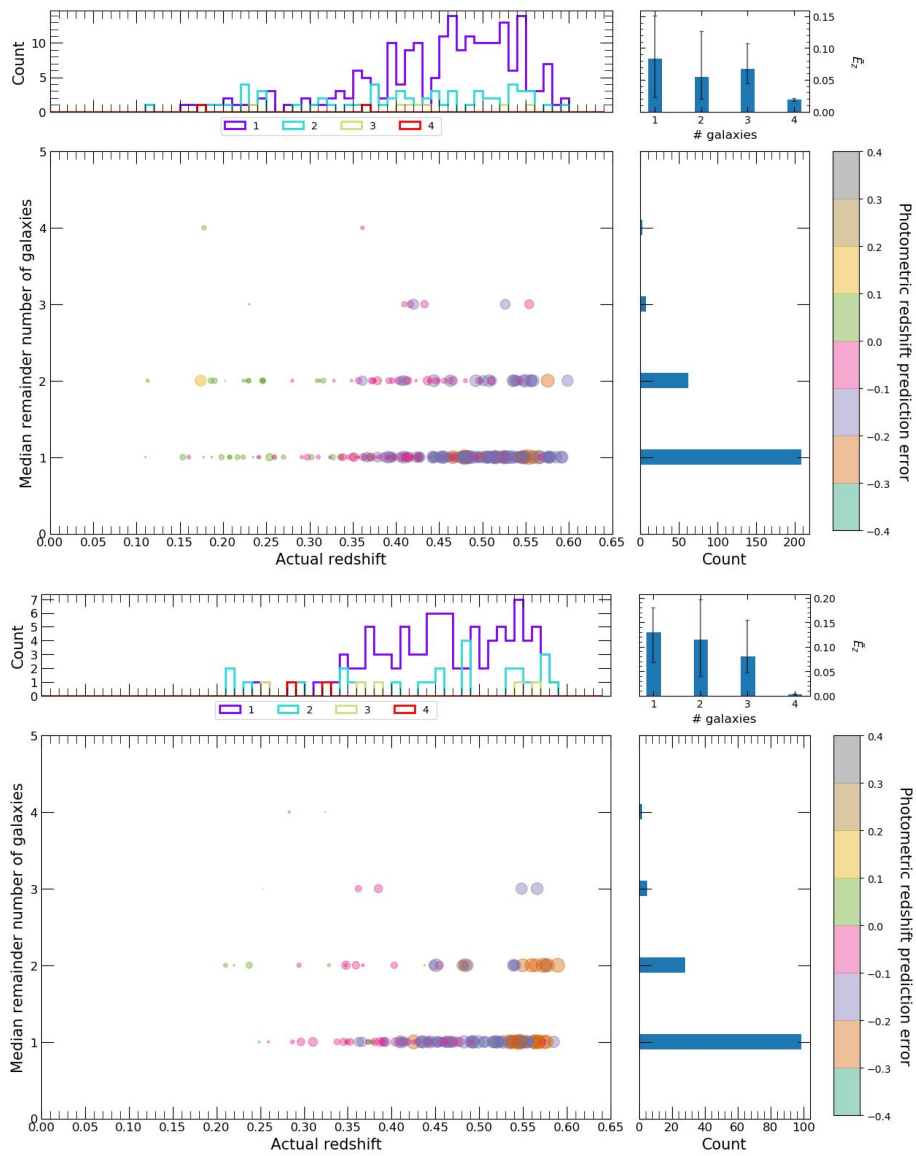
**Figure S41.** This figure displays the number of galaxies used in photometric redshift predictions versus 'actual' redshift of tested clusters for the WNMR test set, where predictions had full bootstrap resamples returned within a 21 (top row) or 32 (bottom row) arcseconds search radius. If a cluster has no or partial bootstrap resamples returned at 10 arcseconds then the search radius is increased until a prediction with full bootstrap resamples returned is obtained. It should be noted that the size of individual points change in relation to the value of the non-absolute photometric redshift prediction error. Frequency histograms of the distributions are also shown.  $\tilde{E}_z$  represents the median of photometric redshift prediction errors across all tested clusters for each number of galaxies bin.



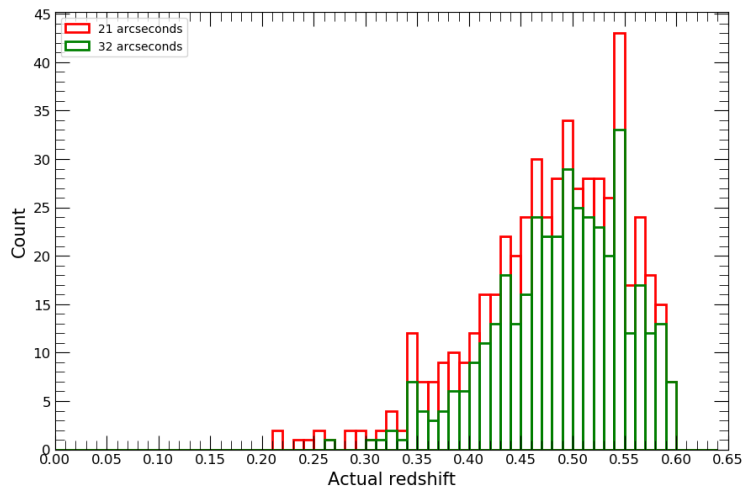
**Figure S42.** This figure displays the 'actual' redshift distributions of the remaining clusters from the WNMR test set that had no bootstrap resamples returned within a 21 (red) or 32 (green) arcseconds search radius.



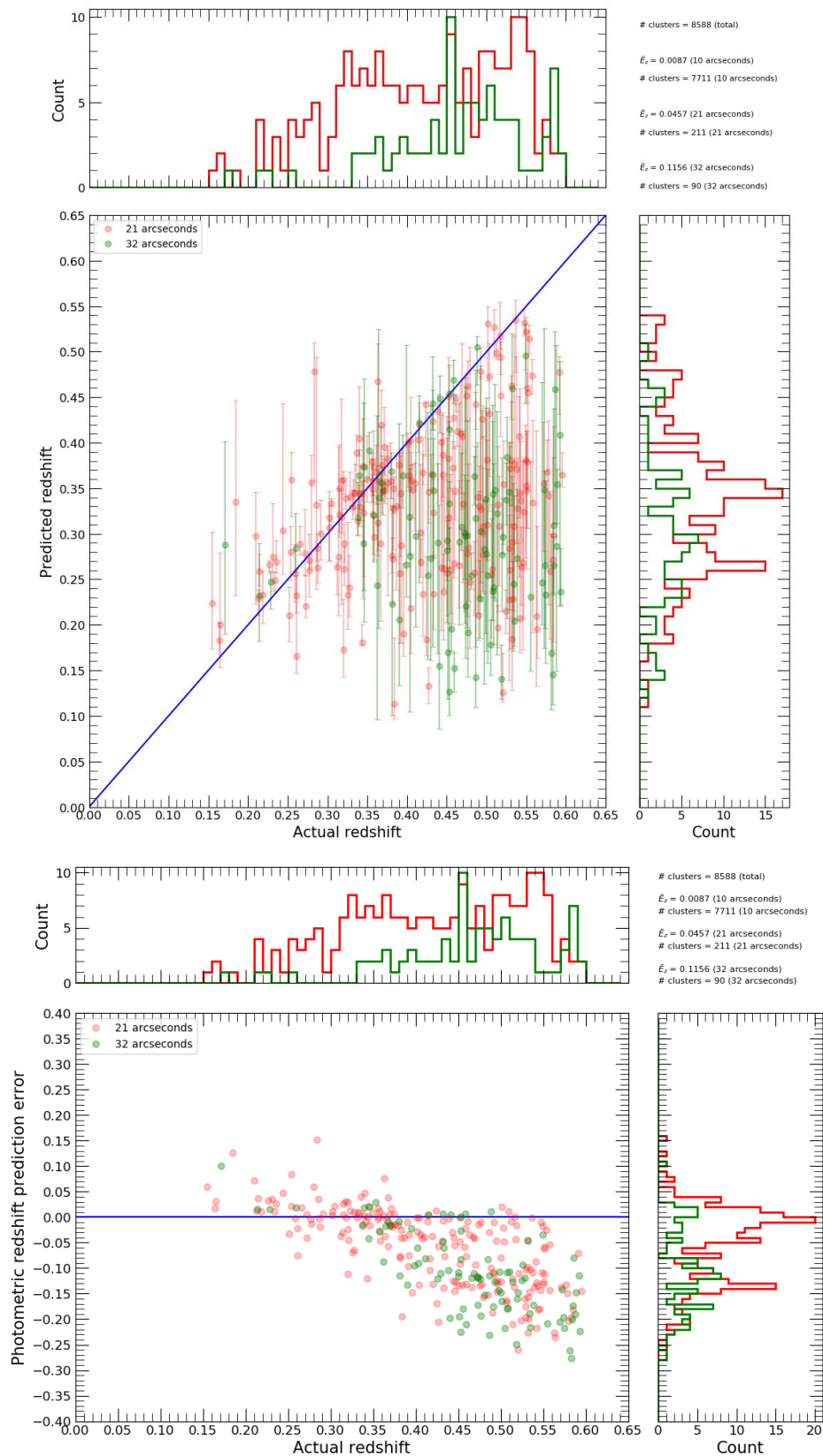
**Figure S43.** This figure displays the performance of photometric redshift predictions of clusters for the RNMW test set that had full bootstrap resamples returned within a 21 (red) or 32 (green) arcseconds search radii. If a cluster has no or partial bootstrap resamples returned at 10 arcseconds then the search radius is increased until a prediction with full bootstrap resamples returned is obtained. Top row: Predicted versus 'actual' photometric redshift of tested clusters with frequency histograms of the distributions. Bottom row: Non-absolute photometric redshift prediction error versus 'actual' redshift of tested clusters with frequency histograms of the distributions. Other: '# clusters (total)' represents the total number of clusters for the RNMW test set, '# clusters' represents the number of clusters for the RNMW test set that have observed galaxies within a 10, 21 and 32 arcseconds search radii with full bootstrap resamples returned,  $\bar{E}_z$  represents the median of photometric redshift prediction errors across all tested clusters within a 10, 21 and 32 arcseconds search radii with full bootstrap resamples returned.



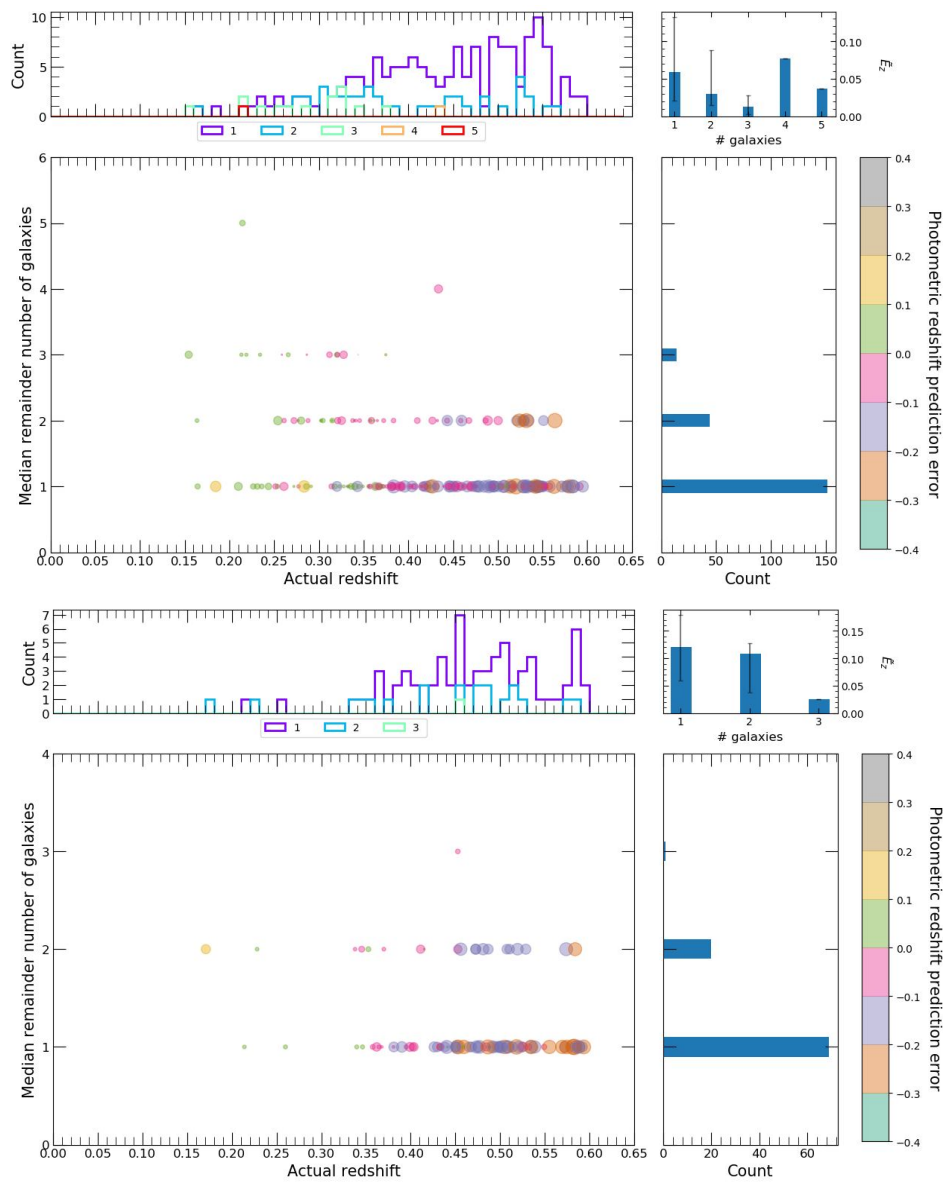
**Figure S44.** This figure displays the number of galaxies used in photometric redshift predictions versus ‘actual’ redshift of tested clusters for the RNMW test set, where predictions had full bootstrap resamples returned within a 21 (top row) or 32 (bottom row) arcseconds search radius. If a cluster has no or partial bootstrap resamples returned at 10 arcseconds then the search radius is increased until a prediction with full bootstrap resamples returned is obtained. It should be noted that the size of individual points change in relation to the value of the non-absolute photometric redshift prediction error. Frequency histograms of the distributions are also shown.  $\tilde{E}_z$  represents the median of photometric redshift prediction errors across all tested clusters for each number of galaxies bin.



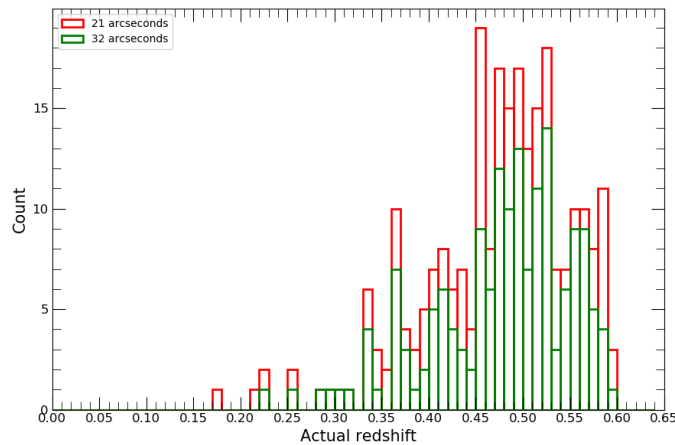
**Figure S45.** This figure displays the ‘actual’ redshift distributions of the remaining clusters from the RNMW test set that had no bootstrap resamples returned within a 21 (red) or 32 (green) arcseconds search radius.



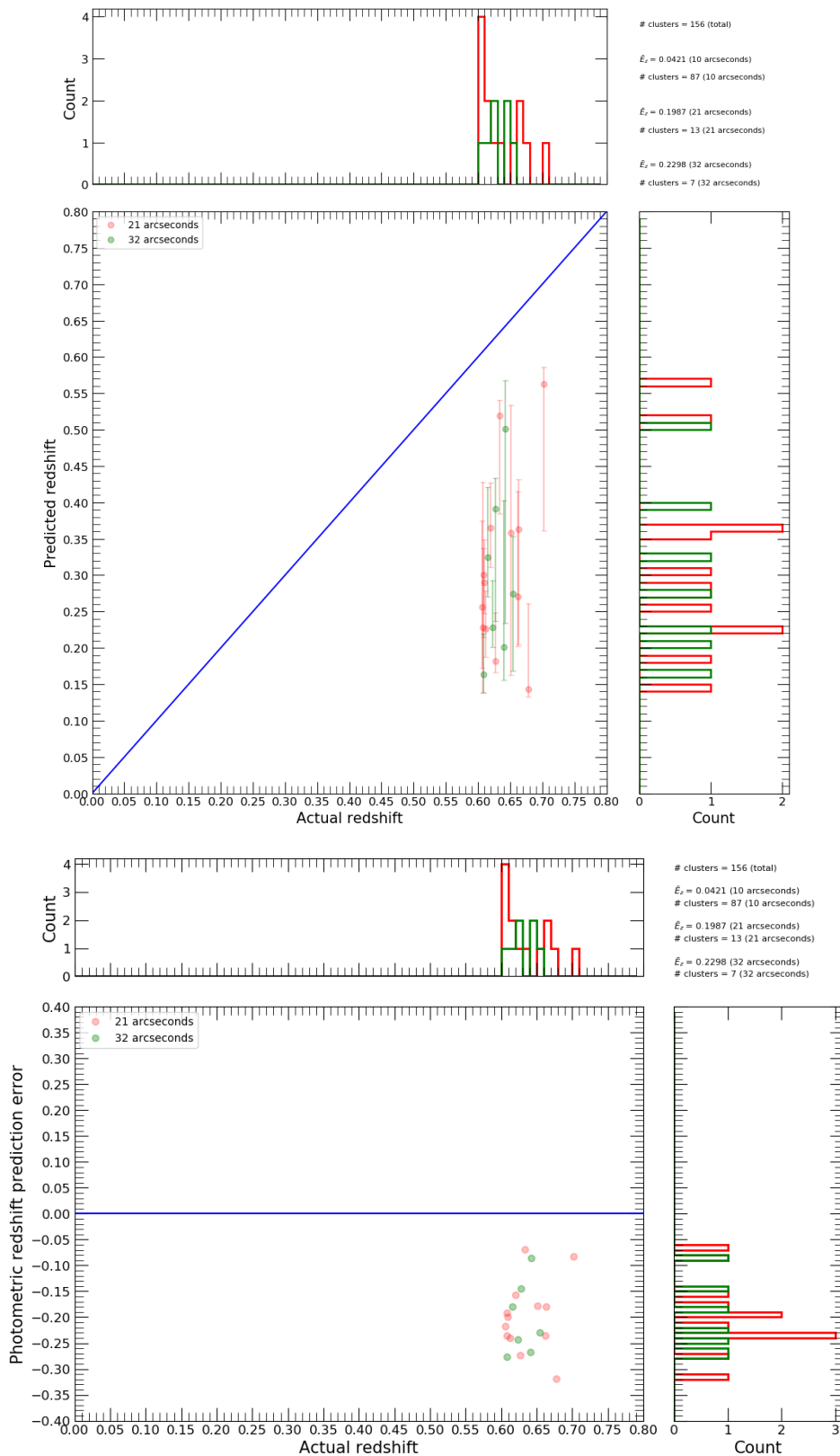
**Figure S46.** This figure displays the performance of photometric redshift predictions of clusters with low richness, which did not qualify for the MWAR dataset, that had full bootstrap resamples returned within a 21 (red) or 32 (green) arcseconds search radii. If a cluster has no or partial bootstrap resamples returned at 10 arcseconds then the search radius is increased until a prediction with full bootstrap resamples returned is obtained. Top row: Predicted versus 'actual' photometric redshift of tested clusters with frequency histograms of the distributions. Bottom row: Non-absolute photometric redshift prediction error versus 'actual' redshift of tested clusters with frequency histograms of the distributions. Other: '# clusters (total)' represents the total number of clusters with low richness which did not qualify for the MWAR dataset, '# clusters' represents the number of clusters with low richness which did not qualify for the MWAR dataset that have observed galaxies within a 10, 21 and 32 arcseconds search radii with full bootstrap resamples returned,  $\tilde{E}_z$  represents the median of photometric redshift prediction errors across all tested clusters within a 10, 21 and 32 arcseconds search radii with full bootstrap resamples returned.



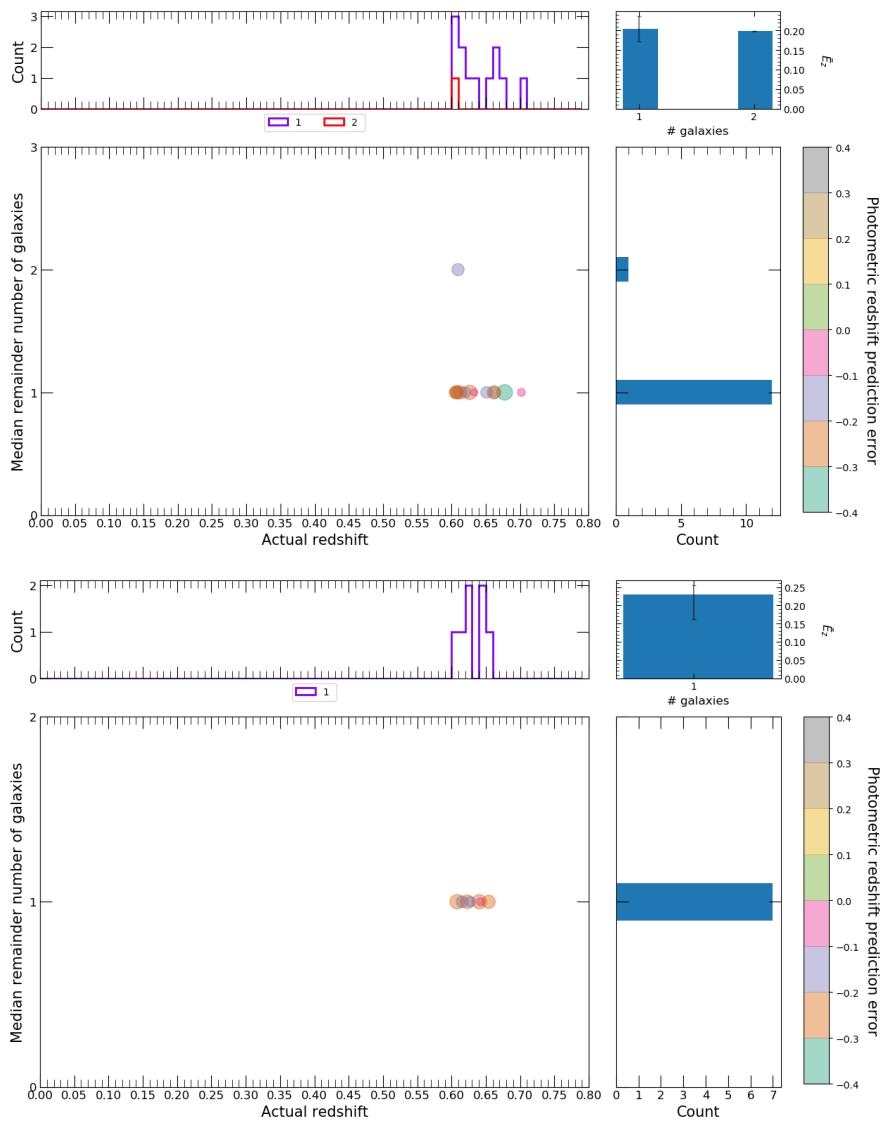
**Figure S47.** This figure displays the number of galaxies used in photometric redshift predictions of clusters with low richness versus ‘actual’ redshift of tested clusters, which did not qualify for the MWAR dataset, where predictions had full bootstrap resamples returned within a 21 (top row) or 32 (bottom row) arcseconds search radius. If a cluster has no or partial bootstrap resamples returned at 10 arcseconds then the search radius is increased until a prediction with full bootstrap resamples returned is obtained. It should be noted that the size of individual points change in relation to the value of the non-absolute photometric redshift prediction error. Frequency histograms of the distributions are also shown.  $\tilde{E}_z$  represents the median of photometric redshift prediction errors across all tested clusters for each number of galaxies bin.



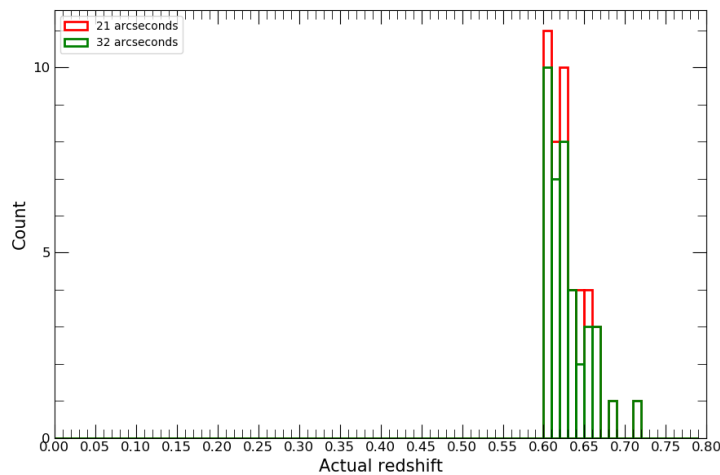
**Figure S48.** This figure displays the ‘actual’ redshift distributions of clusters with low richness, which did not qualify for the MWAR dataset, that had no bootstrap resamples returned within a 21 (red) or 32 (green) arcseconds search radius.



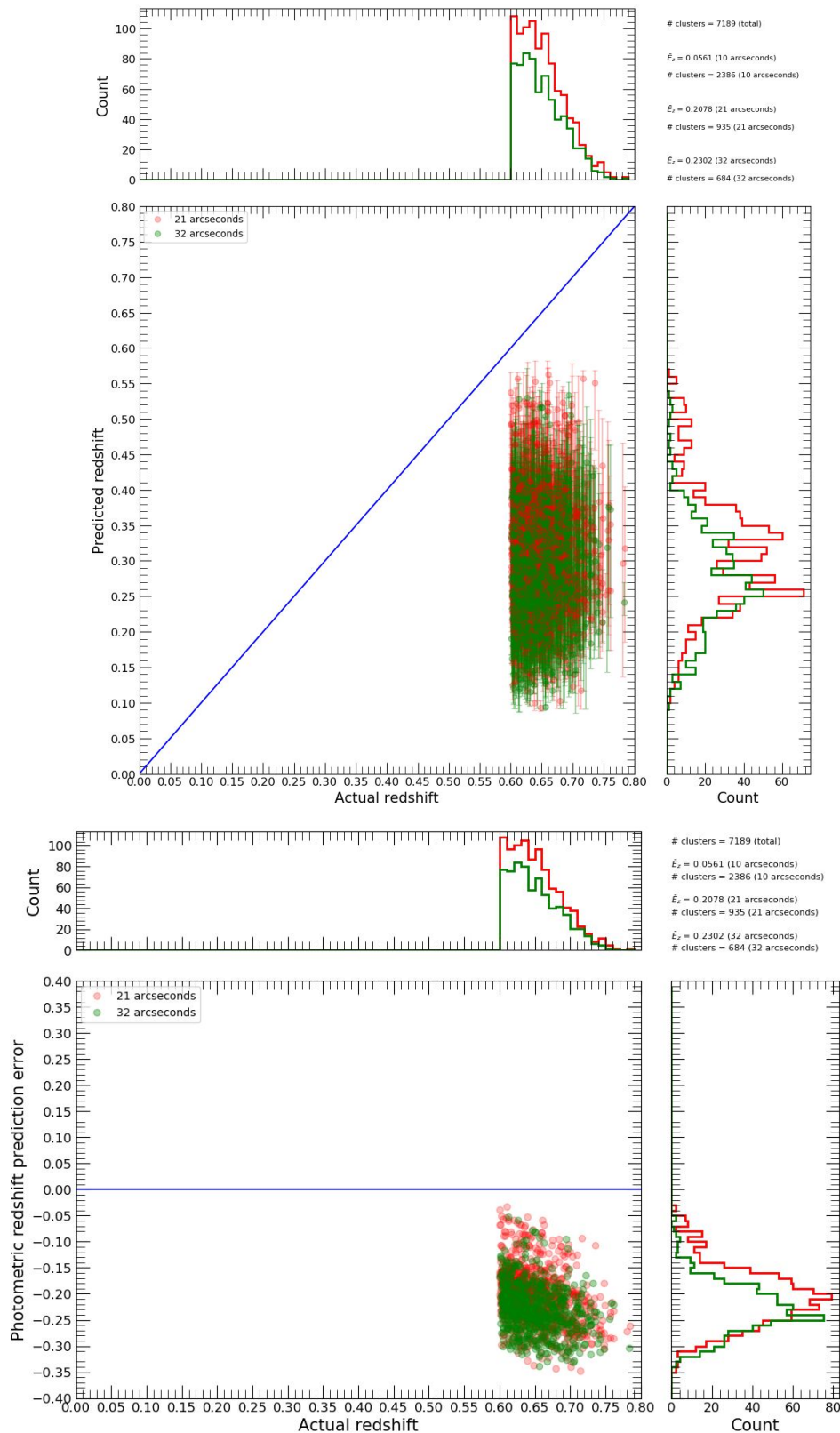
**Figure S49.** This figure displays the performance of photometric redshift predictions of clusters at high redshift, which did not qualify for the WNMN dataset, that had full bootstrap resamples returned within a 21 (red) or 32 (green) arcseconds search radii. If a cluster has no or partial bootstrap resamples returned at 10 arcseconds then the search radius is increased until a prediction with full bootstrap resamples returned is obtained. Top row: Predicted versus 'actual' photometric redshift of tested clusters with frequency histograms of the distributions. Bottom row: Non-absolute photometric redshift prediction error versus 'actual' redshift of tested clusters with frequency histograms of the distributions. Other: '# clusters (total)' represents the total number of clusters at high redshift which did not qualify for the WNMN dataset, '# clusters' represents the number of clusters at high redshift which did not qualify for the WNMN dataset that have observed galaxies within a 10, 21 and 32 arcseconds search radii with full bootstrap resamples returned,  $\bar{E}_z$  represents the median of photometric redshift prediction errors across all tested clusters within a 10, 21 and 32 arcseconds search radii with full bootstrap resamples returned.



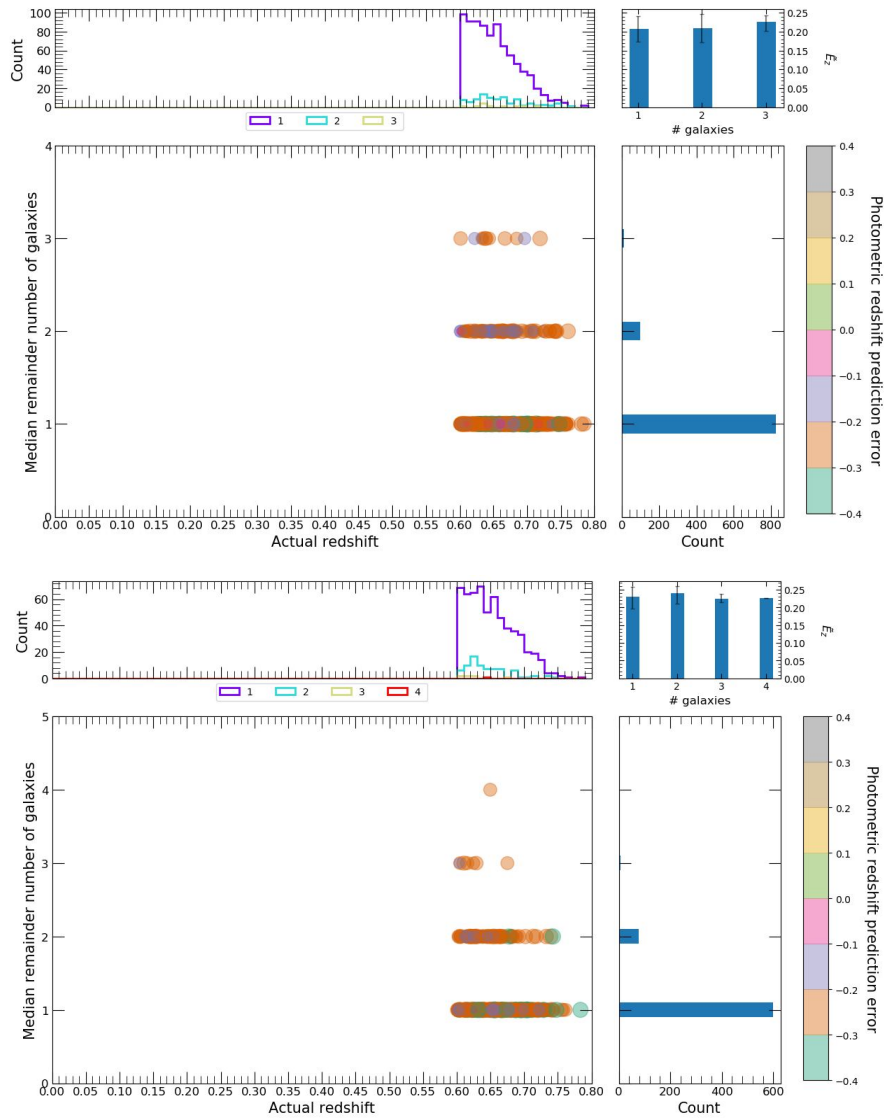
**Figure S50.** This figure displays the number of galaxies used in photometric redshift predictions of clusters at high redshift versus 'actual' redshift of tested clusters, which did not qualify for the WNMR dataset, where predictions had full bootstrap resamples returned within a 21 (top row) or 32 (bottom row) arcseconds search radius. If a cluster has no or partial bootstrap resamples returned at 10 arcseconds then the search radius is increased until a prediction with full bootstrap resamples returned is obtained. It should be noted that the size of individual points change in relation to the value of the non-absolute photometric redshift prediction error. Frequency histograms of the distributions are also shown.  $\bar{E}_z$  represents the median of photometric redshift prediction errors across all tested clusters for each number of galaxies bin.



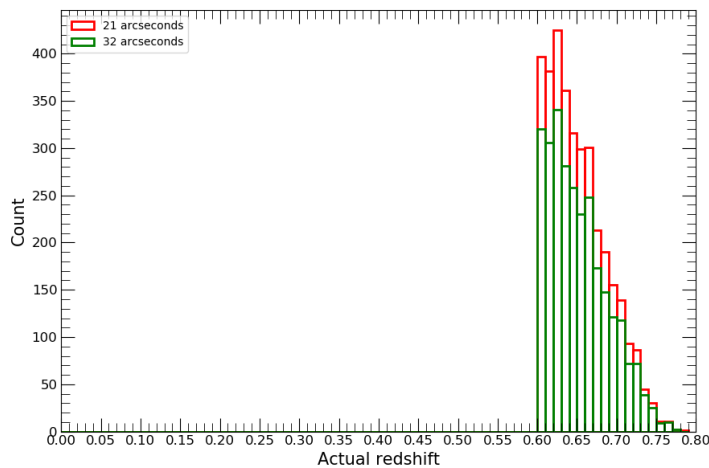
**Figure S51.** This figure displays the 'actual' redshift distributions of clusters at high redshift, which did not qualify for the WNMR dataset, that had no bootstrap resamples returned within a 21 (red) or 32 (green) arcseconds search radius.



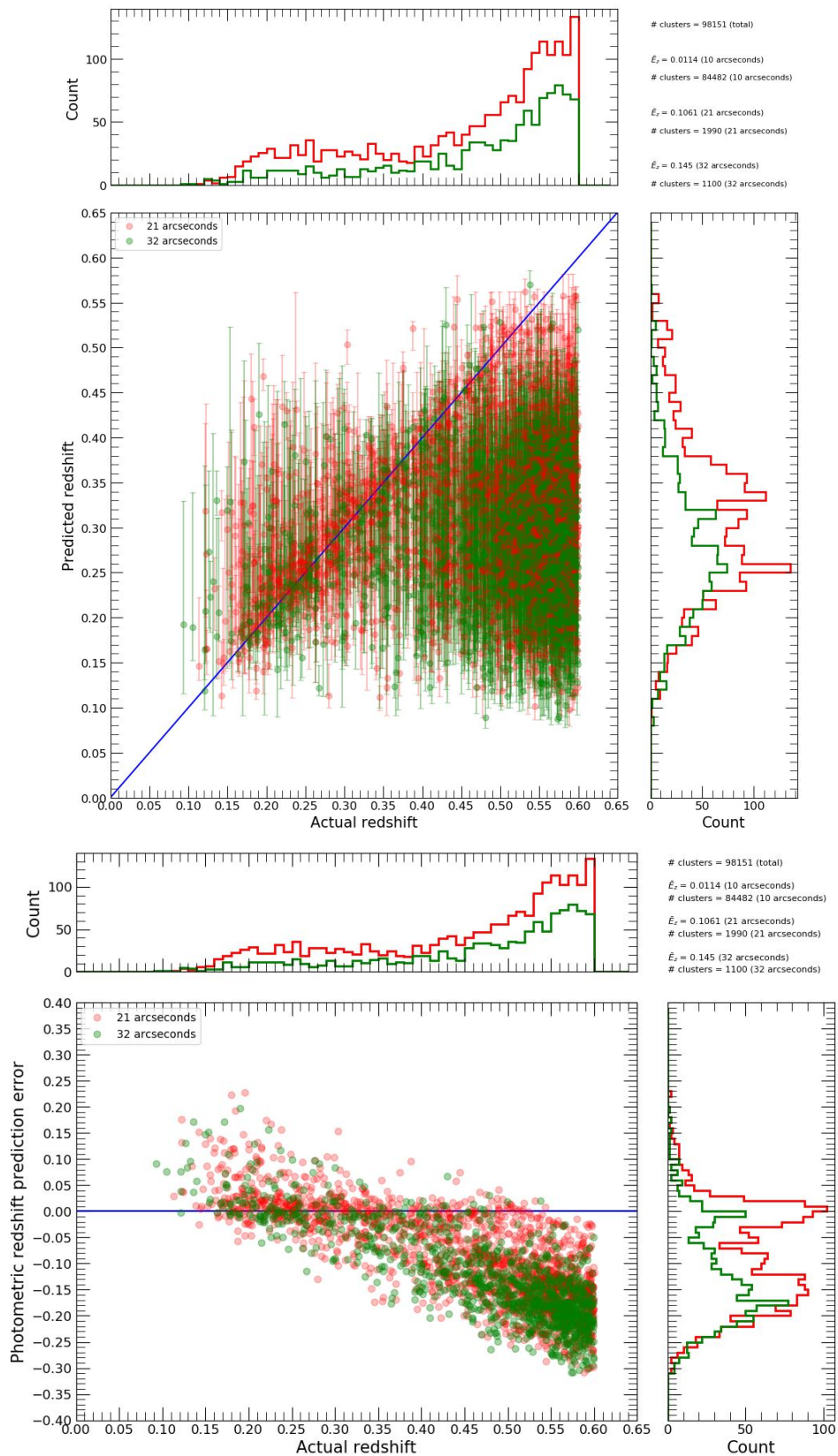
**Figure S52.** This figure displays the performance of photometric redshift predictions of clusters at high redshift with low richness, which did not qualify for the WNMR dataset, that had full bootstrap resamples returned within a 21 (red) or 32 (green) arcseconds search radii. If a cluster has no or partial bootstrap resamples returned at 10 arcseconds then the search radius is increased until a prediction with full bootstrap resamples returned is obtained. Top row: Predicted versus 'actual' photometric redshift of tested clusters with frequency histograms of the distributions. Bottom row: Non-absolute photometric redshift prediction error versus 'actual' redshift of tested clusters with frequency histograms of the distributions. Other: '# clusters (total)' represents the total number of clusters at high redshift with low richness which did not qualify for the WNMR dataset, '# clusters' represents the number of clusters at high redshift with low richness which did not qualify for the WNMR dataset that have observed galaxies within a 10, 21 and 32 arcseconds search radii with full bootstrap resamples returned,  $\bar{E}_z$  represents the median of photometric redshift prediction errors across all tested clusters within a 10, 21 and 32 arcseconds search radii with full bootstrap resamples returned.



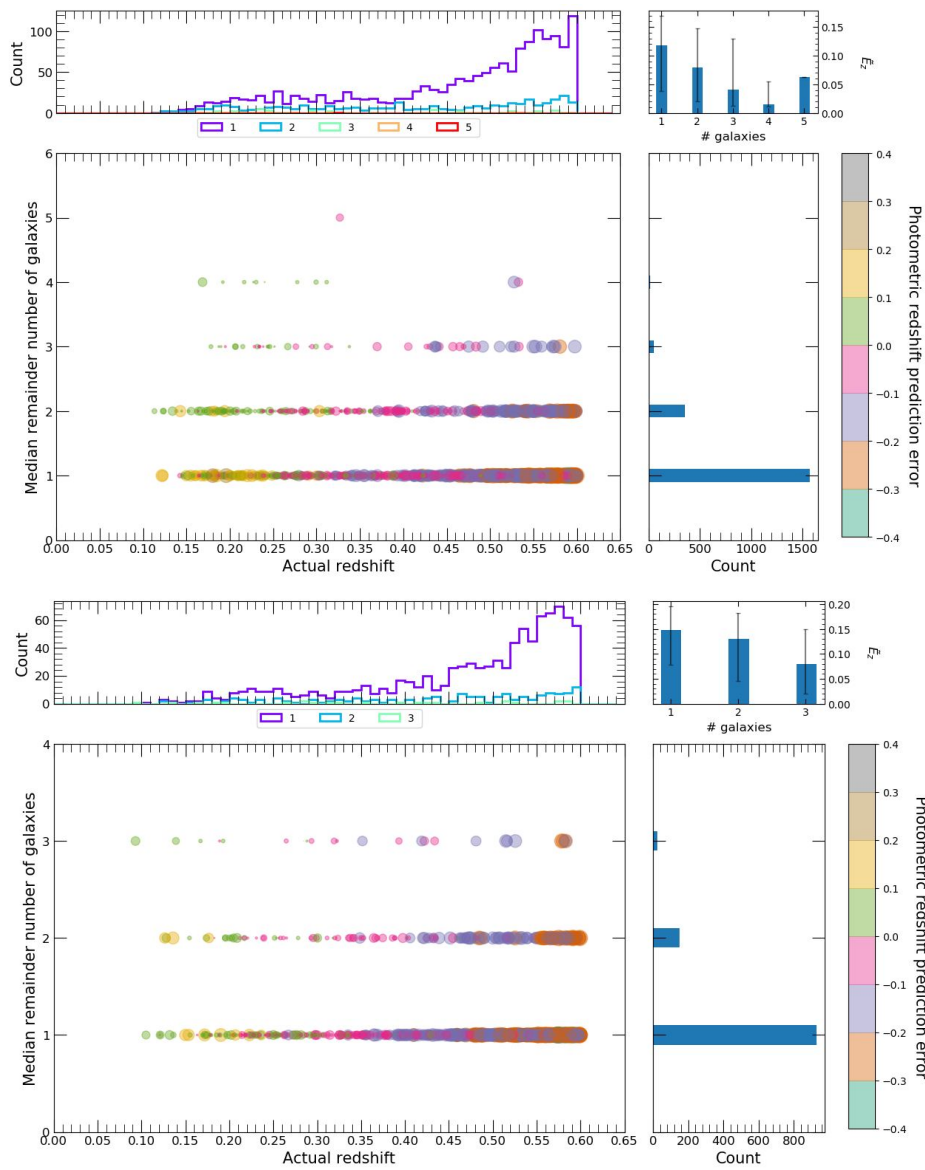
**Figure S53.** This figure displays the number of galaxies used in photometric redshift predictions of clusters at high redshift with low richness versus ‘actual’ redshift of tested clusters, which did not qualify for the WNMR dataset, where predictions had full bootstrap resamples returned within a 21 (top row) or 32 (bottom row) arcseconds search radius. If a cluster has no or partial bootstrap resamples returned at 10 arcseconds then the search radius is increased until a prediction with full bootstrap resamples returned is obtained. It should be noted that the size of individual points change in relation to the value of the non-absolute photometric redshift prediction error. Frequency histograms of the distributions are also shown.  $\bar{E}_z$  represents the median of photometric redshift prediction errors across all tested clusters for each number of galaxies bin.



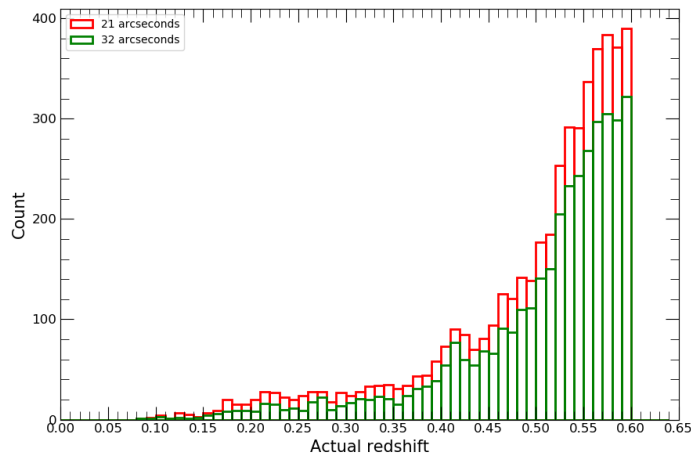
**Figure S54.** This figure displays the ‘actual’ redshift distributions of clusters at high redshift with low richness, which did not qualify for the WNMR dataset, that had no bootstrap resamples returned within a 21 (red) or 32 (green) arcseconds search radius.



**Figure S55.** This figure displays the performance of photometric redshift predictions of clusters with low richness, which did not qualify for the WNMR dataset, that had full bootstrap resamples returned within a 21 (red) or 32 (green) arcseconds search radii. If a cluster has no or partial bootstrap resamples returned at 10 arcseconds then the search radius is increased until a prediction with full bootstrap resamples returned is obtained. Top row: Predicted versus 'actual' photometric redshift of tested clusters with frequency histograms of the distributions. Bottom row: Non-absolute photometric redshift prediction error versus 'actual' redshift of tested clusters with frequency histograms of the distributions. Other: '# clusters (total)' represents the total number of clusters with low richness which did not qualify for the WNMR dataset, '# clusters' represents the number of clusters with low richness which did not qualify for the WNMR dataset that have observed galaxies within a 10, 21 and 32 arcseconds search radii with full bootstrap resamples returned,  $\bar{E}_z$  represents the median of photometric redshift prediction errors across all tested clusters within a 10, 21 and 32 arcseconds search radii with full bootstrap resamples returned.



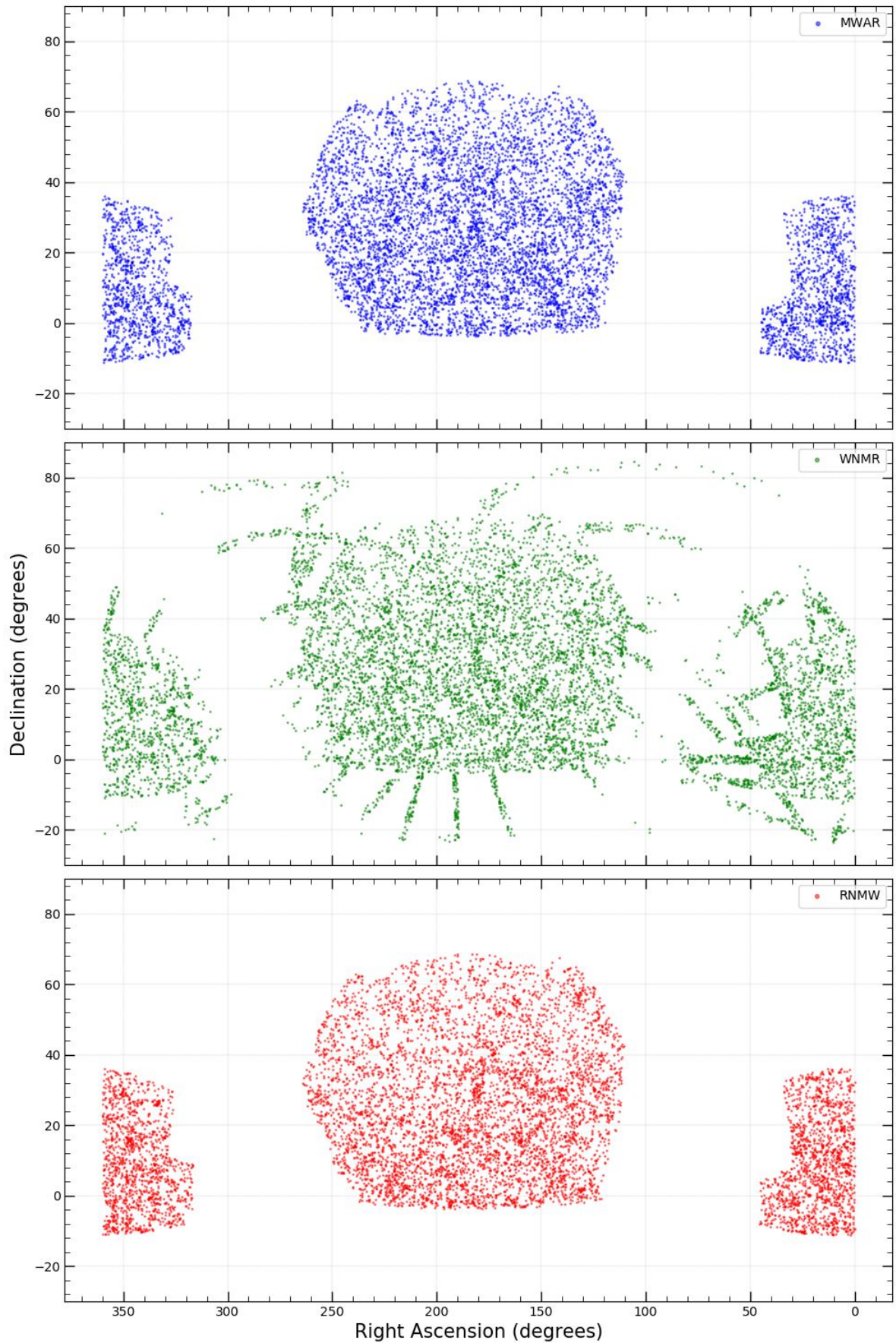
**Figure S56.** This figure displays the number of galaxies used in photometric redshift predictions of clusters with low richness versus ‘actual’ redshift of tested clusters, which did not qualify for the WNMR dataset, where predictions had full bootstrap resamples returned within a 21 (top row) or 32 (bottom row) arcseconds search radius. If a cluster has no or partial bootstrap resamples returned at 10 arcseconds then the search radius is increased until a prediction with full bootstrap resamples returned is obtained. It should be noted that the size of individual points change in relation to the value of the non-absolute photometric redshift prediction error. Frequency histograms of the distributions are also shown.  $\tilde{E}_z$  represents the median of photometric redshift prediction errors across all tested clusters for each number of galaxies bin.



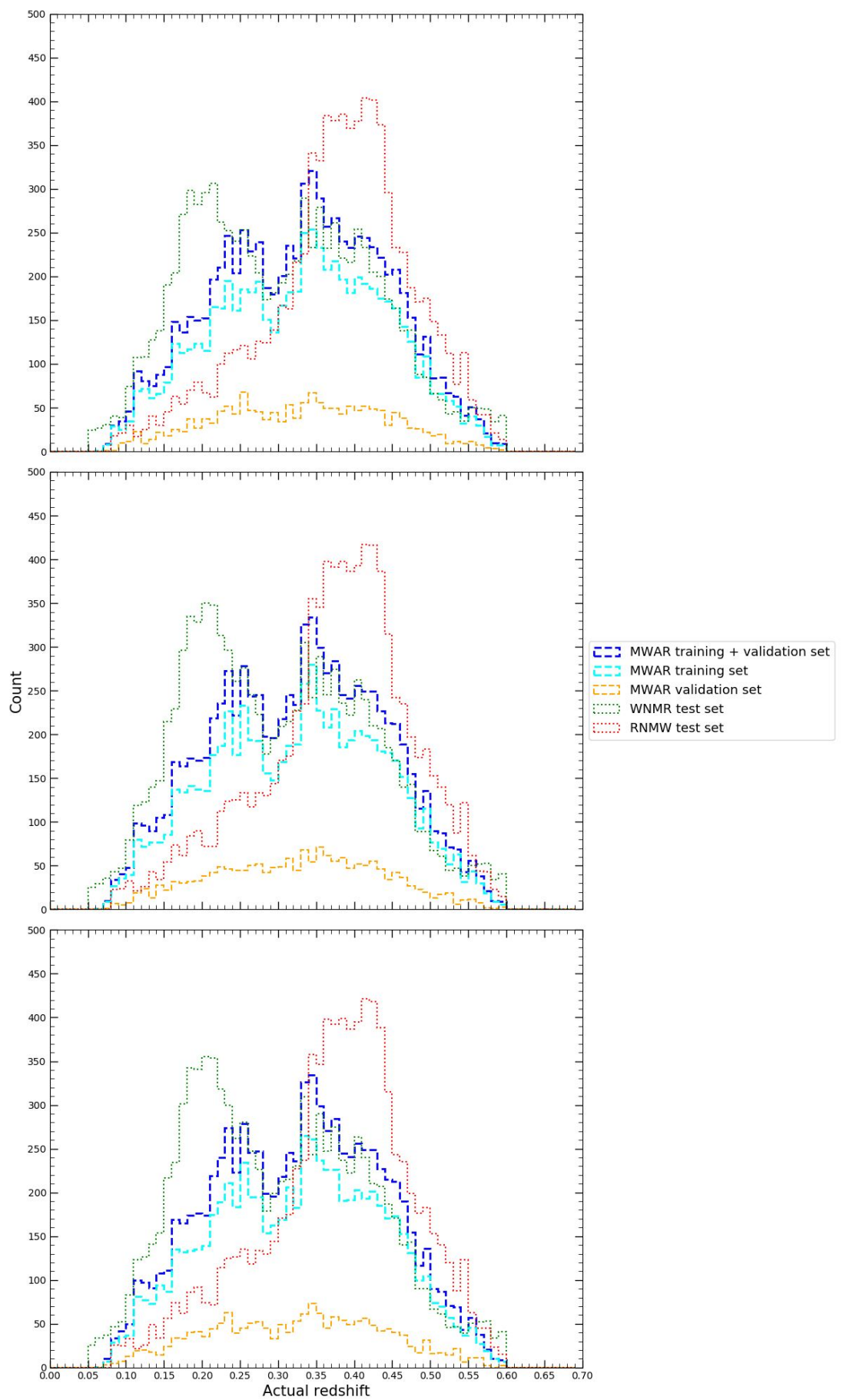
**Figure S57.** This figure displays the ‘actual’ redshift distributions of clusters with low richness, which did not qualify for the WNMR dataset, that had no bootstrap resamples returned within a 21 (red) or 32 (green) arcseconds search radius.



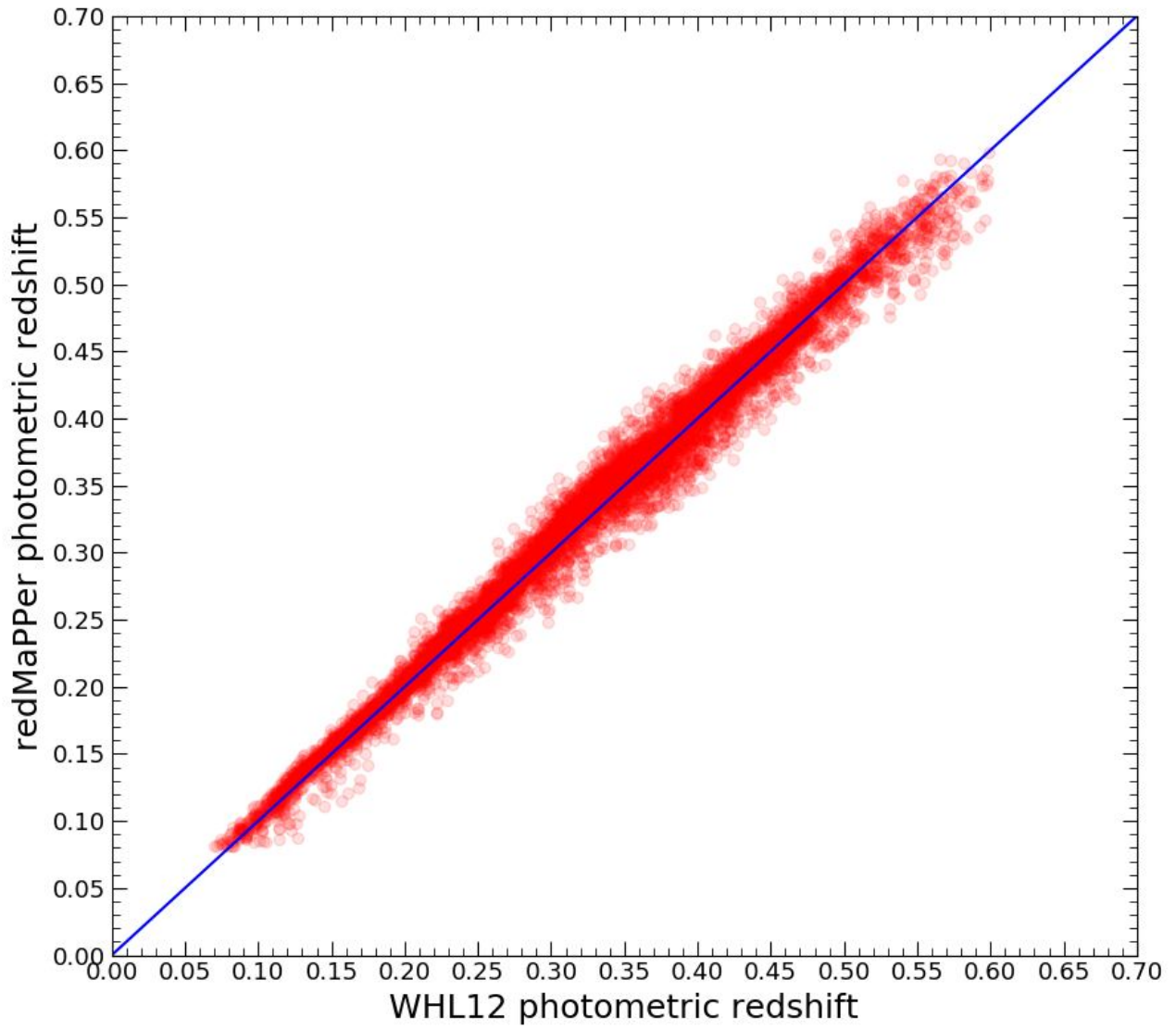
## SUPPLEMENTARY APPENDIX



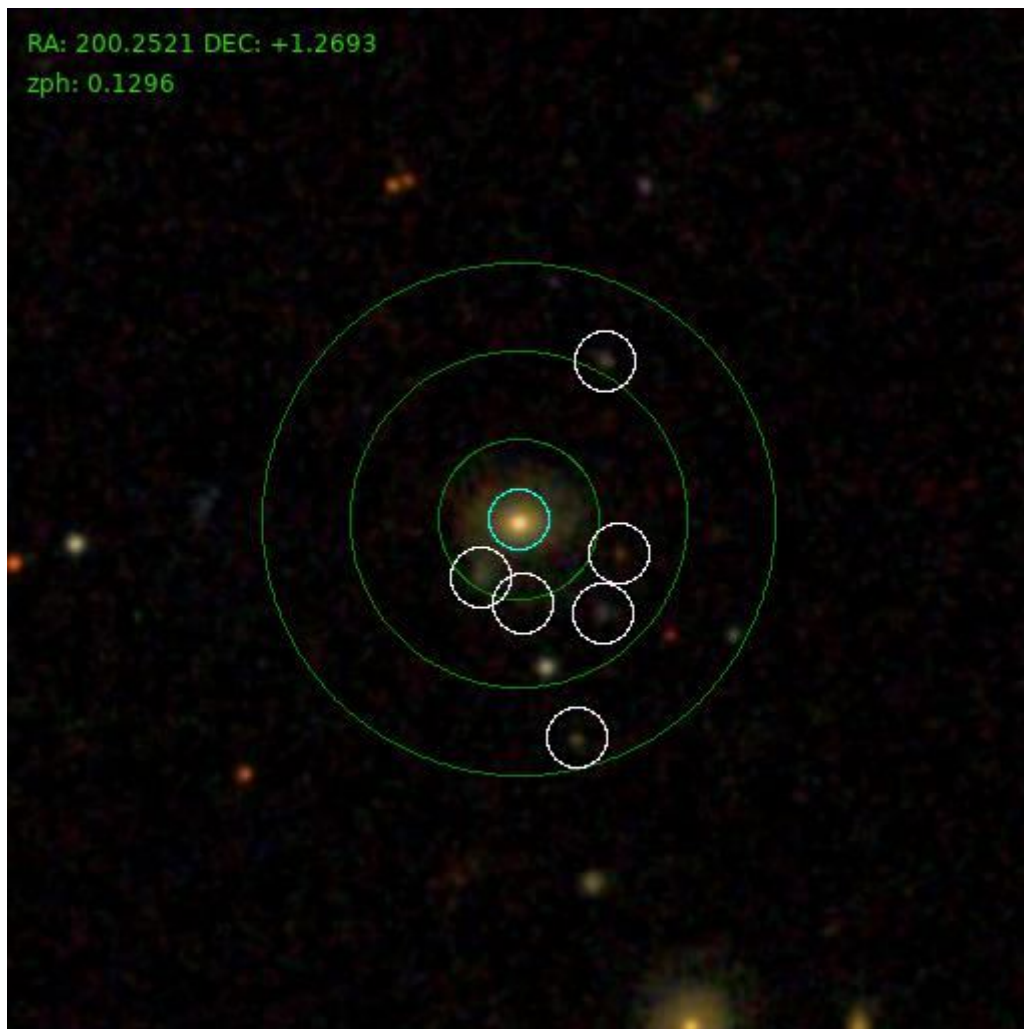
**Figure SA1.** This figure displays astronomical sky maps with the J2000 epoch coordinate system of the observed positions of clusters in the MWAR (top row), WNMR (middle row) and RNMW (bottom row) datasets.



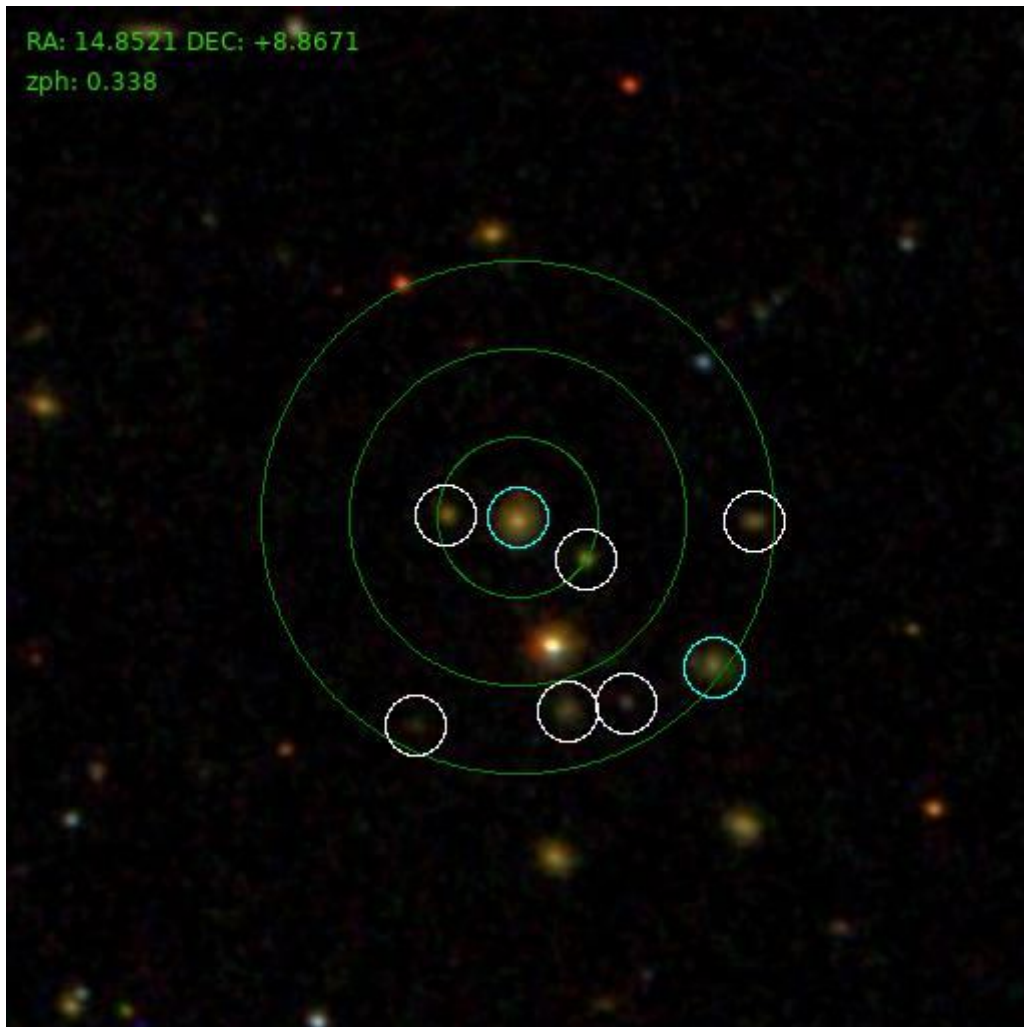
**Figure SA2.** This figure displays the ‘actual’ redshift distributions, where photometric redshifts of clusters in the MWAR dataset (blue dashed line), MWAR training set (cyan dashed line), MWAR validation set (orange dashed line) and WNMR test set (green dotted line) are originally estimated by WHL12. Whilst photometric redshifts of clusters in the RNMW test set (red dotted line) are originally estimated by redMaPPer. The top row contains clusters within a 10 arcseconds search radius, the middle row contains clusters within a 21 arcseconds search radius and the bottom row contains clusters within a 32 arcseconds search radius.



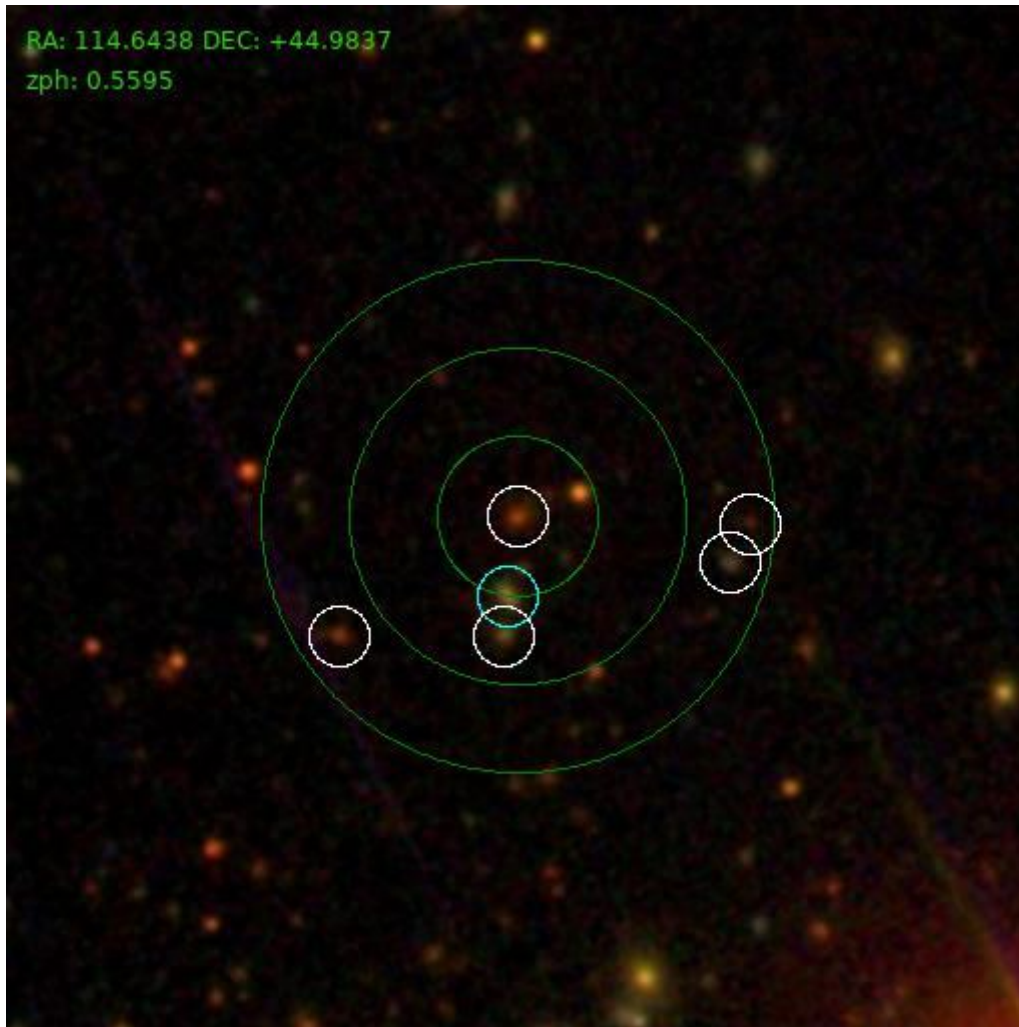
**Figure SA3.** This figure displays a direct comparison of photometric redshifts for clusters in the MWAR dataset that are originally estimated by the WHL12 and redMaPPer cluster catalogues.



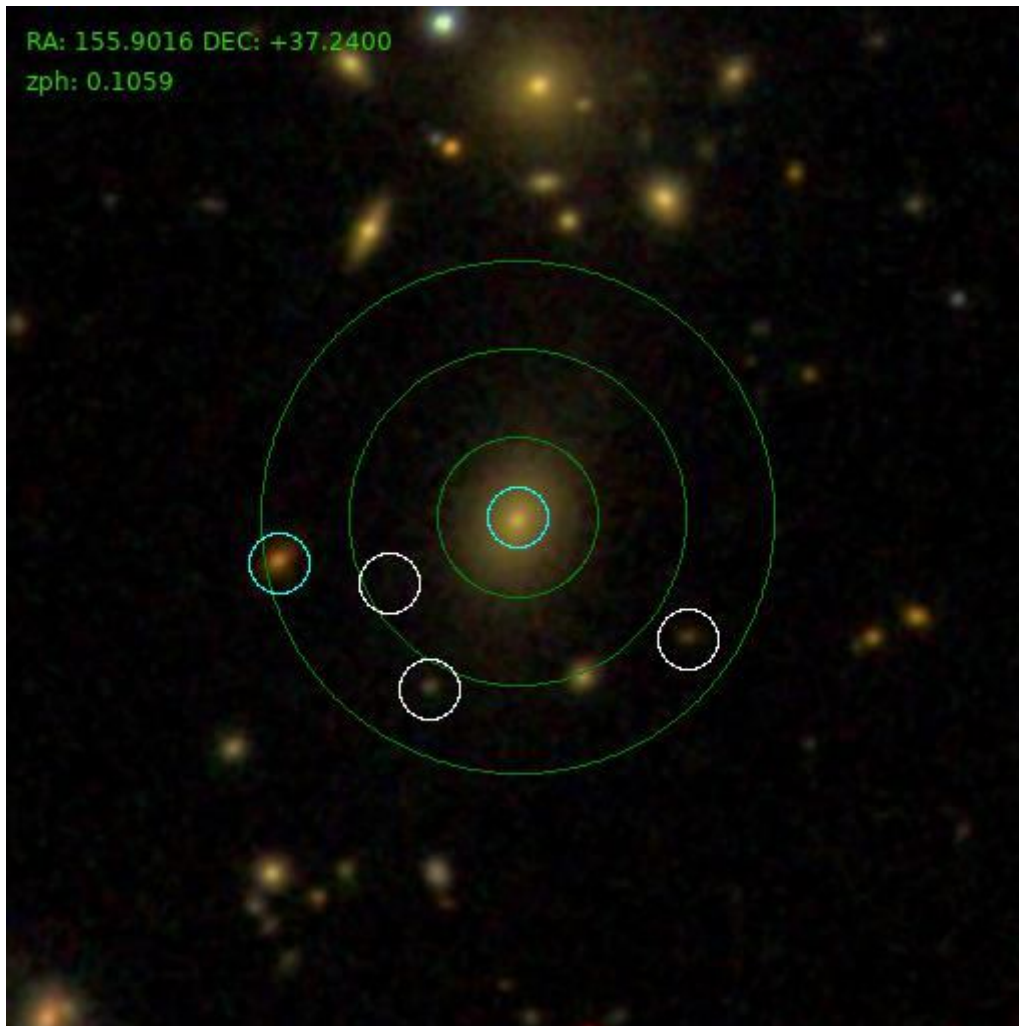
**Figure SA4.** This figure displays an SDSS image of a cluster from the WNMR test set with J2000 coordinates of RA: 200.2521 and Dec: +1.2693. The cluster has a photometric redshift of  $z_{ph}: 0.1296$  in the WHL12 cluster catalogue. The green circles represent the size of the 10, 21 and 32 arcseconds search radii respectively. Any objects with no circle surrounding it within the 32 arcseconds search radius is not considered to be a galaxy or is a galaxy with poor photometry. The white circles represent galaxies with 'clean' photometry, as determined by SDSS, found within the 32 arcseconds search radius that are removed if all LM-0.5 filter magnitude-cuts (excluding the u filter) for the 32 arcseconds search radius are applied at the same time. The cyan circles represent galaxies with also 'clean' photometry, as determined by SDSS, found within the 32 arcseconds search radius that remain if all LM-0.5 filter magnitude-cuts (excluding the u filter) for the 32 arcseconds search radius are applied at the same time. From which, we find that only the central galaxy remains within the 32 arcseconds search radius, such that the tuned model returns photometric redshift estimates of  $z_{ph}: 0.1269$  with  $CI_{95\%}=[0.0961, 0.3093]$  for the 10 arcseconds search radius,  $z_{ph}: 0.1092$  with  $CI_{95\%}=[0.0893, 0.4661]$  for the 21 arcseconds search radius and  $z_{ph}: 0.3976$  with  $CI_{95\%}=[0.1526, 0.4918]$  for the 32 arcseconds search radius. This example shows that the training set itself can contaminate model predictions when a larger search radius is applied, as we observe that no interloping galaxies are included when the 32 arcseconds search radius is used.



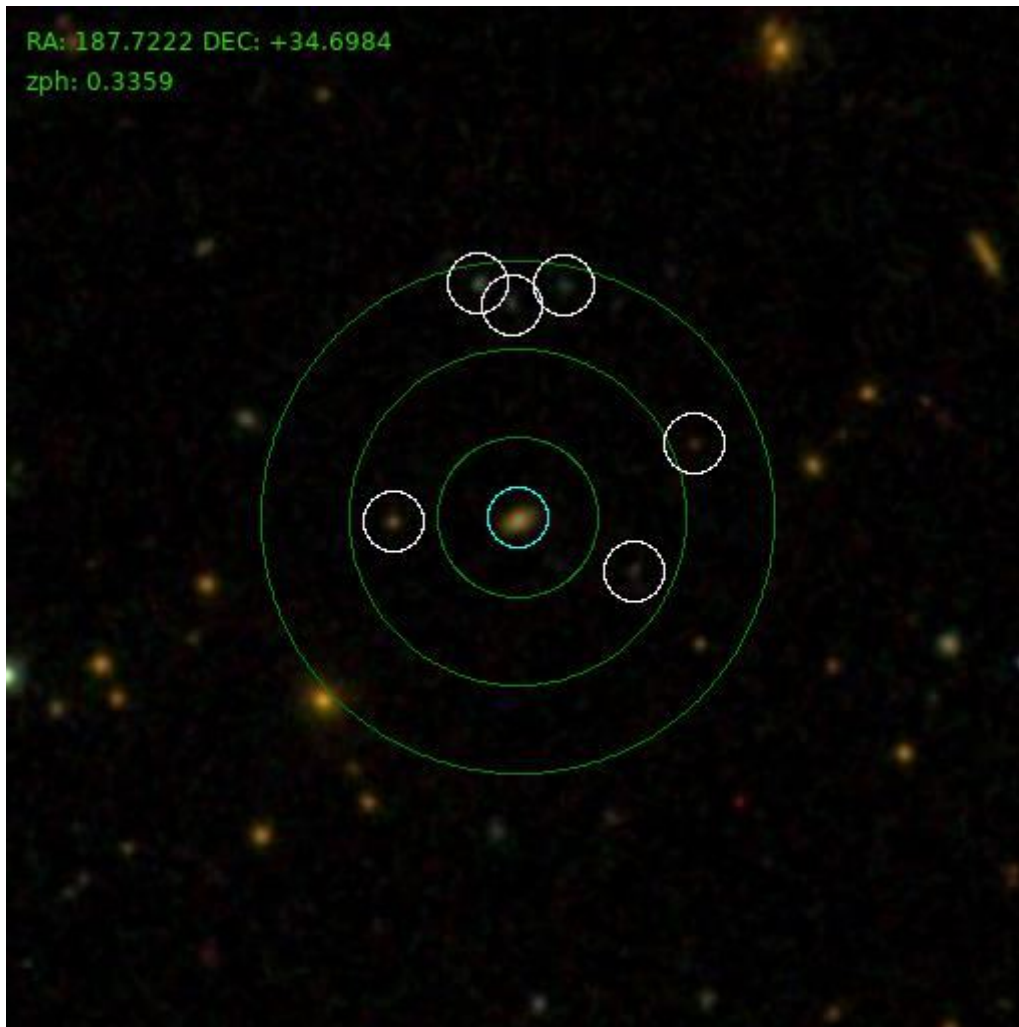
**Figure SA5.** This figure displays an SDSS image of a cluster from the WNMR test set with J2000 coordinates of RA: 14.8521 and Dec: +8.8671. The cluster has a photometric redshift of zph: 0.338 in the WHL12 cluster catalogue. The green circles represent the size of the 10, 21 and 32 arcseconds search radii respectively. Any objects with no circle surrounding it within the 32 arcseconds search radius is not considered to be a galaxy or is a galaxy with poor photometry. The white circles represent galaxies with 'clean' photometry, as determined by SDSS, found within the 32 arcseconds search radius that are removed if all LM-0.5 filter magnitude-cuts (excluding the u filter) for the 32 arcseconds search radius are applied at the same time. The cyan circles represent galaxies with also 'clean' photometry, as determined by SDSS, found within the 32 arcseconds search radius that remain if all LM-0.5 filter magnitude-cuts (excluding the u filter) for the 32 arcseconds search radius are applied at the same time. From which, we find that the central galaxy and another galaxy remains within the 32 arcseconds search radius, such that the tuned model returns photometric redshift estimates of zph: 0.1859 with  $CI_{95\%}=[0.1664, 0.2261]$  for the 10 arcseconds search radius, zph: 0.1877 with  $CI_{95\%}=[0.1653, 0.2519]$  for the 21 arcseconds search radius and zph: 0.1651 with  $CI_{95\%}=[0.1431, 0.2001]$  for the 32 arcseconds search radius. This example shows that the training set itself can contaminate model predictions at all search radii, as we observe that no obvious interloping galaxies are included for any search radii.



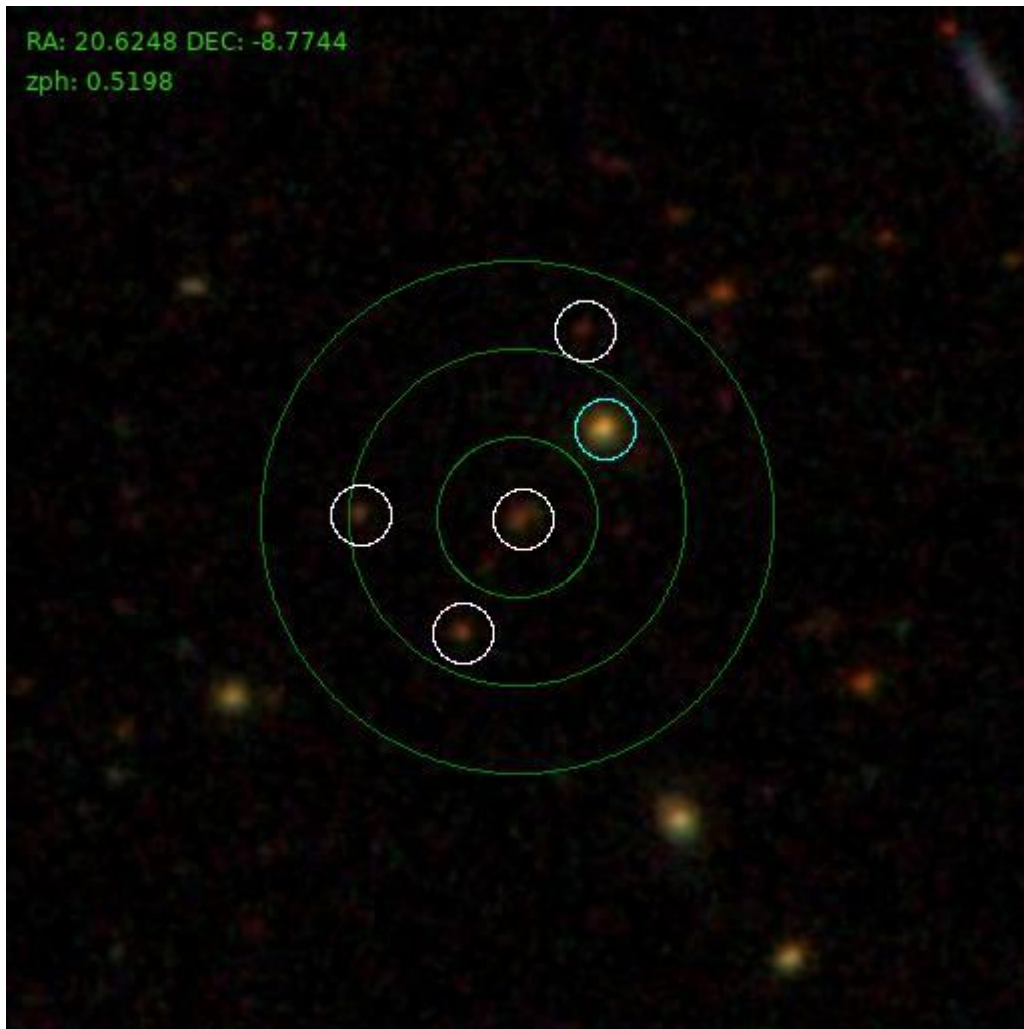
**Figure SA6.** This figure displays an SDSS image of a cluster from the WNMR test set with J2000 coordinates of RA: 114.6438 and Dec: +44.9837. The cluster has a photometric redshift of  $z_{ph}: 0.5595$  in the WHL12 cluster catalogue. The green circles represent the size of the 10, 21 and 32 arcseconds search radii respectively. Any objects with no circle surrounding it within the 32 arcseconds search radius is not considered to be a galaxy or is a galaxy with poor photometry. The white circles represent galaxies with 'clean' photometry, as determined by SDSS, found within the 32 arcseconds search radius that are removed if all LM-0.5 filter magnitude-cuts (excluding the u filter) for the 32 arcseconds search radius are applied at the same time. The cyan circles represent galaxies with also 'clean' photometry, as determined by SDSS, found within the 32 arcseconds search radius that remain if all LM-0.5 filter magnitude-cuts (excluding the u filter) for the 32 arcseconds search radius are applied at the same time. From which, we find that an interloping galaxy remains within the 32 arcseconds search radius, such that the tuned model returns photometric redshift estimates of  $z_{ph}: 0.1730$  with  $CI_{95\%}=[0.1153, 0.2350]$  for the 10 arcseconds search radius,  $z_{ph}: 0.2399$  with  $CI_{95\%}=[0.1960, 0.2710]$  for the 21 arcseconds search radius and  $z_{ph}: 0.1637$  with  $CI_{95\%}=[0.1152, 0.3672]$  for the 32 arcseconds search radius. This example shows that an interloping galaxy within the 10 arcseconds search radius, presumably at lower redshift than the cluster itself, can contaminate model predictions for all search radii.



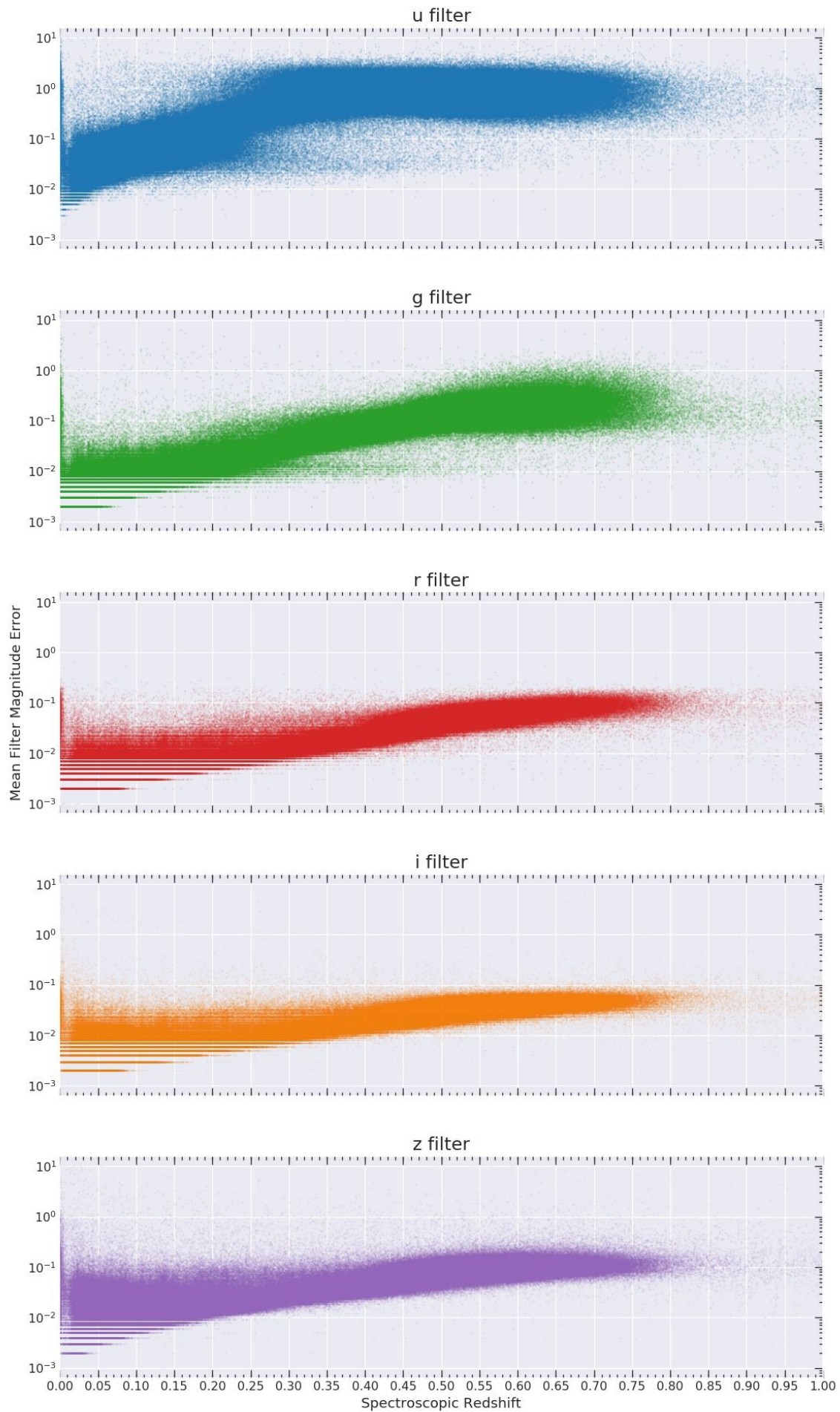
**Figure SA7.** This figure displays an SDSS image of a cluster from the RNMW test set with J2000 coordinates of RA: 155.9016 and Dec: +37.2400. The cluster has a photometric redshift of  $z_{ph}$ : 0.1059 in the redMaPPer cluster catalogue. The green circles represent the size of the 10, 21 and 32 arcseconds search radii respectively. Any objects with no circle surrounding it within the 32 arcseconds search radius is not considered to be a galaxy or is a galaxy with poor photometry. The white circles represent galaxies with 'clean' photometry, as determined by SDSS, found within the 32 arcseconds search radius that are removed if all LM-0.5 filter magnitude-cuts (excluding the u filter) for the 32 arcseconds search radius are applied at the same time. The cyan circles represent galaxies with also 'clean' photometry, as determined by SDSS, found within the 32 arcseconds search radius that remain if all LM-0.5 filter magnitude-cuts (excluding the u filter) for the 32 arcseconds search radius are applied at the same time. From which, we find that the central galaxy and an interloping galaxy remains within the 32 arcseconds search radius, such that the tuned model returns photometric redshift estimates of  $z_{ph}$ : 0.1115 with  $CI_{95\%}=[0.0914, 0.1239]$  for the 10 arcseconds search radius,  $z_{ph}$ : 0.1121 with  $CI_{95\%}=[0.1024, 0.1198]$  for the 21 arcseconds search radius and  $z_{ph}$ : 0.2709 with  $CI_{95\%}=[0.1972, 0.4003]$  for the 32 arcseconds search radius. This example shows that an interloping galaxy, presumably at higher redshift than the cluster itself, can contaminate model predictions when the search radius increases.



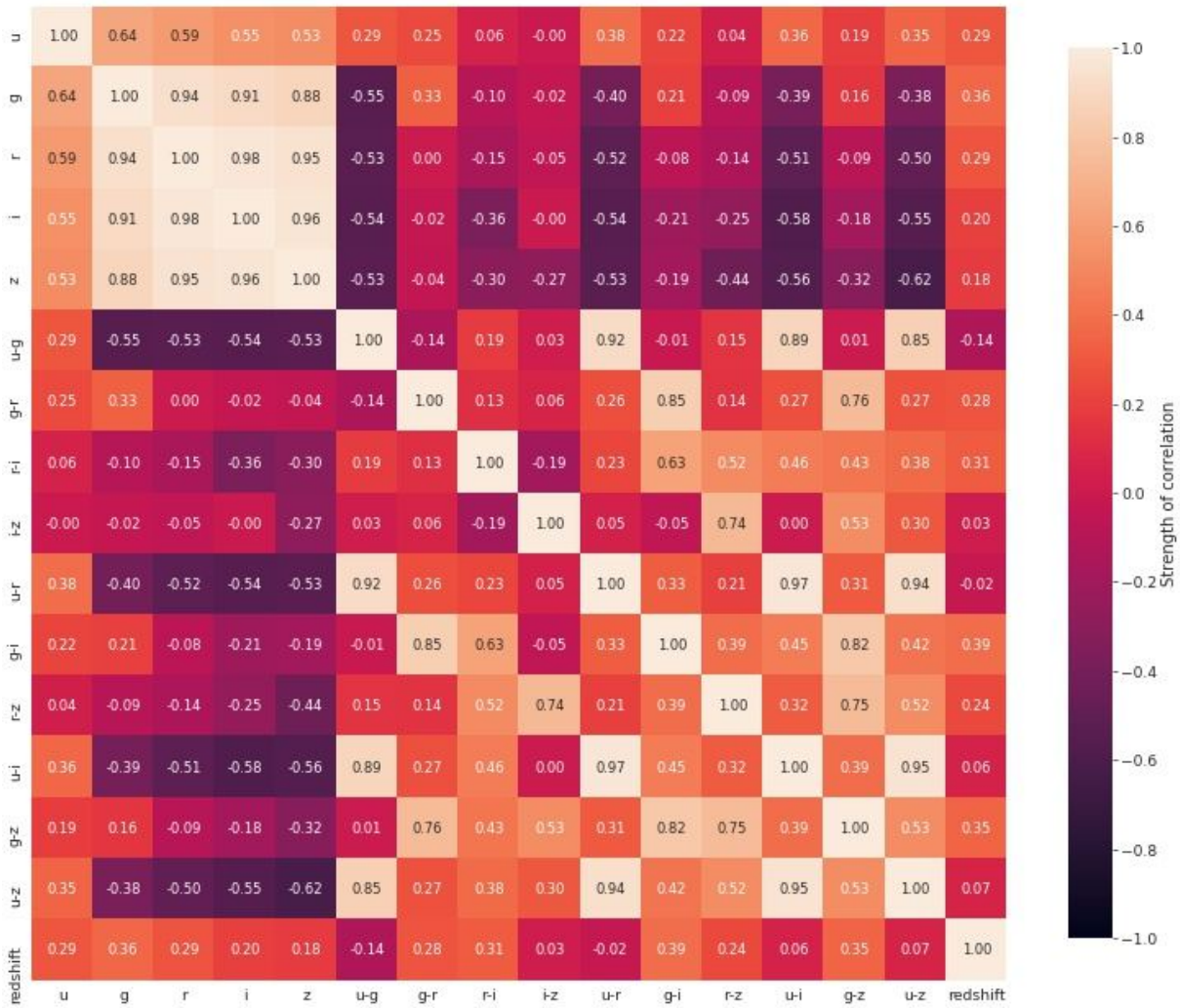
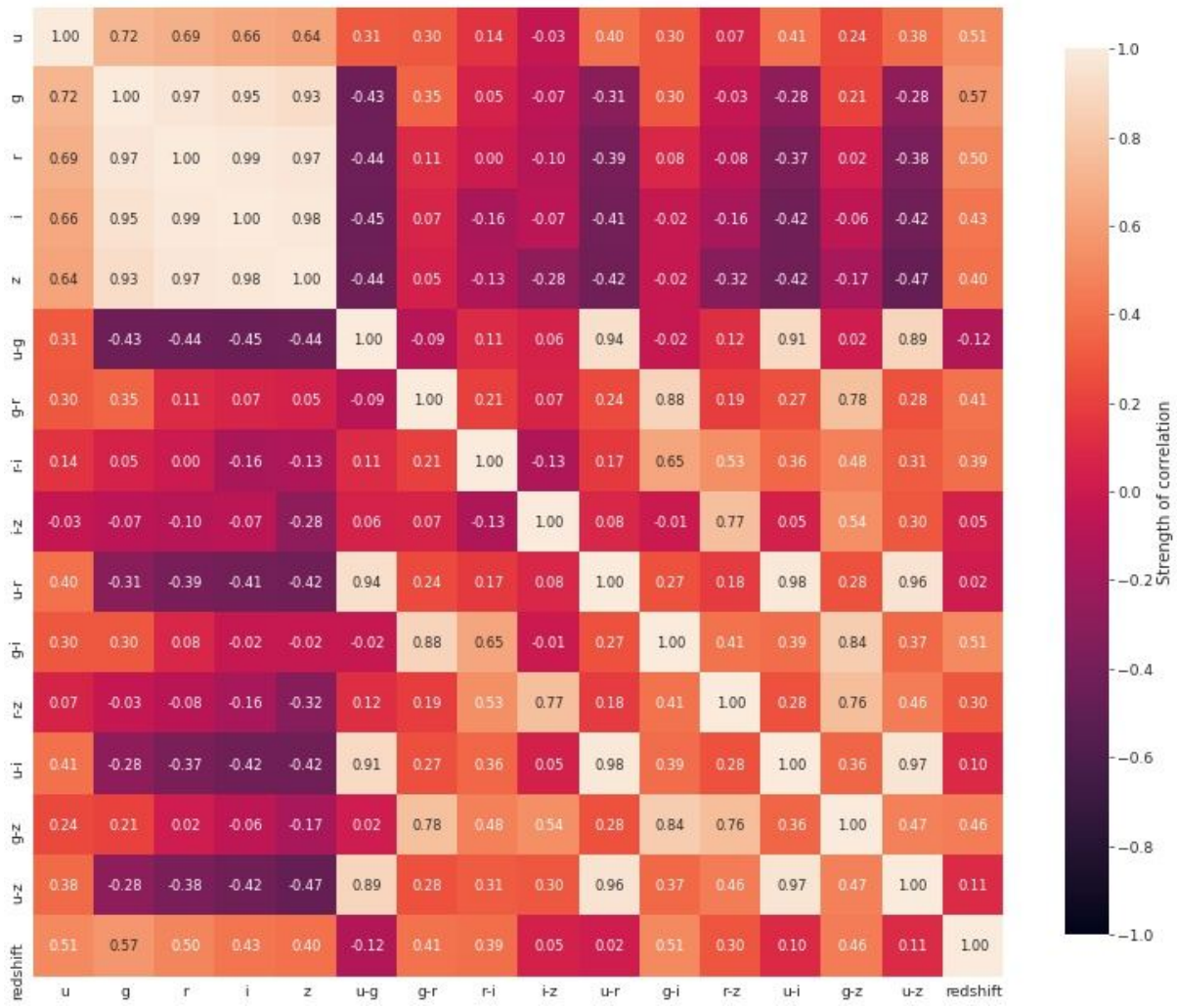
**Figure SA8.** This figure displays an SDSS image of a cluster from the RNMW test set with J2000 coordinates of RA: 187.7222 and Dec: +34.6984. The cluster has a photometric redshift of  $z_{ph}: 0.3359$  in the redMaPPer cluster catalogue. The green circles represent the size of the 10, 21 and 32 arcseconds search radii respectively. Any objects with no circle surrounding it within the 32 arcseconds search radius is not considered to be a galaxy or is a galaxy with poor photometry. The white circles represent galaxies with 'clean' photometry, as determined by SDSS, found within the 32 arcseconds search radius that are removed if all LM-0.5 filter magnitude-cuts (excluding the u filter) for the 32 arcseconds search radius are applied at the same time. The cyan circles represent galaxies with also 'clean' photometry, as determined by SDSS, found within the 32 arcseconds search radius that remain if all LM-0.5 filter magnitude-cuts (excluding the u filter) for the 32 arcseconds search radius are applied at the same time. From which, we find that only the central galaxy remains within the 32 arcseconds search radius, such that the tuned model returns photometric redshift estimates of  $z_{ph}: 0.1664$  with  $CI_{95\%}=[0.1189, 0.1820]$  for the 10 arcseconds search radius,  $z_{ph}: 0.1617$  with  $CI_{95\%}=[0.1264, 0.2041]$  for the 21 arcseconds search radius and  $z_{ph}: 0.1474$  with  $CI_{95\%}=[0.1191, 0.2131]$  for the 32 arcseconds search radius. This example also shows that the training set itself can contaminate model predictions at all search radii, as we observe that no interloping galaxies are included for any search radii.

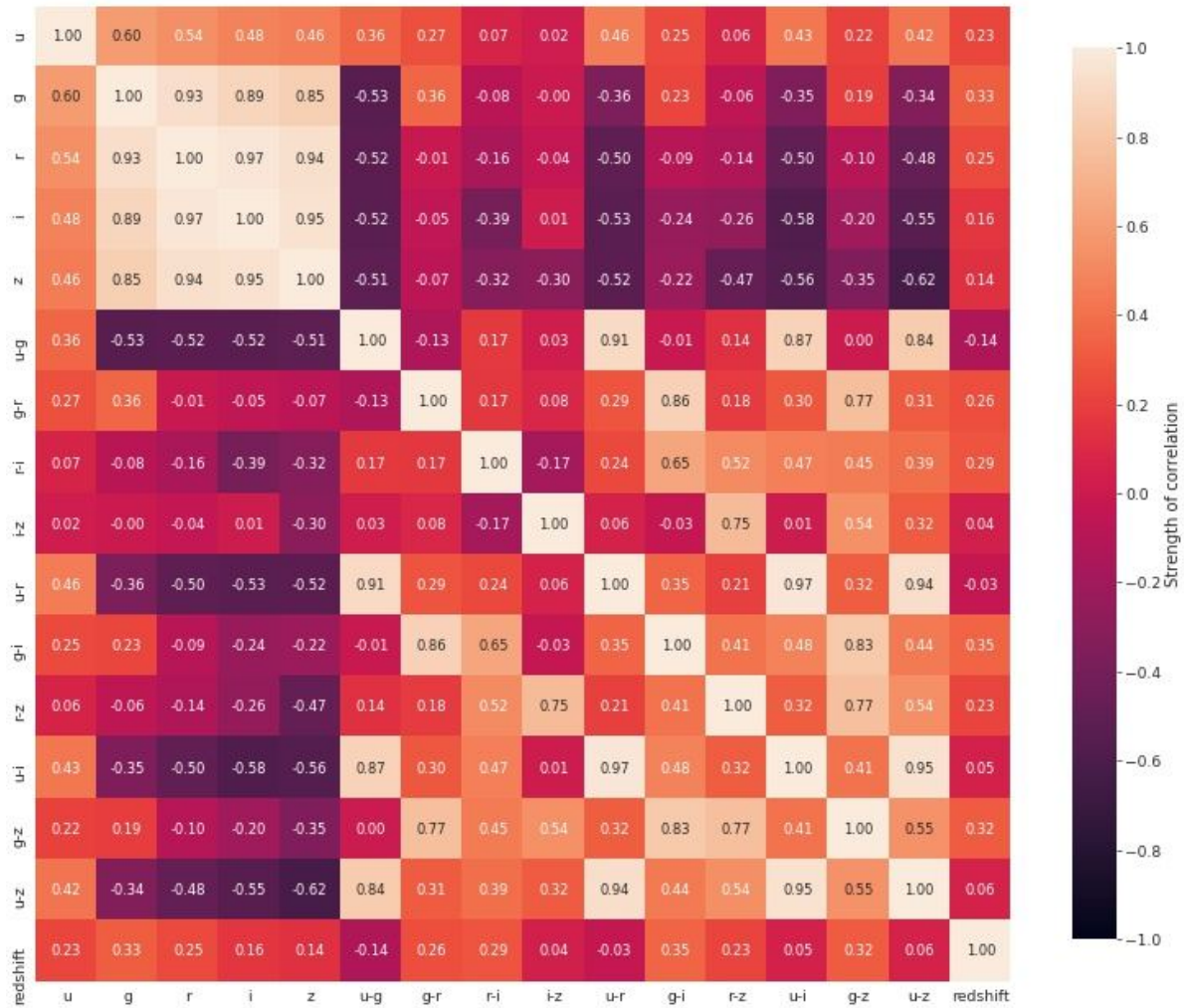


**Figure SA9.** This figure displays an SDSS image of a cluster from the RNMW test set with J2000 coordinates of RA: 20.6248 and Dec: -8.7744. The cluster has a photometric redshift of  $z_{ph}: 0.5198$  in the redMaPPer cluster catalogue. The green circles represent the size of the 10, 21 and 32 arcseconds search radii respectively. Any objects with no circle surrounding it within the 32 arcseconds search radius is not considered to be a galaxy or is a galaxy with poor photometry. The white circles represent galaxies with 'clean' photometry, as determined by SDSS, found within the 32 arcseconds search radius that are removed if all LM-0.5 filter magnitude-cuts (excluding the u filter) for the 32 arcseconds search radius were applied at the same time. The cyan circles represent galaxies with also 'clean' photometry, as determined by SDSS, found within the 32 arcseconds search radius that remain if all LM-0.5 filter magnitude-cuts (excluding the u filter) for the 32 arcseconds search radius were applied at the same time. From which, we find that an interloping galaxy remains within the 32 arcseconds search radius, such that the tuned model returns photometric redshift estimates of  $z_{ph}: 0.5121$  with  $CI_{95\%}=[0.4954, 0.5281]$  for the 10 arcseconds search radius,  $z_{ph}: 0.4191$  with  $CI_{95\%}=[0.2343, 0.4699]$  for the 21 arcseconds search radius and  $z_{ph}: 0.1415$  with  $CI_{95\%}=[0.1259, 0.2168]$  for the 32 arcseconds search radius. This example shows that an interloping galaxy, presumably at lower redshift than the cluster itself, can contaminate model predictions when the search radius increases.

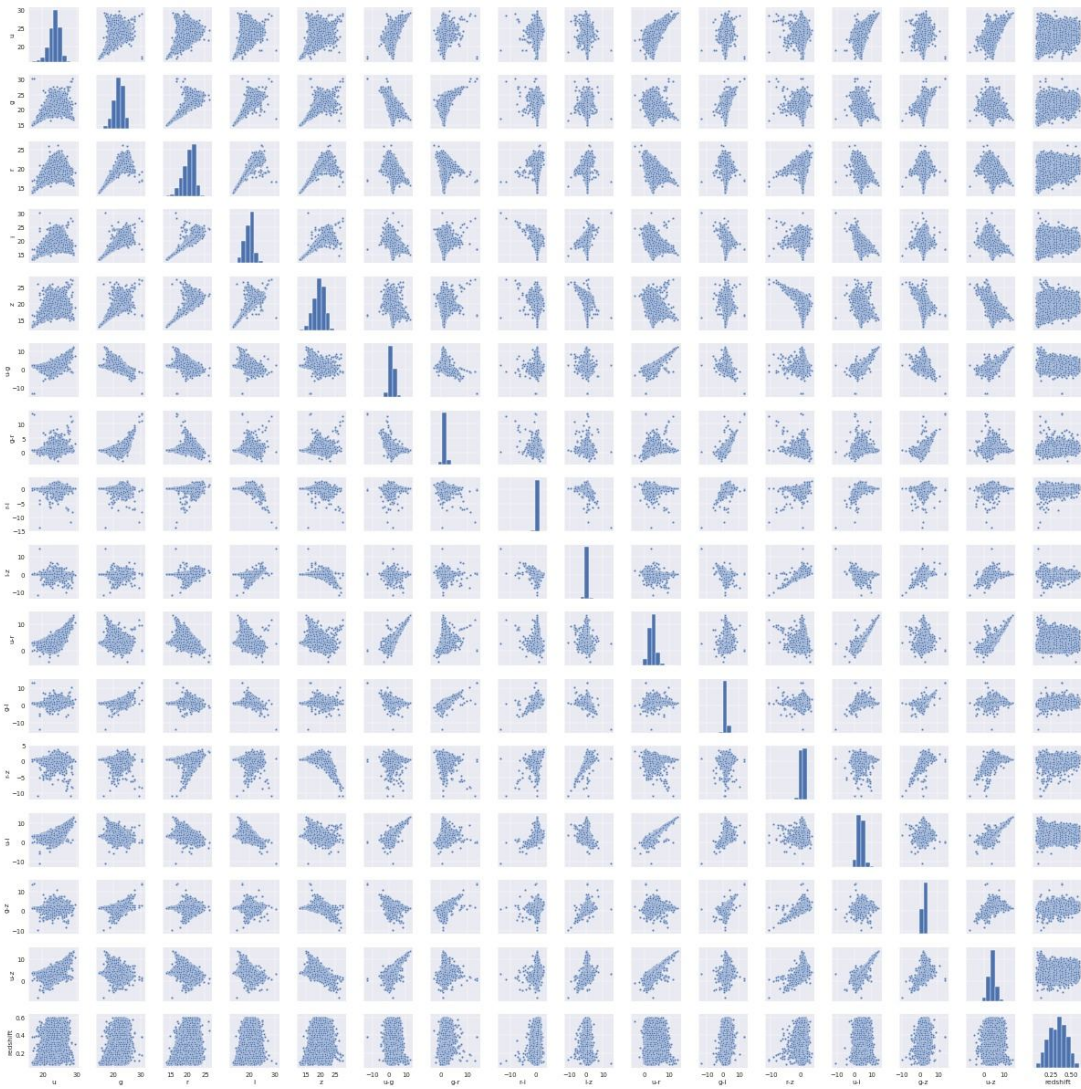
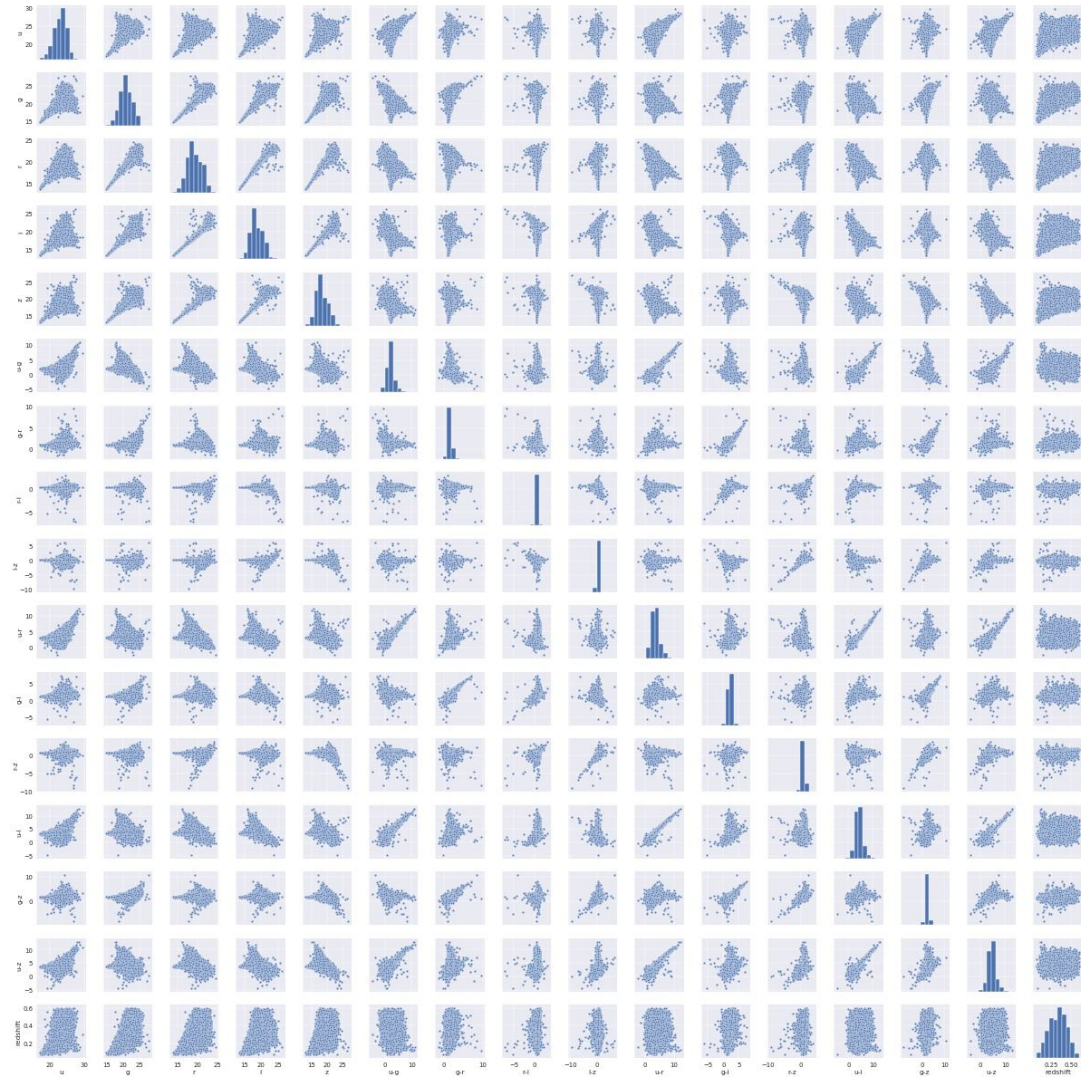


**Figure SA10.** This figure displays the mean filter magnitude errors versus spectroscopic redshift of observed galaxies in SDSS for the *u* (top row), *g* (second from top row), *r* (middle row), *i* (second from bottom row) and *z* (bottom row) filters.





**Figure SA11.** This figure displays correlation matrix heatmaps of all features with raw photometry data from the MWAR training set for the 10 (top row), 21 (middle row) and 32 (bottom row) arcseconds search radius. The colourbar represents the strength of correlation between the features.



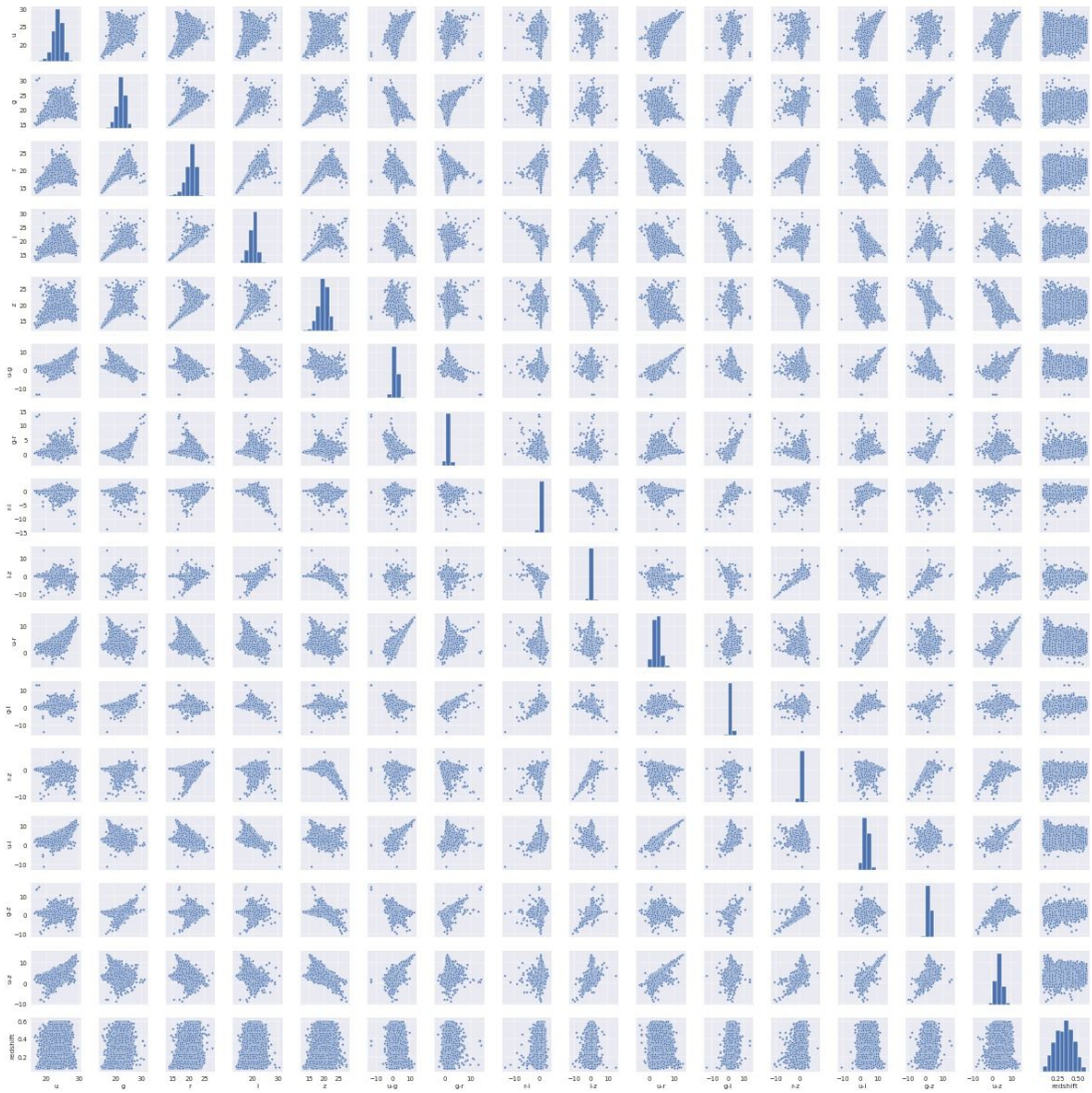


**Figure SA12.** This figure displays correlation matrix scatterplots of all features with raw photometry data from the MWAR training set for the 10 (top row), 21 (middle row) and 32 (bottom row) arcseconds search radius.

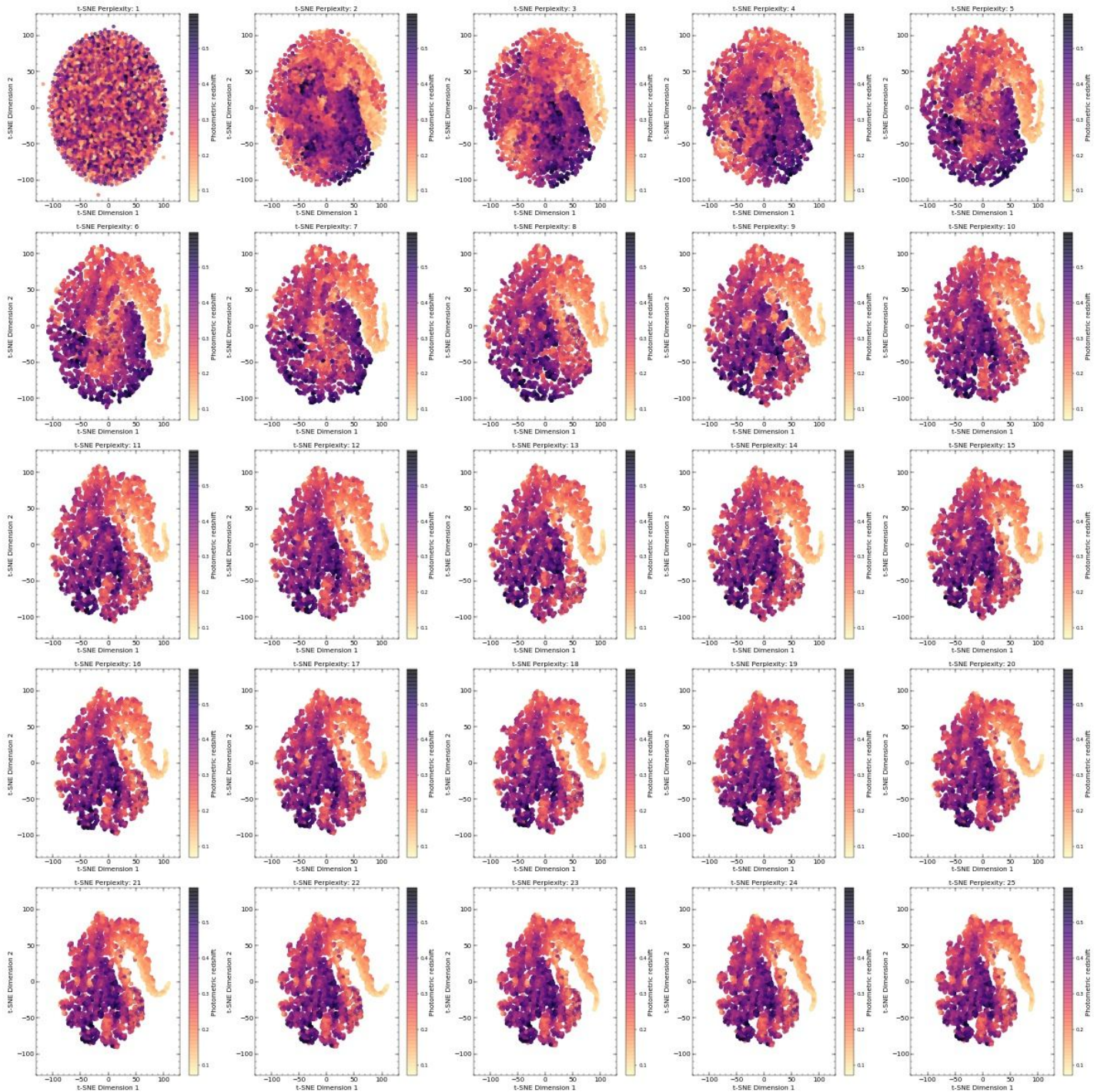


**Figure SA13.** This figure displays a two dimensional representation of the feature space in the MVAR training set with no feature scaling applied for a 10 arcseconds search radius with LM filter magnitude-cuts applied using the t-SNE algorithm. The colourbar represents the photometric redshift of galaxies found within the search radius of clusters originally estimated by WHL12. The t-SNE perplexity value relates to the number of nearest neighbours used to compress the dimensionality of the dataset.

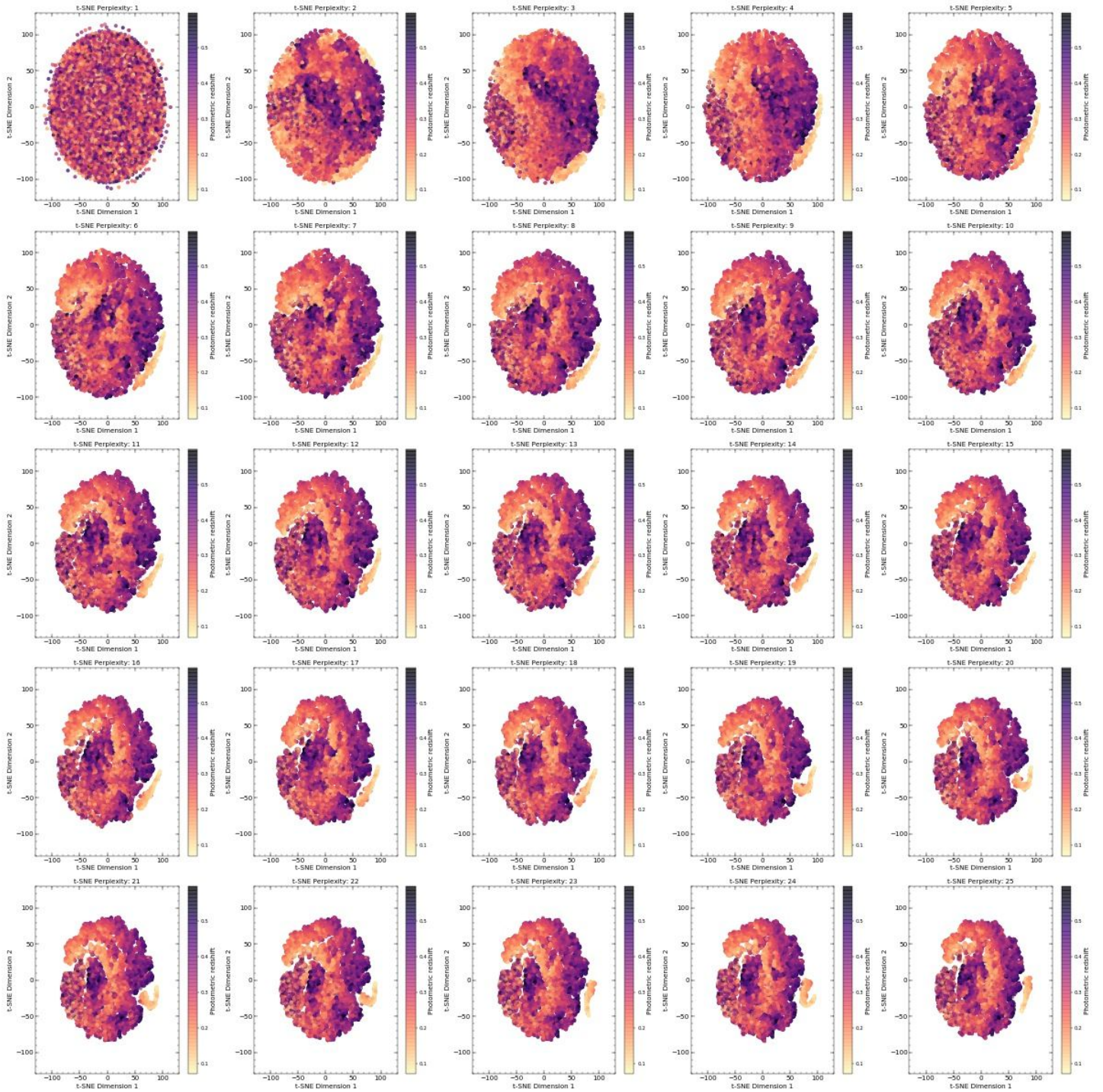


**Figure SA14.** This figure displays a two dimensional representation of the feature space in the MWAR training set with no feature scaling applied for a 21 arcseconds search radius with LM filter magnitude-cuts applied using the t-SNE algorithm. The colourbar represents the photometric redshift of galaxies found within the search radius of clusters originally estimated by WHL12. The t-SNE perplexity value relates to the number of nearest neighbours used to compress the dimensionality of the dataset.

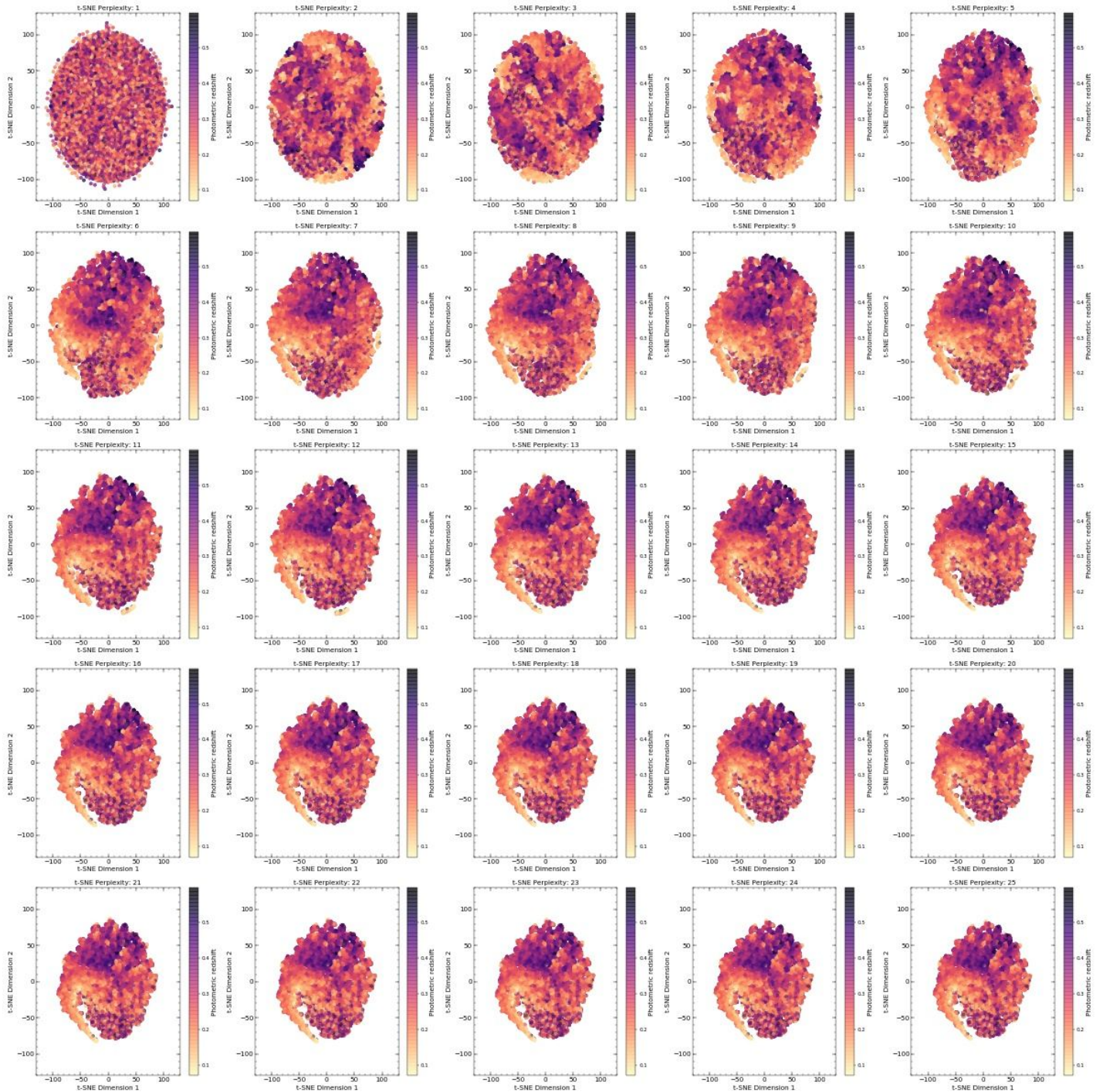


**Figure SA15.** This figure displays a two dimensional representation of the feature space in the MWAR training set with no feature scaling applied for a 32 arcseconds search radius with LM-0.5 filter magnitude-cuts applied using the t-SNE algorithm. The colourbar represents the photometric redshift of galaxies found within the search radius of clusters originally estimated by WHL12. The t-SNE perplexity value relates to the number of nearest neighbours used to compress the dimensionality of the dataset.

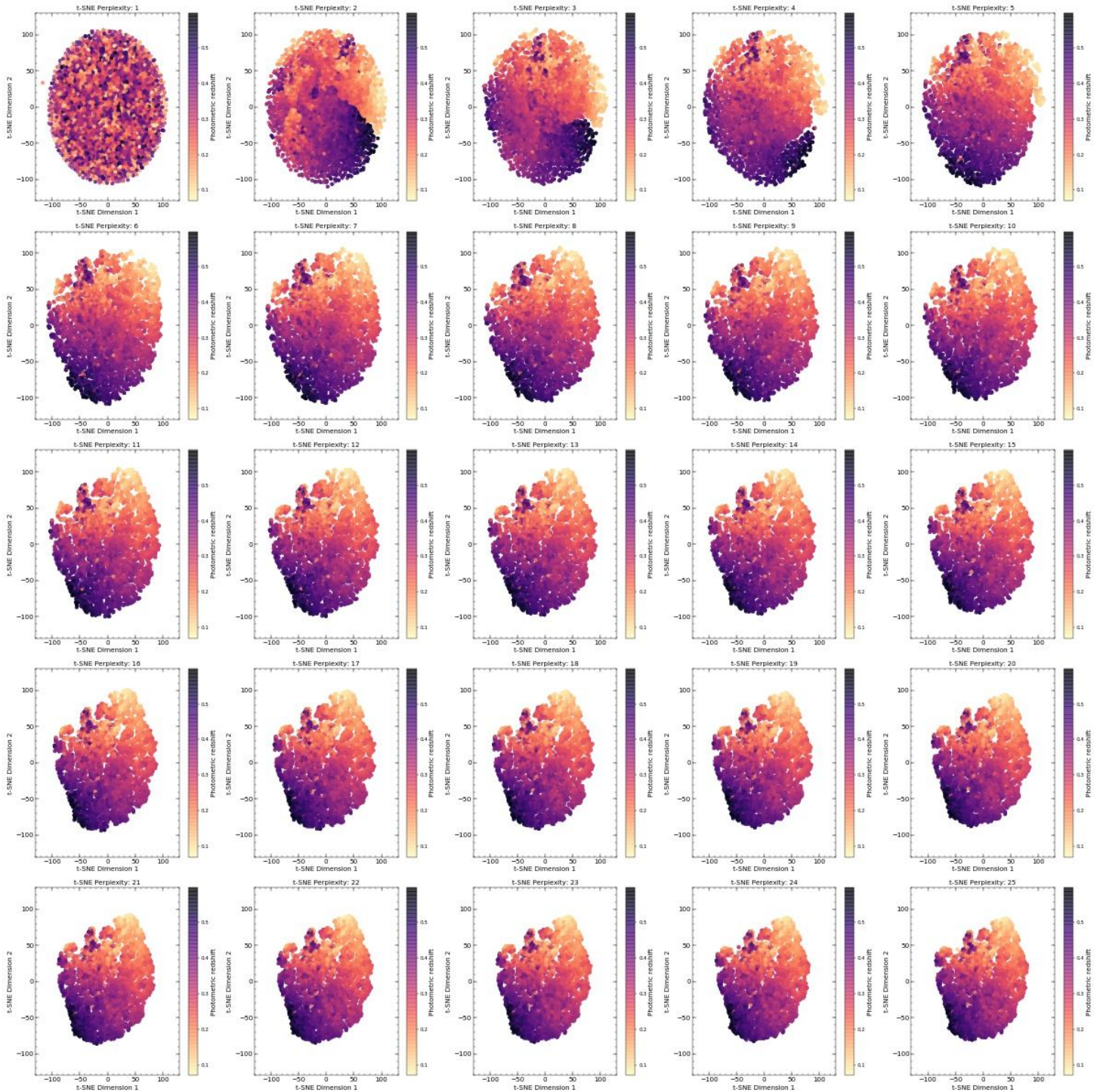


**Figure SA16.** This figure displays a two dimensional representation of the feature space in the MWAR training set with feature scaling applied for a 10 arcseconds search radius with LM filter magnitude-cuts applied using the t-SNE algorithm. The colourbar represents the photometric redshift of galaxies found within the search radius of clusters originally estimated by WHL12. The t-SNE perplexity value relates to the number of nearest neighbours used to compress the dimensionality of the dataset.

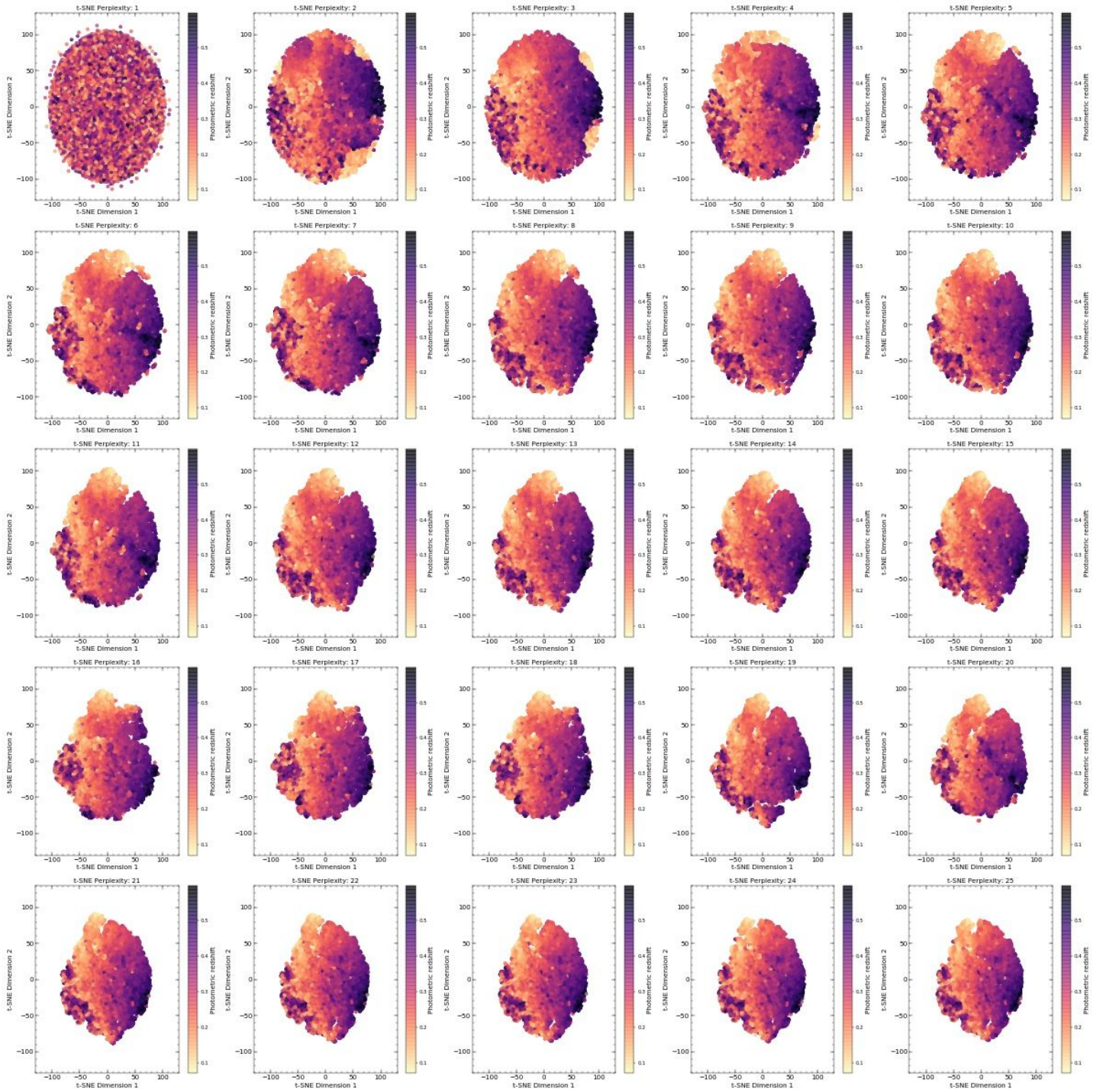


**Figure SA17.** This figure displays a two dimensional representation of the feature space in the MWAR training set with feature scaling applied for a 21 arcseconds search radius with LM filter magnitude-cuts applied using the t-SNE algorithm. The colourbar represents the photometric redshift of galaxies found within the search radius of clusters originally estimated by WHL12. The t-SNE perplexity value relates to the number of nearest neighbours used to compress the dimensionality of the dataset.

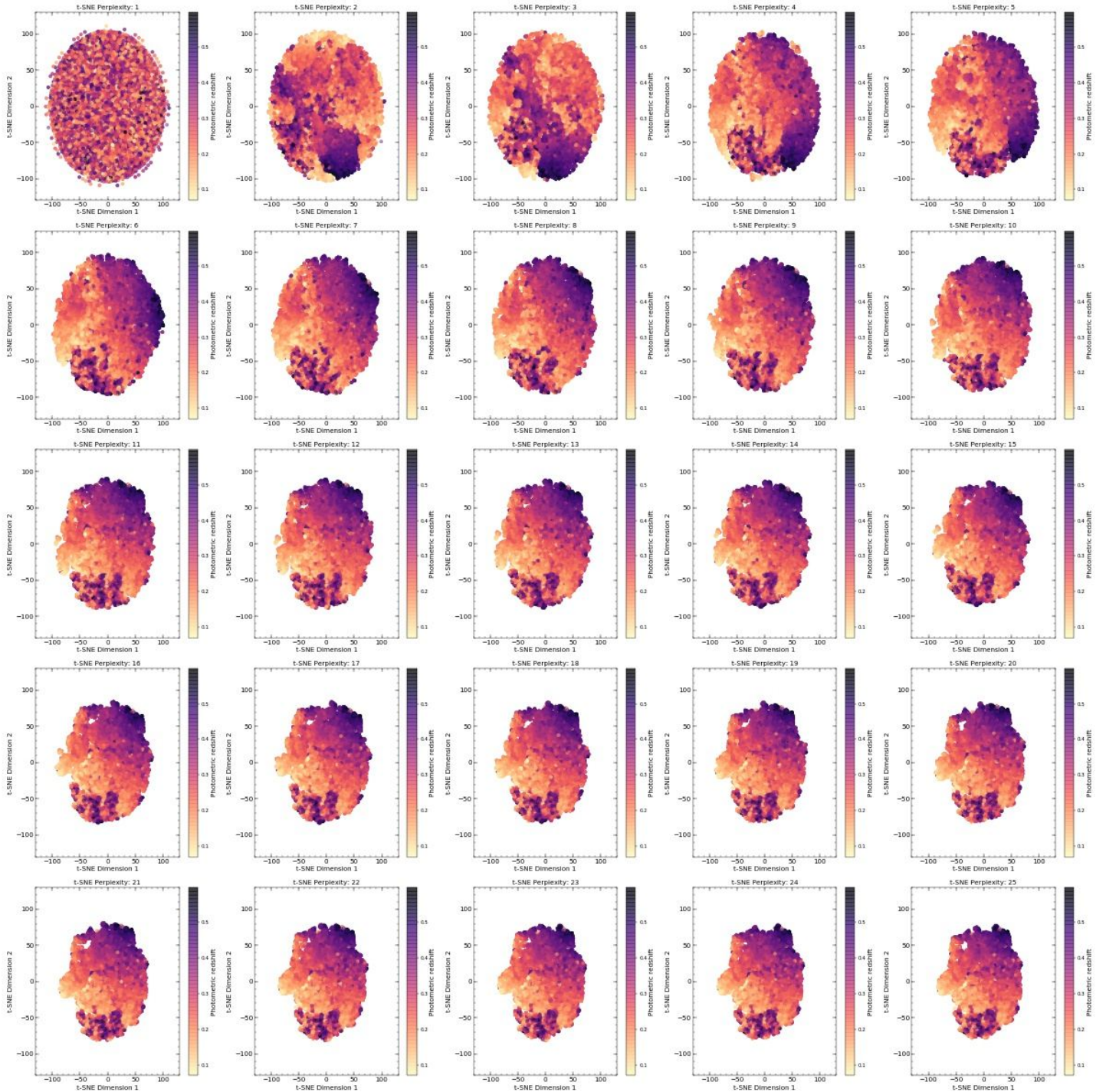


**Figure SA18.** This figure displays a two dimensional representation of the feature space in the MWAR training set with feature scaling applied for a 32 arcseconds search radius with LM-0.5 filter magnitude-cuts applied using the t-SNE algorithm. The colourbar represents the photometric redshift of galaxies found within the search radius of clusters originally estimated by WHL12. The t-SNE perplexity value relates to the number of nearest neighbours used to compress the dimensionality of the dataset.